Technical Physics Letters, Vol. 28, No. 9, 2002, pp. 707–710. Translated from Pis'ma v Zhurnal Tekhnicheskoĭ Fiziki, Vol. 28, No. 17, 2002, pp. 1–8.

On the Mechanisms of Current Transfer in *n*-In_2Se_3–*p*-GaSe Heterostructures

S. I. Drapak, Z. D. Kovalyuk, V. V. Netyaga, and V. B. Orletskiĭ

Frantsevich Institute of Material Sciences Problems (Chernivtsi Department), National Academy of Sciences of Ukraine, Chernivtsi, Ukraine

e-mail: chimsp@unicom.cv.ua

Received February 5, 2002

Abstract—The current–voltage and capacitance–voltage characteristics of originally fabricated photosensitive, radiation-stable anisotype *n*-In_2Se_3–*p*-GaSe heterostructures are presented. The electrical properties of these heterostructures depend on the method of fabrication, which is explained by variation of the band parameters of indium selenide. © *2002 MAIK "Nauka/Interperiodica".*

Gallium selenide (GaSe) and indium selenide (In_2Se_3) belong to a broad class of layered semiconductors. The former compound is a well-known semiconductor material employed in a number of photosensitive diode structures (see, e.g., [1, 2]), while the latter compound remains insufficiently studied. To our knowledge, there are only a few papers devoted to the optical and electrical properties of In_2Se_3 [3–5]. A special feature of In_2Se_3 crystals is a highly defective structure and, hence, increased radiation stability.

Below we present the results of investigation of the current transfer mechanisms in photosensitive, radiation-stable anisotype *n*-In_2Se_3–*p*-GaSe heterostructures fabricated by different methods. These data can be of interest for developing methods of optimization of the main photoelectrical characteristics of such structures.

The *n*-In_2Se_3–*p*-GaSe heterojunctions were obtained by two methods. First, by bringing the two materials (1- to 1.2-mm-thick GaSe plates and 0.1- to 0.12-mm-thick In_2Se_3 plates) into tight optical contact. Second, by vacuum deposition of In_2Se_3 layers onto freshly cleaved GaSe substrates heated to ≈150°C at a residual pressure of not worse than 2×10^{-5} Torr. The samples were prepared using *p*-GaSe with a hole concentration of $p \approx 10^{14}$ cm^{-3} and *n*-In_2Se_3 possessing a hexagonal α phase structure (bandgap width E_g = 1.42 eV [3]) with an electron concentration of $n \approx 10^{16}$ cm^{-3}, grown by the Bridgman method. The charge carrier concentrations in both semiconductors were determined from room-temperature Hall effect measurements. The ohmic contacts were prepared by applying In–Ga eutectics, followed by fusing In on the side of In_2Se_3 and a silver paste composition (contactol) on the GaSe side.

The originally fabricated heterostructures are promising materials for use in photosensitive devices. For example, the open-circuit voltage measured on the structures illuminated at a power density of 100 mW/cm^2 was ~0.35 and 0.72 V for the samples prepared by the methods of optical contact and vacuum deposition, respectively. Measurements of the current–voltage (*J–V*) characteristics showed that the *n*-In_2Se_3–*p*-GaSe heterostructures possess pronounced diode properties in the entire temperature range studied (233–333 K): at a voltage of 1.5–2 V, the direct to reverse current ratio was greater than 10^3.

Figure 1 shows the band energy diagrams of the *n*-In_2Se_3–*p*-GaSe heterostructures prepared by the two different methods described above. The diagrams were constructed using published data on the physical properties of GaSe [6] and In_2Se_3 [3–5], the concentrations of majority carriers determined in both semiconductors, and the values of diffusion potential φ_0 determined

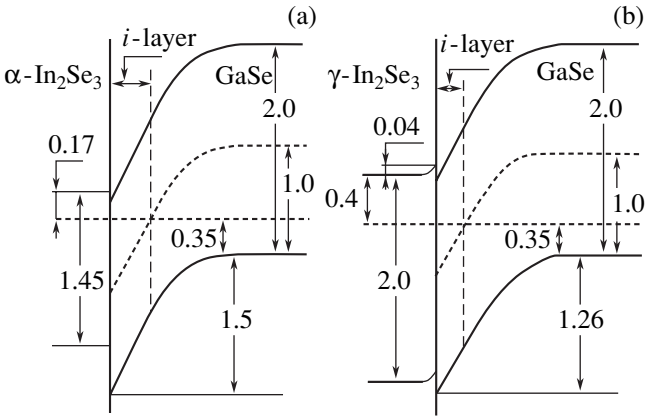

Fig. 1. Equilibrium energy band diagrams of the *n*-In_2Se_3–*p*-GaSe heterostructures obtained by (a) bringing the two materials into tight optical contact and (b) by vacuum deposition of In_2Se_3 layers onto freshly cleaved GaSe substrates. The values of energy parameters are indicated in electronvolts.

1063-7850/02/2809-0707$22.00 © 2002 MAIK "Nauka/Interperiodica"

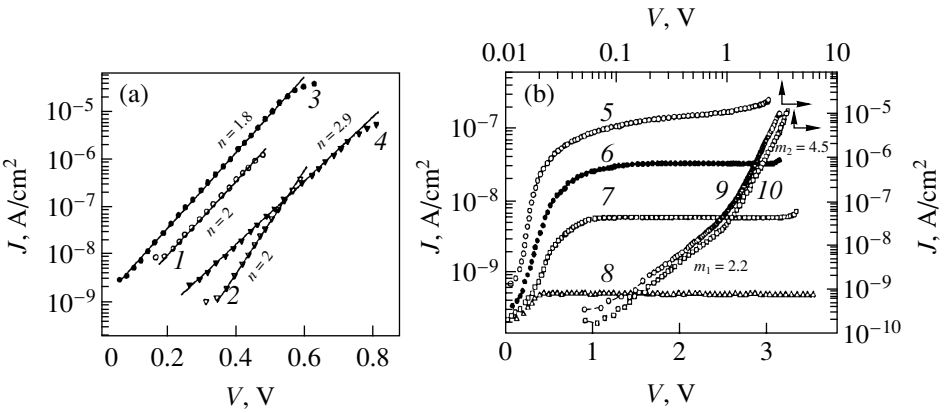

Fig. 2. Direct (a) and reverse (b) current–voltage characteristics of *n*-In_2Se_3–*p*-GaSe heterostructures obtained by (*1*, *2*, *5*–*8*) bringing the two materials into tight optical contact and (*3*, *4*, *9*, *10*) by vacuum deposition of In_2Se_3 layers onto GaSe substrates. The measurements were performed at T = 333 (*1*, *3*, *5*, *9*), 296 (*6*), 274 (*7*), and 240 K (*2*, *4*, *8*, *10*).

from the measured capacitance–voltage (*C*–*V*) characteristics. We also took into account the difference between the phase composition of In_2Se_2 films deposited in vacuum and that of the material used in the optical contacts. An analysis of the X-ray diffraction patterns showed that the films are composed predominantly of In_2Se_3 in the γ modification with E_g = 2.0 eV [3]. In addition, the films contain a hexagonal α-In_2Se_3 phase and a free indium phase. The room-temperature equilibrium charge carrier concentration in the films amounted to $n \approx 10^{15}$ cm^{-3}. The space-charge region thickness was determined by the formula [7]

$$W = [(2\varepsilon_0\varepsilon_n\varepsilon_p(\varphi_0 - eV)(p-n)^2)/(e(\varepsilon_n n + \varepsilon_p p)np)]^{1/2}, \quad (1)$$

where ε_0, ε_n, ε_p are the permittivities of vacuum, In_2Se_3, and GaSe, respectively. For ε_n = 9.53 [3] and ε_p = 8.86 [6], $W = 5 \times 10^{-4}$ cm for the optical contact and $W = 3 \times 10^{-4}$ cm for the structures with vacuum-deposited layers.

We compared the contact potential differences (Fig. 1) determined from the *C*–*V* curves to those calculated by the formula [7]

$$e\varphi_0 = (\chi_p + E_{gp} - E_{Fp}) - (\chi_n + E_{F_n}), \quad (2)$$

assuming (by analogy with [8]) that the electron affinity of In_2Se_3 in both structures is approximately the same and amounts to χ_n = 3.6 eV [9]. In expression (2), $\chi_{p,n}$ are the electron affinities and $E_{Fp,Fn}$ are the Fermi levels of semiconductors of the *p* and *n* types, respectively, and E_{gp} is the bandgap of the *p*-type semiconductor. For the calculation, we used χ_p = 3.6 eV for GaSe [10]. The experimental and calculated values of the contact potential difference are in good agreement. This result, as well as the *C*–*V* curves typical of the sharp *p*–*n* junctions or Schottky barriers observed for the *n*-In_2Se_3–*p*-GaSe heterostructures prepared by both methods, is indicative of the negligibly small influence of the inversion layer in GaSe appearing as a result of the large band bending in this semiconductor (Fig. 1).

In order to determine the mechanisms of charge transfer in the *n*-In_2Se_3–*p*-GaSe heterostructures, we measured the *J*–*V* curves in the directly and reversely biased samples.

Heterostructures based on optical contact. In the region of direct bias V = 0.1–0.6 V, where the voltage drop on the base semiconductor can be ignored, the *J*–*V* curve is described by an exponential function $J \sim \exp(eV/nkT)$, where the diode coefficient n remains constant (n = 2) in the entire temperature range T = 239–332 K (Fig. 2a, curves *1* and *2*). According to the Saha–Noyes–Shockley theory [7], this slope of the *J*–*V* curves is characteristic of the recombination processes in a space-charge region at low levels of injection. However, the activation energy determined from the slope of the temperature dependence of the recombination saturation current (Fig. 3, curve *1*) is equal to 0.58 eV, which is much smaller that the expected half of the GaSe bandgap width ($E_{gp}/2$ = 1 eV). This difference can be explained by the fact that recombination proceeds via the donor–acceptor pairs, rather than via simple centers. The temperature dependences of J_{0s} in the former case can be expressed as

$$J_{0s} \sim \exp[-(E_{gp} - \Delta E_t)/2kT] = \exp(-E'_{gp}/2kT), \quad (3)$$

where ΔE_t is the energy position of the impurity level. Taking into account the experimental value E'_g = 1.16 eV, we determine the impurity level depth as $\Delta E_t = E_{gp} - E'_g$ = 0.84 eV.

The total reverse current of the heterojunction at $|eV| > 2kT$ is [7]

$$J_{rev} = en_i W/\tau_i + (eD_n n_{p0}/L_n + eD_p p_{n0}/L_p), \quad (4)$$

where n_i is the intrinsic carrier concentration; n_{p0}, p_{n0} and D_n, D_p are the equilibrium concentrations and dif-

fusion coefficients of minority carriers in semiconductors of the p and n types, respectively; τ_i is the lifetime of charge carriers in the space-charge region; and L_n, L_p are the diffusion lengths of minority carriers in semiconductors of the p and n types, respectively. In Eq. (4), the first term in the right-hand part describes the production of carriers in the space-charge region, while the sum in parentheses describes the diffusion of minority carriers in the neutral regions adjacent to the space-charge region.

Figure 2b shows reverse branches of the current–voltage characteristics of the n-In_2Se_3–p-GaSe heterostructures based on the optical contact measured at various temperatures (curves *5–8*). Since saturation is not typical of the generation currents, the dominating mechanism of room-temperature charge transfer at a reverse bias of $|V| > 1$ V is the diffusion of minority carriers: holes from In_2Se_3 and electrons from GaSe. The regions in which the reverse current exhibits saturation are characteristic of the diffusion currents in thick-base structures [7]. The contribution of diffusion currents to the total current is known to grow with the temperature. Therefore, as the temperature increases, we should observe more extended regions of saturated current [7]. However, experimental data reveal the opposite trend: the maximum saturation current is observed at T = 240 K, while the curves measured at room temperature virtually do not exhibit saturation. This behavior cannot be explained by the increasing role of the carrier production (described by the first term in expression (4)), since the injection currents increase with the temperature at a slower rate ($\sim n_i$) as compared to the diffusion currents ($\sim n_i^2$). Therefore, we have to suggest that the reverse current contains contributions due to the tunneling and leakage currents. The regions where tunneling becomes the dominating room-temperature current transfer mechanism are observed for various samples at a reverse bias increased to 3–3.5 V. Here, the J–V curve can be approximated by an expression of the type $J \sim V^{4.5}$ corresponding to a soft breakdown.

Heterostructures based on the vacuum-deposited layers. In this case, the diode coefficient is no longer constant in the entire temperature range studied (Fig. 2a, curves *3* and *4*). The room-temperature value n = 2.05 is (like n = 2 for the optical contact) characteristic of recombination in the space-charge region. As the temperature decreases to T = 240 K, the diode coefficient grows to $n \approx 3$, which is evidence that the tunneling mechanism begins to dominate. At temperatures above room temperature (where n = 1.8), the diffusion current component becomes significant. Thus, the total current can be presented as

$$J = J_d + J_{gr} + J_{tun}. \quad (5)$$

Since neither of the two semiconductors in contact is degenerate, direct interband tunneling is impossible. At the same time, an indirect process, whereby electrons from the bottom of the conduction band of In_2Se_3 tunnel first to a local level E_1 and then to the valence band of p-GaSe, can take place. In this case,

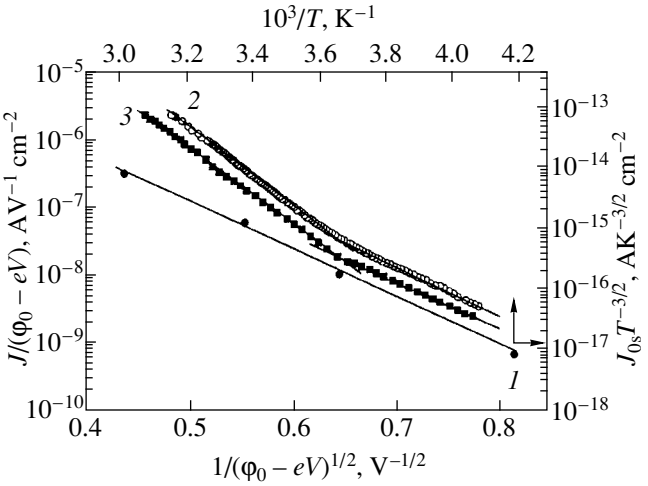

Fig. 3. (*1*) Temperature dependence of the saturation current density J_{0s} of a directly biased n-In_2Se_3–p-GaSe heterostructure based on the optical contact; (*2*, *3*) reverse current–voltage characteristics of a n-In_2Se_3–p-GaSe heterostructure based on vacuum-deposited films plotted in coordinates of Eq. (9) for T = 333 (*2*) and 240 K (*3*).

$$J_{tun} = \alpha N_1 T_t, \quad (6)$$

where α is a constant, N is the density of local centers at the E_1 level, and T_t is the tunneling probability. The latter quantity is given by the formula

$$T_t \approx \exp[(-4m^{*1/2}2^{1/2}E^{*3/2}\pi)/3e\hbar E], \quad (7)$$

where E^* is the tunneling energy and E is the electric field strength. Substituting relation (6) into formula (7), with a given value of the electric field in the sharp junction and E^* as a function of the barrier height, leads to an expression for the tunneling current [11]:

$$J_{tun} \cong \alpha N_1 \exp[-\alpha_1(E_g - eV)], \quad (8)$$

which determines behavior of the direct current at low temperatures. As the temperature increases, the charge transfer mechanism begins to change, whereby a dominating contribution is from the generation–recombination current component $J_{gr} = (en_iW/\tau_i)\exp(eV/2kT)$. At still higher temperatures, a significant contribution also comes from the diffusion current component $J_d = (eD_n n_{p0}/L_n + eD_p p_{n0}/L_p)\exp(eV/kT)$.

The reverse current of this heterostructure is virtually independent of temperature but exhibits a strong field dependence. This behavior is characteristic of the tunneling mechanism [12]. The reverse branches observed at $|V| > 0.3$ V cannot be approximated by single power functions $J \sim V^m$ and behave differently, depending on the bias voltage: for $|V| < 1$ V, m_1 = 2.2; for higher applied voltages, m_2 = 4.5 (Fig. 2b, curves *9* and *10*). In the region of smaller exponent $m = m_1$, the

dominating process is tunneling via local centers, while at $m = m_2$ and large biases, interband tunneling prevails. Indeed, for a barrier with a parabolic potential profile, the tunneling current is describe by the expression [7]

$$J = A\frac{e^3\sqrt{2m_n}V(\varphi_0 - eV)^{1/2}p}{2\pi^2\hbar^2\varphi_0^{1/2}(2\varepsilon\varepsilon_0\varphi_0)^{1/2}s} \times \exp\left(-\frac{4}{3}\frac{\sqrt{m_n\varepsilon\varepsilon_0}}{\hbar p^{1/2}}\frac{\varphi_0^{3/2}}{\sqrt{\varphi_0 - eV}}\right), \quad (9)$$

where s is the heterojunction area and ε, ε_0 are the permittivities of the semiconductor and vacuum, respectively.

According to formula (9), the J–V curve of a structure featuring tunneling through the barrier must represent a straight line in the coordinates of $\ln[J(\varphi_0 - eV)^{-1/2}]$ versus $(\varphi_0 - eV)^{-1/2}$. Presented in Fig. 3 (curves *2* and *3*), such plots appear as superpositions of two straight lines. This is evidence of the tunneling via local centers at a small bias, changed for interband tunneling with increasing applied voltages.

In concluding, it should be noted that the above data concerning the mechanisms of current transfer in the *n*-In_2Se_3–*p*-GaSe heterostructures should be taken into account in device applications, in particular, in radiation-stable converters for the visible and near infrared spectral range.

REFERENCES

1. S. I. Drapak and Z. D. Kovalyuk, Pis'ma Zh. Tekh. Fiz. **27** (18), 1 (2001) [Tech. Phys. Lett. **27**, 755 (2001)].
2. V. A. Manasson, Z. D. Kovalyuk, S. I. Drapak, and V. N. Katerinchuk, Electron. Lett. **26** (10), 664 (1990).
3. C. Julien, M. Eddrief, M. Balkanski, *et al.*, Phys. Status Solidi A **88** (2), 687 (1985).
4. C. De Blasi, A. V. Drigo, G. Micocci, and A. Tepore, J. Cryst. Growth **94** (2), 455 (1989).
5. G. Micocci, A. Tepore, R. Rella, and P. Siciliano, Phys. Status Solidi A **126** (2), 437 (1991).
6. *Landolt-Börnstein: Numerical Data and Functional Relationships in Science and Technology, New Series*, Group III: *Crystal and Solid State Physics*, Ed. by O. Madelung (Springer-Verlag, Berlin, 1983), Vol. 17f.
7. A. G. Milnes and D. L. Feucht, *Heterojunctions and Metal-Semiconductor Junctions* (Academic, New York, 1972; Mir, Moscow, 1975).
8. T. V. Blank, Yu. A. Gol'berg, E. V. Kalinina, *et al.*, Fiz. Tekh. Poluprovodn. (St. Petersburg) **35** (5), 550 (2001) [Semiconductors **35**, 529 (2001)].
9. J. Martinez-Pastor, A. Segura, J. L. Valdes, and A. Chevy, J. Appl. Phys. **62** (2), 1477 (1987).
10. R. R. Daniels, G. Margaritondo, C. Quaresima, *et al.*, J. Vac. Sci. Technol. A **3**, 979 (1985).
11. A. Q. Chynoweth, W. L. Feldman, and R. A. Logan, Phys. Rev. **121**, 684 (1961).
12. S. V. Bulyarskiĭ and N. S. Grushko, *Generation-Recombination Processes in Active Elements* (Mosk. Gos. Univ., Moscow, 1995).

Translated by P. Pozdeev

Technical Physics Letters, Vol. 28, No. 9, 2002, pp. 711–713. Translated from Pis'ma v Zhurnal Tekhnicheskoĭ Fiziki, Vol. 28, No. 17, 2002, pp. 9–15.

The Electrical and Photoelectrical Properties of *n*-In_2Se_3–*p*-InSe Heterostructures

S. I. Drapak, V. V. Netyaga, and Z. D. Kovalyuk

Frantsevich Institute of Material Sciences Problems (Chernivtsi Department), National Academy of Sciences of Ukraine, Chernivtsi, Ukraine

e-mail: chimsp@unicom.cv.ua

Received March 25, 2002

Abstract—The current–voltage and voltage–capacitance characteristics of an originally fabricated photosensitive, radiation-stable *n*-In_2Se_3–*p*-InSe heterostructure were measured at liquid nitrogen temperature and in the temperature interval from 230 to 330 K. It is established that the direct currents are determined (i) by the thermoemission of carriers and their recombination at the interface and (ii) by tunneling via local centers. The reverse currents are also due to the tunneling via local centers. The spectral dependence of the relative quantum efficiency of the heterostructure is presented. © *2002 MAIK "Nauka/Interperiodica"*.

Indium monoselenides InSe and In_2Se_3 belong to a broad class of layered semiconductors. While the former compound has been employed in a number of photosensitive diode structures (see, e.g., [1, 2]), the latter compound was used in such devices only once [2]. Taking into account that InSe crystals contain a number of defects and the structure of In_2Se_3 is highly defective, we may conclude that both semiconductors possess increased stability with respect to ionizing radiation. Therefore, it would be of practical interest to create photosensitive structures based on these materials.

Below we present the results of investigation of the charge transfer mechanisms in the original photosensitive, radiation-stable anisotype *n*-In_2Se_3–*p*-InSe heterostructure, which can be of interest for developing methods of optimization of the main photoelectrical characteristics of such structures.

The *n*-In_2Se_3–*p*-InSe heterojunctions were prepared using *p*-InSe:Cd and *n*-In_2Se_3 possessing a hexagonal α phase structure. The charge carrier concentrations in the initial semiconductors, determined from room-temperature Hall effect measurements, were $p = 5 \times 10^{13}$ cm^{-3} (*p*-InSe) and $n = 4 \times 10^{17}$ cm^{-3} (*n*-In_2Se_3). The heterostructures were prepared by bringing the two materials into tight optical contact. The ohmic contacts were prepared by applying In–Ga eutectics, followed by fusing In on the side of In_2Se_3 and a silver paste composition on the InSe side. The originally fabricated heterostructure is a promising material for photosensitive devices. The open-circuit voltage measured on the structures illuminated at a power density of 100 mW/cm^2 was ~0.35 V. The samples were characterized by measurements of the of the current–voltage (*J*–*V*) characteristics at various temperatures, capacitance–voltage (*C*–*V*) characteristics, frequency dependence of the capacitance, and spectral dependence of the relative quantum efficiency at room temperatures.

As can be seen from Fig. 1a, direct branches of the *J*–*V* curves of the *n*-In_2Se_3–*p*-InSe heterostructure can be divided into two parts. The initial portion exhibits exponential behavior and can be described by the expression

$$J \sim \exp(eV/nkT), \quad (1)$$

where *n* is the diode coefficient, which retains a constant value $n = 1.66$ in the temperature interval $T = 231$–331 K (Fig. 1a, curves *1*–*3*). As the temperature decreases, the exponential portion becomes smaller to vanish completely at liquid nitrogen temperature (Fig. 1a, curve *4*).

At greater direct bias voltages, the *J*–*V* curve, with an allowance for the base material resistance, in the entire temperature range obeys the relation

$$J = J_0[\exp(A(V - Ir)) - 1], \quad (2)$$

where *r* is the resistance of the InSe layer calculated from the results of impedance measurements at various frequencies. The slope parameter *A* in this region remains virtually the same at all temperatures. In the interval $T = 231$–331 K, the saturation current density J_0 (see Fig. 2a) varies with temperature according to the law $J_0 \sim \exp(-\Delta E/kT)$, where $\Delta E = 0.24$ eV (this value coincides with the activation energy of the acceptor level in InSe [3]).

It should be also noted that the *J*–*V* curve of the *n*-In_2Se_3–*p*-InSe heterostructure at $T = 231$–331 K exhibits a well-pronounced "diode" shape: at a bias voltage of 1.5–2 V, the direct to reverse current ratio is ~10^2. At the same time, the *J*–*V* curve measured at liquid nitrogen temperature possesses a somewhat asymmetric shape. This behavior can be explained taking

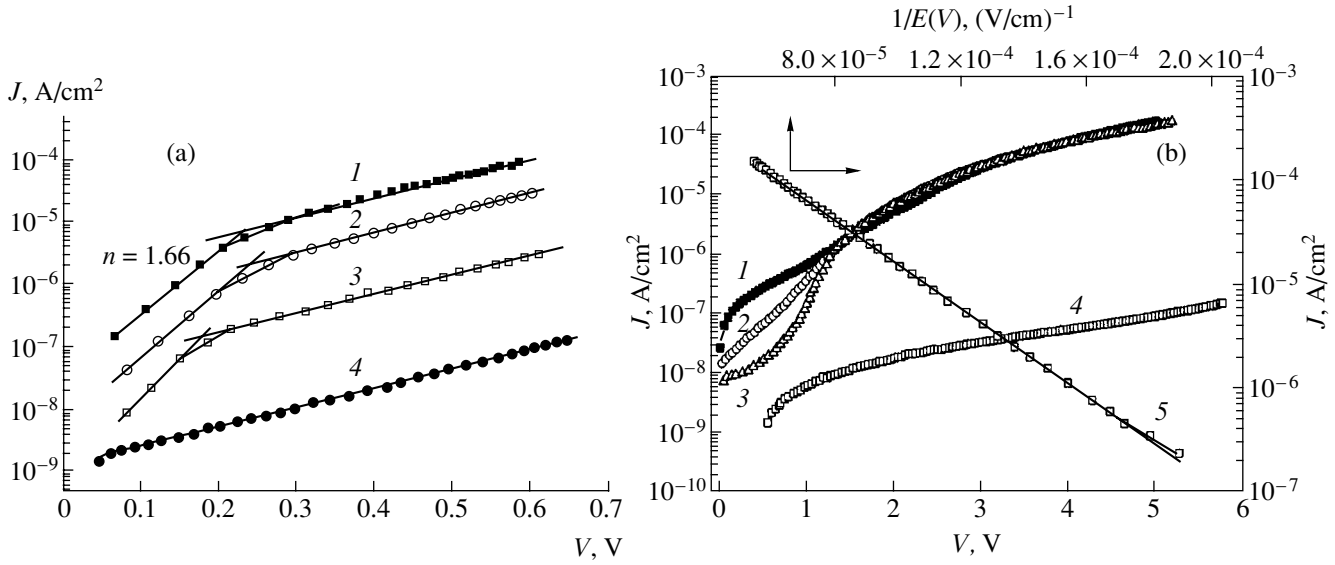

Fig. 1. Direct (a) and reverse (b) current–voltage characteristics of the *n*-In_2Se_3–*p*-InSe heterostructure measured at T = 311 (*1*), 288 (*2*), 231 (*3*), and 77 K (*4*). Curve *5* shows the reverse branch of the characteristic measured at T = 288 K, plotted in the coordinates of $J = f(1/E(V))$.

into account a complicated energy structure of the base *p*-InSe layer. According to [4], in the temperature range T < 170–180 K, *p*-InSe behaves as an *n*-type semiconductor. In our case, this implies that the barrier at T = 77 K vanishes or becomes very small and, hence, the *n*-In_2Se_3–*p*-InSe heterostructure should be considered as a structure of the n^+–*n* type (or as a photoresistor), rather than a diode. Asymmetry of the *J*–*V* curve measured at 77 K reflects violation of the ohmic character of a current contact on the InSe side.

An analysis of the experimental data leads to a conclusion that, in the temperature interval from 231 to 331 K, the total current in a directly biased structure consists of a thermal (first portion of the *J*–*V* curve) and tunneling (second portion) components (Fig. 1a, curves *1*–*3*). Since the resistance of the space-charge region (completely localized in *p*-InSe, where $N_A/N_D \ll 1$) is significantly greater than the resistance of In_2Se_3, the former region is characterized by a maximum electric field strength and, hence, by a maximum probability that carriers (holes) from *p*-InSe will tunnel through the barrier. Simultaneously, In_2Se_3 features thermoemission of electrons which exhibit recombination at the interface. Since the recombination current usually increases more rapidly with the applied voltage, an increase in the bias can lead (according to the tunneling–recombination model [5]) to passage from a characteristic determined by recombination to that controlled by tunneling, in agreement with our observations. All these processes, occurring in a directly biased In_2Se_3–InSe heterostructure, can be schematically illustrated by an energy band diagram (see the inset in Fig. 2b) constructed using published data on the physical parameters of *p*-InSe [4] and In_2Se_3 [6], the concentrations of charge carriers determined in both semiconductors and the values of contact potential difference φ_0 determined from the measured *C*–*V* characteristics.

The reverse branches of the current–voltage characteristic of the *n*-In_2Se_3–*p*-InSe heterostructure measured in the temperature interval T = 321–331 K can be also divided into two parts (Fig. 1b, curves *1*–*3*). In the region of small bias voltages ($|V|$ < 1 V), the room-tem-

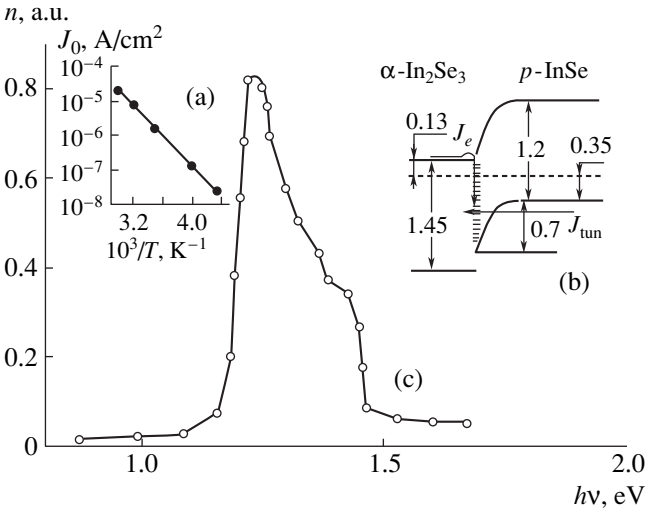

Fig. 2. Characteristics of the *n*-In_2Se_3–*p*-InSe heterostructure: (a) temperature dependence of the saturation current density J_0 of a directly biased structure measured in the region where tunneling is the dominating charge-transfer mechanism; (b) equilibrium energy band diagram (the values of energy parameters are indicated in electronvolts); (c) a typical spectrum $n(h\nu)$ of the relative quantum efficiency at T = 288 K.

perature J–V curve can be described by an expression of the type $J \sim (\varphi_0 - eV)^{1/2}$, which is typical of the generation–recombination processes in the space-charge region [7]. As the reverse bias increases, the current is nearly independent of temperature but exhibits a significant field dependence. This behavior is characteristic of a tunneling mechanism of the charge transfer [8]. In this case, the J–V curve can be approximately described by the power function $J \sim V^4$, which generally corresponds to a soft breakdown.

Detailed analysis of the reverse current–voltage characteristic of the n-In_2Se_3–p-InSe heterostructure will be the subject of a special publication. Here we will only point out that the reverse branches measured at $|V| > 1$ are described by the expression [9]

$$J \sim J_0 \exp\left(-\frac{4}{3}\frac{\sqrt{2m^*}}{eE\hbar}(E_t^*)^{3/2}\right), \quad (3)$$

where E is the electric field strength in the space-charge region and E_t^* is the effective tunneling energy depending on the corresponding level energy. Plotted in coordinates of $J = f(1/E)$, the J–V curves in the region of large fields fit well to a straight line (Fig. 1b, curve 5), which confirms the assumption of tunneling via a deep center. Recalculation of the reverse-bias voltage to the electric field strength in the space-charge region is performed using the relation [5]

$$E(V) = \frac{1}{\varepsilon\varepsilon_0 s}\int_{V-\varphi_0/e}^{V} C(V)dV, \quad (4)$$

which is valid even in the case of a significantly inhomogeneous distribution of impurities in the base semiconductor. In Eq. (4), the integrand represents the capacitance of the space-charge region in the n-In_2Se_3–p-InSe heterostructure as a function of the bias voltage, $C = f(V)$, measured at a frequency of 1 kHz for the forward (from $V - \varphi_0/e$ to 0) and reverse (from 0 to V) variation of the applied voltage; s is the barrier area.

Illumination of the n-In_2Se_3–p-InSe heterostructure from the side of In_2Se_3 (possessing a wider bandgap) gives rise to a photovoltaic effect. The sign of the photo emf depends neither on the photon energy nor on the localization of the probing light spot (the spot diameter was ≈1 mm) on the sample surface, which allows us to relate the observed photoeffect to the existence of a single active region ensuring separation of nonequilibrium charge carriers. In order to determine the relative quantum efficiency n of the heterostructure studied, the photo emf was measured on a linear portion of the luminance–voltage characteristic and the results were normalized to the number of incident photons. Figure 2c shows a typical spectral characteristic $n(h\nu)$ measured at 288 K on an n-In_2Se_3–p-InSe heterostructure illuminated from the side of In_2Se_3. As can be seen from these data, the spectrum of the relative quantum efficiency exhibits a band shape. The longwave edge is determined by the narrowband component and the shortwave edge, by the optical absorption of In_2Se_3 [10]. The maximum of $n(h\nu)$ for the heterostructure stud falls within the region of fundamental absorption of the highly ohmic p-InSe, which can be explained by a certain relation of the electrical parameters of contacting phases resulting in that the active region of the structure is mostly localized in the base component.

In concluding, it should be noted that the data concerning the mechanisms of charge transfer in the n-In_2Se_3–p-InSe heterostructure should be taken into account in applications, in particular, in the development of radiation-stable converters for the visible and near infrared spectral range and during the optimization of design and characteristics of such devices.

REFERENCES

1. J. Martinez-Pastor, A. Segura, J. L. Valdes, and A. Chevy, J. Appl. Phys. **62** (2), 1477 (1987).
2. S. I. Drapak, Z. D. Kovalyuk, V. V. Netyaga, and V. B. Orletskiĭ, Pis'ma Zh. Tekh. Fiz. **28** (17), 1 (2002) [Tech. Phys. Lett. **28**, 707 (2002)].
3. M. C. Martinez-Tomaz, V. Munoz, M. V. Andres, *et al.*, Z. Phys. B **91**, 25 (1993).
4. A. Segura, J. Martinez-Pastor, B. Mari, *et al.*, J. Appl. Phys. **21** (3), 249 (1987).
5. A. G. Milnes and D. L. Feucht, *Heterojunctions and Metal–Semiconductor Junctions* (Academic, New York, 1972; Mir, Moscow, 1975).
6. C. De Blasi, A. V. Drigo, G. Micocci, and A. Tepore, J. Cryst. Growth **94** (2), 455 (1989).
7. V. I. Strikha, *Contact Phenomena in Semiconductors* (Kiev, 1982).
8. S. V. Bulyarskiĭ and A. V. Zhukov, Fiz. Tekh. Poluprovodn. (St. Petersburg) **35** (5), 560 (2001) [Semiconductors **35**, 539 (2001)].
9. O. V. Kurnosova and A. A. Pakhomova, Fiz. Tekh. Poluprovodn. (Leningrad) **20** (10), 1868 (1986) [Sov. Phys. Semicond. **20**, 1171 (1986)].
10. A. V. Novoselova, V. B. Lazarev, Z. S. Medvedeva, *et al.*, *Physicochemical Properties of Semiconductor Substances: A Handbook* (Nauka, Moscow, 1979).

Translated by P. Pozdeev

Technical Physics Letters, Vol. 28, No. 9, 2002, pp. 714–718. Translated from Pis'ma v Zhurnal Tekhnicheskoĭ Fiziki, Vol. 28, No. 17, 2002, pp. 16–24.

The Influence of a Photoinduced Volume Charge on the Weak-Radiation-Induced Interband Photoproduction of Carriers in Semiconductors with Impurity Recombination Centers

V. A. Kholodnov and A. A. Drugova

ORION Research, Development, and Production Corporation, State Scientific Center of the Russian Federation, Moscow, Russia

e-mail: khol.orion@g23.relcom.ru

Received January 15, 2002; in final form, March 29, 2002

Abstract—Analytical expressions for the average concentrations of photogenerated electrons and holes are obtained outside the framework of the quasineutrality approximation in the case of a strong surface recombination in the presence of a single-level impurity recombination centers. It is shown that the quasineutrality approximation becomes incorrect with decreasing sample size in the direction of irradiation. © *2002 MAIK "Nauka/Interperiodica".*

Previously, we reported in papers [1–3] and at conference [4] on the phenomenon of a giant buildup in photocurrent (I_{ph}) during interband photoproduction of carriers in semiconductors with increasing concentration N of the impurity recombination centers. This effect is related primarily to a strongly nonmonotonic dependence of the lifetimes of photoelectrons (τ_n) and photoholes (τ_p) on the impurity concentration N (Fig. 1a; see the text below for the definition of τ_n and τ_p adopted here). It was also demonstrated [1–3] that, as the external field strength E_0 increases, the $I_{ph}(N)$ dependence becomes strongly influenced (even before the onset of field-induced heating) by a photoinduced volume charge density $\Delta\rho$. This is indicative of violation of the quasineutrality condition in the photoexcited plasma of the semiconductor.

In this communication, we demonstrate that, for a sample featuring strong recombination on the illuminated front ($x = 0$) and shadowed rear ($x = W$) surfaces (see the inset in Fig. 1b) with the boundary conditions $\Delta n(0) = \Delta p(0) = \Delta n(W) = \Delta p(W) = 0$, the volume charge density $\Delta\rho$ may significantly influence the average values $\langle\Delta n\rangle$ and $\langle\Delta p\rangle$ of the concentrations of photoelectrons $\Delta n(x)$ and photoholes $\Delta p(x)$, respectively, even for $E_0 = 0$ (Fig. 1b). Unlike previous papers [1–3], we will not assume spatial homogeneity of the interband photoproduction rate density $g(x)$. Nor do we attract the well-known quasineutrality approximation (frequently used for solving such problems—see, e.g., [5, p. 384], [6, p. 311], [7, p. 14] and references therein). As will be shown below, the quasineutrality approximation may lead to unacceptable errors during the calculation of $\langle\Delta n\rangle$ and $\langle\Delta p\rangle$ as functions of N. For example, in the quasineutrality approximation, $\tau_n \gg \tau_p$ always implies that $\langle\Delta p\rangle \ll \langle\Delta n\rangle$; in fact, the reverse relation can also take place (Fig. 2b).

The average value $\langle y\rangle$ of a quantity $y(x)$ is defined as

$$\langle y\rangle = \frac{1}{W}\int_0^W y(x)dx. \quad (1)$$

Following [1–3], let us consider a weakly illuminated nondegenerate semiconductor doped with a shallow, fully ionized donor impurity to a concentration of N_D, in which the recombination proceeds via an acceptor impurity occurring in the neutral (A^0) or singly charged (A^{1-}) states. The concentration of recombination centers in the neutral state is N_0, and in the charged state, $N_- = N - N_0$. The neutral centers trap electrons and thermally generate holes, whereas the charged centers trap holes and thermally generate electrons. The situation under consideration corresponds to a single recombination level. Under stationary conditions, the rates of recombination and generation of electrons (R_n) and holes (R_p), related to the trapping of carriers on the recombination level and the thermal generation of carriers from this level to the free bands, must be equal to each other:

$$R_n \equiv (nN_0 - \delta^{-1}n_eN_-)w_n = R_p \equiv (pN_- - \delta p_eN_0)w_p. \quad (2)$$

Here, n_e and p_e are the equilibrium values of the electron (n) and hole (p) concentrations; w_n and w_p are the probabilities of trapping electrons and holes on the cor-

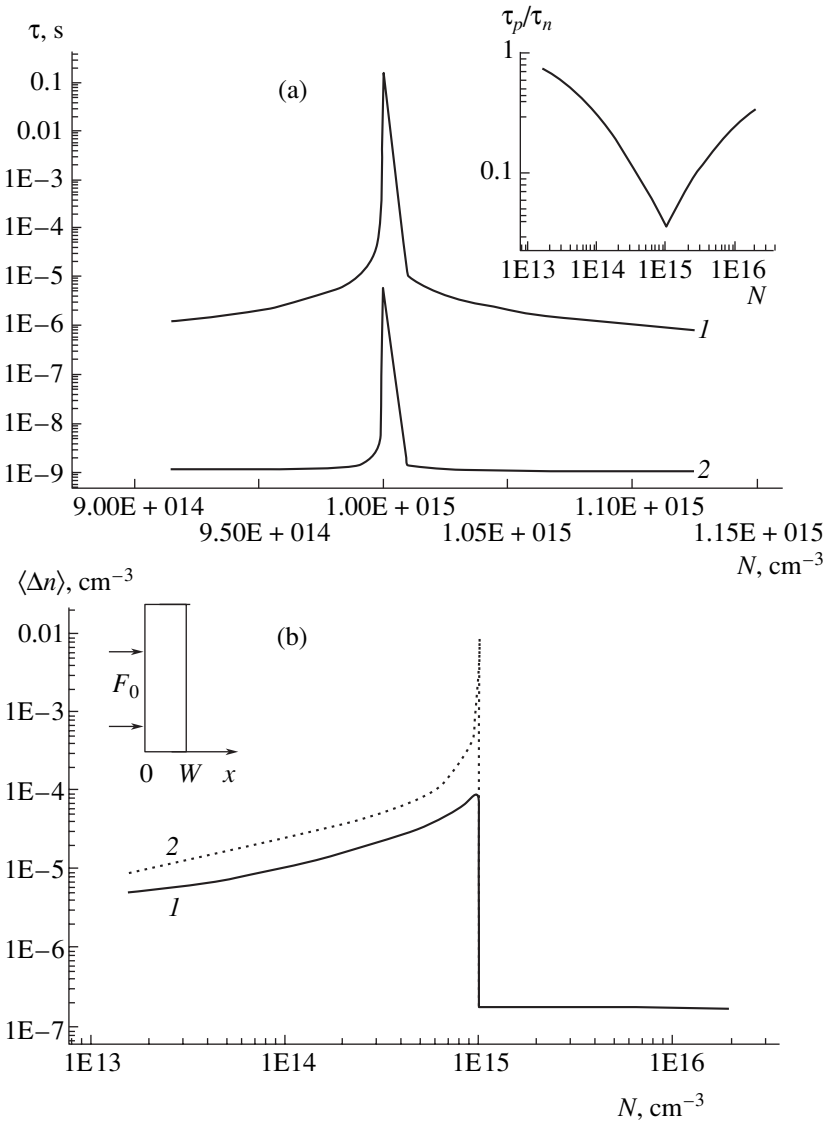

Fig. 1. (a) Plots of the lifetimes of photoelectrons (τ_n curve *1*) and photoholes (τ_p, curve *2*) versus N (the concentration of impurity recombination centers) in the vicinity of maxima of the functions $\tau_n(N)$ and $\tau_p(N)$ for the recombination level E_{t2} lying 0.24 eV below the middle of the bandgap $E_g/2$ of GaAs (the inset shows the ratio τ_p/τ_n versus N for the recombination level E_{t1} lying 0.42 eV below $E_g/2$ of GaAs). (b) Plots of the average concentration of photoelectrons $\langle\Delta n\rangle$ for levels E_{t1} (curve *1*) and E_{t2} (curve *2*) versus N (the inset shows a diagram of the sample exposed to the light flux F_0 along the x axis). The calculations were performed for the temperature $T = 300$ K; shallow donor concentration $N_D = 10^{15}$ cm^{-3}; sample thickness in the direction of irradiation (x axis) $W = 10^{-3}$ cm; light absorption coefficient $\gamma = 10^4$ cm^{-1}; ratio of the hole and electron trapping probabilities $\theta \equiv w_p/w_n = 10^2$, $w_n = 10^{-8}$ cm^3/s; electron and hole diffusion coefficients $D_n = 221$ cm^2/s and $D_p = 10.4$ cm^2/s, respectively [5, 10]; photon flux density $F_0 = 1$ cm^{-2} s^{-1}.

responding impurity center; and $\delta = N_-^e/N_0^e$, where N_-^e and N_0^e are the equilibrium concentrations of the acceptor in the A^{1-} and A^0 charged states, respectively.

In the case of low radiation intensity (realized in threshold photodetectors [7]), we may employ a linear approximation with respect to the incident light flux F_0. Linearizing relations (2) with respect to small deviations $\Delta N_0(x) = N_0(x) - N_0^e = \Delta N_-(x) = N_-^e - N_-(x)$, $\Delta n(x) = n(x) - n_e$, $\Delta p(x) = p(x) - p_e$ from equilibrium and using the Poisson equation,

$$\frac{\partial \Delta E}{\partial x} = \frac{4\pi}{\epsilon}\Delta\rho(x) \equiv \frac{4\pi}{\epsilon}q[\Delta p(x) - \Delta n(x) - \Delta N_-(x)], \quad (3)$$

and the condition of semiconductor neutrality in the thermodynamic equilibrium [8, 9],

$$N = n_t \frac{1+\delta}{2\delta^2} f(\delta), \tag{4}$$

we arrive at the relations

$$R_n = \frac{\Delta n}{\tau_n} + a_n \frac{\partial \Delta E}{\partial x}, \quad R_p = \frac{\Delta p}{\tau_n} - a_p \frac{\partial \Delta E}{\partial x},$$
$$\Delta p(x) = \frac{\tau_p}{\tau_n}\Delta n(x) + (a_n + a_p)\tau_p \frac{\partial \Delta E}{\partial x}, \tag{5}$$

where

$$\tau_n = \frac{2\delta^2}{f(\delta)} \frac{\theta f(\delta) + (1+\delta)(\theta B + \delta)}{[\delta A + (2+\delta)B + \delta^3] w_p n_t},$$
$$\tau_p = \frac{2\delta}{f(\delta)} \frac{B + (A + \theta B)\delta + (\theta B + \delta)\delta^2}{[\delta A + (2+\delta)B + \delta^3] w_p n_t}, \tag{6}$$

$$a_n = \frac{\epsilon}{8\pi q} \frac{(1+\delta) f(\delta) w_p n_t}{\theta f(\delta) + (1+\delta)(\theta B + \delta)},$$
$$a_p = \frac{\epsilon}{2\pi q} \frac{(1+\delta^{-1}) F(\delta) w_p n_t}{B + (A + \theta\delta)\delta + (\theta B + \delta)\delta^2}, \tag{7}$$

$$f(\delta) = B + A\delta - \delta^2, \quad \delta = N_-^e / N_0^e, \quad A = 2N_D / n_t,$$
$$B = 4p_t / n_t = (2n_i / n_t)^2; \quad \theta = w_p / w_n; \tag{8}$$

$n_t = 2n_e/\delta$ and $p_t = p_e\delta/2$ are the values of n_e and p_e when the recombination level coincides wit the Fermi level; n_i is the intrinsic carrier concentration; ϵ is the dielectric permittivity; q is the electron charge; and ΔE is the photoinduced electric field strength. In expressions (5) for R_n and R_p, the terms $\Delta n/\tau_n$ and $\Delta p/\tau_p$ represent the rates of recombination of nonequilibrium electrons and holes (whereby τ_n and τ_p are their lifetimes) in the quasineutrality approximation (i.e., at sufficiently small $|\Delta\rho|$ values). This terminology for τ_n and τ_p values will be retained in the case of a non-quasineutral photoexcited plasma, so that τ_n and τ_p are independent of the coordinate x.

Using relations (1), (3)–(8), expressions for the electron (ΔI_n) and hole ($\Delta I_p = -\Delta I_n$) photocurrents, and the continuity equations for ΔI_n and ΔI_p, we obtain the relations

$$\langle \Delta n \rangle = \eta_n \langle g \rangle, \quad \langle \Delta\rho \rangle = \eta_\rho \langle g \rangle,$$
$$\langle \Delta p \rangle = \eta_p \langle g \rangle, \quad \langle \Delta N_- \rangle = \eta_n \langle g \rangle, \tag{9}$$

where

$$\eta_n = T + \frac{\gamma \coth(\gamma W/2)}{(k_2^2 - k_1^2) D_n} \times \sum_{i=1}^{2} (-1)^{i-1} \frac{k_i \alpha_{3-i}}{\gamma^2 - k_i^2} \tanh\left(\frac{k_i W}{2}\right), \tag{10}$$

$$\eta_\rho = -\frac{\epsilon}{4\pi} \frac{\gamma \alpha_1 \alpha_2}{(\mu_n n_e - a_n) L_n^2} \times \left\{ \Lambda^3 - \frac{\coth(\gamma W/2)}{k_2^2 - k_1^2} \sum_{i=1}^{2} (-1)^i \frac{k_i}{\gamma^2 - k_i^2} \tanh\left(\frac{k_i W}{2}\right) \right\}, \tag{11}$$

$$\eta_p = \frac{4\pi}{\epsilon}(a_n + a_p)\tau_p \eta_\rho + \frac{\tau_p}{\tau_n}\eta_n,$$
$$\eta_N = \eta_p - \eta_n - \frac{1}{q}\eta_\rho, \tag{12}$$

$$T = \frac{(1/\xi L_p^2) - \gamma^2}{D_n(\gamma^2 - k_1^2)(\gamma^2 - k_2^2)}, \quad \Lambda^3 = \frac{\gamma}{(\gamma^2 - k_1^2)(\gamma^2 - k_2^2)},$$
$$\alpha_{1,2} = k_{1,2}^2 L_n^2 - 1, \tag{13}$$

$$k_{1,2} = \sqrt{\frac{L^2 \mp \sqrt{L^4 - 4\xi L_n^2 L_p^2}}{2\xi L_n^2 L_p^2}},$$

$$\xi = \frac{2(a_n + a_p)\delta}{(\delta^2 \mu_n + B\mu_p) n_t} \equiv \xi_n + \xi_p,$$
$$L_0^2 = \frac{\delta^2 \tau_p + B\tau_n}{B + b\delta^2} D_n \equiv D_0^n \tau_n, \tag{14}$$

$$L^2 = L_0^2 + \xi_p L_p^2 + \xi_p L_n^2,$$

$$L_p^2 = D_p \tau_n, \quad L_n^2 = D_n \tau_n,$$
$$\langle g \rangle = \frac{(1-R)F_0}{W} \frac{1 - \exp(-\gamma W)}{1 - R\exp(-\gamma W)}, \tag{15}$$

$$g(x) = \frac{(1-R)\gamma F_0}{1 - R^2 \exp(-2\gamma W)} \times [\exp(-\gamma x) + R\exp(\gamma x - 2\gamma W)]; \tag{16}$$

R and γ are the light reflection and absorption coefficients; μ_n, μ_p and D_n, D_p are the mobilities and diffusion coefficients of electrons and holes, respectively; L_0 and D_0^n are the ambipolar diffusion length and the diffusion coefficient of electrons in the quasineutrality approximation, respectively [1–3]; and ξ is a small dimensionless parameter characterizing deviation of

the photoexcited plasma in the semiconductor [1, 3] from the quasineutrality condition (for which $a_n = a_p = \xi = 0$).

Thus, expressions (4) and (6)–(16) determine the average concentrations $\langle\Delta n\rangle$ and $\langle\delta p\rangle$ as functions of N in the parametric form (with the ratio $\delta = N_-^e/N_0^e$ being the parameter) outside the framework of the quasineutrality approximation. These dependences (Figs. 1b and 2) will be called exact because, in the approximation linear with respect to F_0, they provide adequate description of $\langle\Delta n\rangle$ and $\langle\delta p\rangle$ (in contrast to the values $\langle\Delta\tilde{n}(N)\rangle$ and $\langle\Delta\tilde{p}(N)\rangle$ obtained in the quasineutrality approximation).

As can be seen in Fig. 1b, the efficiency of carrier photoproduction can grow very strongly with increasing impurity concentration N. To within small corrections, the concentrations $\langle\Delta n\rangle$ and $\langle\Delta p\rangle$ as functions of N reach maxima $\langle\Delta n\rangle_{\max}$ and $\langle\Delta p\rangle_{\max}$ at the same point $N = \hat{N} = N_D$ as the corresponding lifetimes (Fig. 1) [8, 9] and then exhibit a sharp drop. The influence of a photoinduced volume charge at $N = \hat{N}$ is illustrated in Fig. 2, from which it is seen that, as the sample thickness W decreases, the quasineutrality approximation leads to an error reaching up to several orders of magnitude. Let us make some comments to Figs. 1b and 2.

The lengths L and $L_1 \equiv 1/k_1$ are nearly equal to L_0 (to within small corrections), while $L_n > L_1 > L_2 \equiv 1/k_2$. For $W \ll L_0$, we obtain $\langle\Delta\tilde{n}\rangle = f(W, \gamma)/D_0^n$ and $\langle\Delta\tilde{p}\rangle = f(W, \gamma)/D_0^p$, where $D_0^p = (\tau_n/\tau_p)D_0^n$ is the ambipolar diffusion coefficient of holes and $f(W, \gamma)$ is a function independent of the lifetimes τ_n and τ_p. On the other hand, for a sufficiently strong inequality $W \ll L_2$ (when $L_p \gg W$ as well), expressions (4) and (6)–(16) yield $\langle\Delta n\rangle = f(W, \gamma)/D_n$ and $\langle\Delta p\rangle = f(W, \gamma)/D_p$. This result implies that photoelectrons and photoholes diffuse independently of each other and, hence, L_2 has a physical meaning of the screening length of the photoinduced electric field.

On both left and right sides of point $N = \hat{N}$, the conditions change to $L_2 \ll L_0$, W and the quasineutrality approximation is valid (to the left from $\hat{N}$, $L_0 < W$ due to small D_0^n). When N passes through point $N = \hat{N}$ toward greater values, length D_0^n dramatically increases (by several orders of magnitude) and then remains constant. Therefore, $L_0 > W$ to the right from $\hat{N}$. This behavior accounts for the asymmetry of $\langle\Delta n\rangle$ as the function of N with respect to point $N = \hat{N}$ and for the plateau at $N > \hat{N}$ (Fig. 1b).

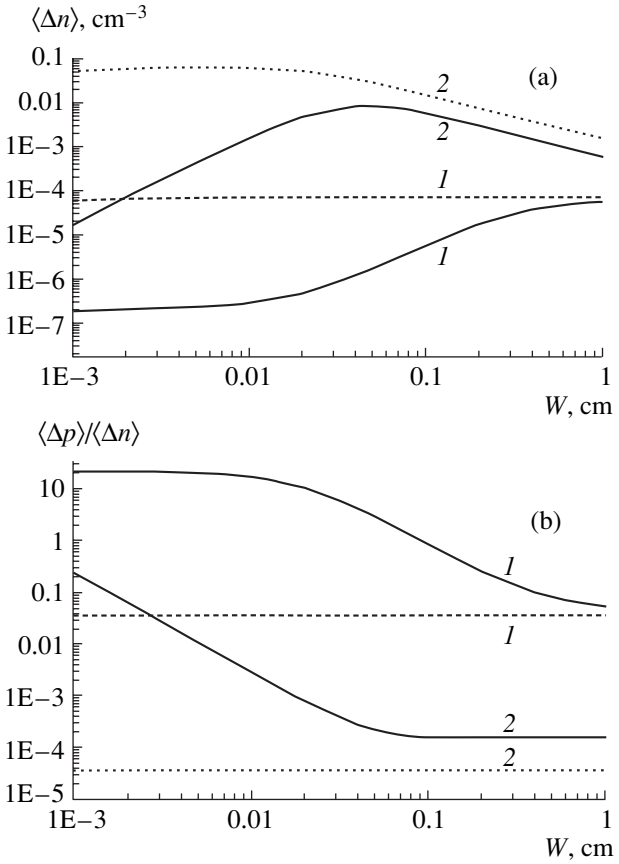

Fig. 2. Plots of (a) $\langle\Delta n\rangle_{\max}$ and (b) $\langle\Delta p\rangle_{\max}/\langle\Delta n\rangle_{\max}$ versus GaAs sample thickness at the point of maxima of $\langle\Delta n\rangle$ and $\langle\Delta p\rangle$ as the functions of N for the energy levels (*1*) E_{t1} and (*2*) E_{t2}: solid curves show the exact solutions; dashed lines correspond to the quasineutrality approximation. The notation and parameters are the same as in Fig. 1.

At the point $N = \hat{N}$ and in the close vicinity of this point, the length L_2 is so large that a solution in the quasineutrality approximation fails to be valid even for $W \sim 0.1$ cm. Moreover, $\langle\Delta n\rangle_{\max}/\langle\Delta\tilde{n}\rangle_{\max} \longrightarrow D_0^n/D_n \ll 1$ and $\langle\Delta p\rangle_{\max}/\langle\Delta n\rangle_{\max} \longrightarrow D_n/D_p \cong 20$ (although $\tau_p \ll \tau_n$, see Fig. 1a) with decreasing W. For $\gamma^{-1} \ll W$ and a sufficiently strong inequality $W \ll L_n$, the total number of photoelectrons becomes proportional to W (because of reduced recombination at the shadowed rear side) and $\langle\Delta n\rangle_{\max}$ as the function of W exhibits a plateau. For the same reasons, $\langle\Delta n\rangle_{\max}$ as the function of W exhibits a plateau at $\gamma^{-1} \ll W \ll L_0$. However, the "height" and width of the latter plateau are much greater than those of the "true" plateau (Fig. 2a, curve *1*). Note that, since $L_2 \approx L_0$ for the energy level E_{t2}, the solution in the quasineutrality approximation differs at least several times from the exact solution even for $W \longrightarrow \infty$ (Fig. 2, curve *2*).

Acknowledgments. This study was supported by the Russian Foundation for Basic Research, project no. 99-02-17415.

REFERENCES

1. V. A. Kholodnov, Pis'ma Zh. Éksp. Teor. Fiz. **67** (9), 655 (1998) [JETP Lett. **67**, 685 (1998)].
2. V. A. Kholodnov and A. A. Drugova, Pis'ma Zh. Tekh. Fiz. **25** (5), 1 (1999) [Tech. Phys. Lett. **25**, 167 (1999)].
3. V. A. Kholodnov, Proc. SPIE **3819**, 98 (1999).
4. V. A. Kholodnov, A. A. Drugova, and N. E. Kurochkin, in *Proceedings of the 25th International Conference on the Physics of Semiconductors, Osaka, Japan, 2000*, Part II, p. 1445.
5. R. A. Smith, *Semiconductors* (Cambridge Univ. Press, Cambridge, 1978; Mir, Moscow, 1982).
6. V. L. Bonch-Bruevich and S. G. Kalashnikov, *Physics of Semiconductors* (Nauka, Moscow, 1990).
7. A. Rogalski *et al.*, *Infrared Photon Detectors* (SPIE Optical Engineering Press, Bellingham, 1995).
8. A. A. Drugova and V. A. Kholodnov, Solid-State Electron. **38** (6), 1247 (1995).
9. V. A. Kholodnov, Fiz. Tekh. Poluprovodn. (St. Petersburg) **30** (6), 1011 (1996) [Semiconductors **30**, 538 (1996)].
10. S. Sze, *Physics of Semiconductor Devices* (Wiley, New York, 1981; Mir, Moscow, 1984).

Translated by P. Pozdeev

Technical Physics Letters, Vol. 28, No. 9, 2002, pp. 719–721. Translated from Pis'ma v Zhurnal Tekhnicheskoĭ Fiziki, Vol. 28, No. 17, 2002, pp. 25–30.

Hydrodynamic Effects Responsible for the Modification of Polysaccharides in an Aqueous Solution under Laser Irradiation

G. A. Baranov, A. A. Belyaev, S. B. Onikienko, S. A. Smirnov, and V. V. Khukharev

Efremov Institute of Electrophysical Equipment, St. Petersburg, Russia
e-mail: laser@mail.rcom.ru
State Military-Medical Academy, St. Petersburg, Russia
Received December 28, 2001; in final form, April 2, 2002

Abstract—An attempt to determine factors responsible for the degradation of polysaccharide molecules in aqueous solutions under the action of laser radiation was undertaken. For this purpose, free-falling drops of water containing polysaccharides were irradiated by a laser beam and the corresponding hydrodynamical model was constructed. Laser irradiation of a drop of an aqueous solution of polysaccharides leads to the formation of oligosaccharides which can be applied in medicine. © *2002 MAIK "Nauka/Interperiodica"*.

Previously [1], we experimentally demonstrated that exposure of free-falling water drops containing polysaccharides to a CO_2 laser beam leads to degradation (depolymerization) of large molecules and the formation of low-molecular-weight fractions, which are highly effective in the immunotherapy of infectious and oncologic disorders. In order to determine factors responsible for the laser-induced degradation of macromolecules, we conducted a series of experiments with aqueous polysaccharide solutions and performed hydrodynamical model calculations.

Experimental. The experimental setup included a continuous CO_2 laser (λ = 10.6 μm) with an output power of up to 220 W. The free-falling aqueous drop diameter was d = 2.6 mm (±12%). The drop velocity in the zone of laser irradiation was v = 0.485 m/s, the laser beam diameter was d_1 = 1.6 mm, and the duration of laser beam action upon the drop was t = 8.7 ms.

Below we present an analysis of the channels of redistribution of the laser energy incident upon a falling drop. The amount of energy absorbed in the drop is $E_2 = E_1 - (E_3 + E_4)$, where E_1 is the incident energy, E_3 is the reflected energy, and E_4 is the scattered energy. Calculations using the Fresnel formulas [2] showed that the radiation with λ = 10.6 μm reflected from the drop can be ignored, that is, $E_3 = 0$. Measurements of the laser radiation power transmitted through a cloud of water vapor showed no signal attenuation to within the measuring system sensitivity (below 5%), so that $E_4 = 0$. Thus, we may assume that $E_2 = E_1$. The value of E_1 measured with the aid of an IR detector was related to the total laser power Q as $E_1 = 7 \times 10^{-3}Q$. All the laser beam energy is absorbed in a thin liquid layer. Indeed, according to the Lambert–Bouguer law, attenuation of the radiation power in an aqueous layer is described by the equation $K = \exp(-\alpha L_2)$, where L_2 is the absorbing layer thickness [cm], $\alpha = 4\pi\chi/\lambda$ is the Bouguer linear absorption coefficient, and χ is the absorption index (e.g., χ_{H_2O} = 0.091 [3]). For K = 0.001, the absorption depth is L_2 = 64 μm.

The radiation energy absorbed in a drop is spent for heating (E_4), evaporating (E_5), and causing the drop to deviate from a vertical trajectory $E_1 - (E_4 + E_5)$. Estimates based on the experimentally measured velocity of such deviation showed that the corresponding energy is much smaller than E_4 and E_5. The value of E_4 was determined by directly measuring the temperature of laser-heated water in a thermoinsulated container. In the range of incident laser powers from 50 to 216 W, we obtained a relation $E_4 = 2{,}1 \times 10^{-3}Q$; at the same time, $\Delta T = 5.5 \times 10^{-2}Q$, where $\Delta T = T_d - T_0$ is a change in the water temperature averaged over the entire volume (T_0 = 288 K). Assuming that water evaporates from the drop at 100°C, the evaporation can be written as $E_5 = m[c_p(373 - T_0) + r]$, where r is the heat of vaporization and m is the mass of evaporated water. Calculated by these formulas, the mass of evaporated water accounts for less than 5% of the drop mass. This estimate agrees with experimental data on the difference of water volumes before and after laser irradiation of the drop.

The experimental data obtained indicate that the degradation of polysaccharides reported in [1] cannot be explained by electromagnetic action of the laser beam (small penetration depth and small fraction of evaporated water). Nor can we attribute the observed effects to a radiation-induced heating of the drop (small temperature increment: ΔT = 2.75 K for Q = 50 W). Then, the only possible explanation is based on the

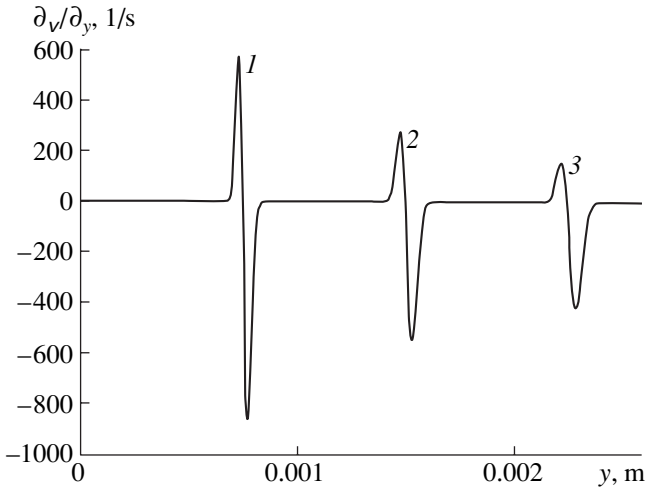

The rate of water straining calculated for $L = 20$ μm and $\delta P = 1.3 \times 10^5$ Pa at $t = 0.5$ (*1*), 1 (*2*), and 1.5 μs (*3*).

hydrodynamic factors: volume expansion, recoil vapor pressure, and explosive boiling of the surface liquid layer. In order to determine the role of the hydrodynamic action upon polysaccharide molecules, we constructed a one-dimensional model.

Model calculations. We have analyzed the state of water along the line parallel to the laser beam direction, originating from the center of the frontal surface of the drop at a maximum intensity of radiation. The calculations were performed for the average values of parameters. For a laser beam diameter of 1.6 mm, the duration of exposure of the central point on the drop surface is 3.2 ms. The average radiation power density was $I_1 = 0.25 \times 10^8$ W/m^2 for $Q_1 = 50$ W and $I_2 = 1 \times 10^8$ W/m^2 for $Q_2 = 200$ W. The temperature was calculated using an equation, written in the coordinate system moving at the vapor velocity v_s [4],

$$\rho c_p \frac{\partial T}{\partial t} - \rho c_p v_s(T_s) \frac{\partial T}{\partial y} = \lambda \frac{\partial^2 T}{\partial y^2} + \alpha I e^{-\alpha y}, \qquad (1)$$

with a boundary condition $\lambda \partial T/\partial y = \rho h v_s(T_s)$, where t is the current time, y is the coordinate along the normal to the surface, λ is the thermal conductivity, c_p is the heat capacity, h is the specific vaporization heat for water, ρ is the density, and T_s is the surface temperature. The vapor velocity v_s was calculated using formulas [4] for two values of the condensation coefficient $\gamma = 0.04$ and 1, the large scatter of which reflects the uncertainty of data on the evaporation process.

We obtained the following values of temperatures T_s and T_{max} (maximum temperature inside the absorbing layer) reached by the end of irradiation of the central zone: $T_s = 605$ K, $T_{max} = 632$ K (for $Q_1 = 50$ W, $\gamma = 0.04$); $T_s = 389$ K, $T_{max} = 437$ K (for $Q_1 = 50$ W, $\gamma = 1$); $T_s = 705$ K, $T_{max} = 790$ K (for $Q_2 = 200$ W, $\gamma = 0.04$); and $T_s = 418$ K, $T_{max} = 475$ K (for $Q_2 = 200$ W, $\gamma = 1$). These estimates show that the rate of heating significantly depends on the condensation coefficient. Heating of the liquid can proceed both in the regime of evaporation and in the form of explosive boiling (beginning almost instantaneously at $T = 600$ K), producing a considerable force action upon the system.

The parameters of an acoustic pulse generated by the volume expansion were determined for the initial time instant. This process probably determines a minimum level of the acoustic signal acting upon macromolecules, before the onset of intensive evaporation or explosive boiling. It was assumed that nonequilibrium overheating of a layer with a thickness of $L = 20$ μm (over which about 90% of the deposited energy is absorbed) is determined by the quantity $\delta T = \tau(dT/dt)$, where τ is the time required for sound to travel across the absorbing layer (for $c = 1500$ m/s; $\tau = L/c = 1.33 \times 10^{-8}$ s) and dT/dt is the heating rate averaged over the layer. For $Q_1 = 50$ W, we obtained $dT/dt = 1 \times 10^5$ K/s, which yields $\delta T \sim 1.33 \times 10^{-3}$ K. At 20°C, the coefficient of thermal expansion is $\alpha = 2 \times 10^{-4}$ K^{-1}, from which it follows that the pressure pulse at the initial time instant for $Q_1 = 50$ W is on the order of $\delta P \sim 1.3 \times 10^5$ Pa. This pulse leads to perturbation of the parameters of water, which was calculated by the equations

$$\frac{\partial \rho}{\partial t} + \frac{\partial \rho v}{\partial y} = 0, \qquad (2)$$

$$\frac{\partial \rho v}{\partial t} + \frac{\partial (\rho v^2 + p)}{\partial y} = \mu \frac{\partial^2 v}{\partial y^2}, \qquad (3)$$

where t is the current time, v is the velocity, p is the pressure, and μ is the viscosity. The calculations were performed for an isothermal liquid in an immobile coordinate system, since the velocity of propagation of the compression wave is significantly higher than the rate of heat transfer from the surface layer. The relation between the density and pressure of water was described by Tate's law. The boundary conditions on the free surface were set as $\partial y/\partial y = 0$, $\partial p/\partial y = 0$. The calculation aimed at estimating the rate of water straining ($\partial v/\partial y$), from which it is possible to determine conditions for the onset of deformation of macromolecules contained in the drop.

Calculated distributions of the rate of water straining at various time instants are presented in the figure. The pressure jump δP in the surface layer was set only at the initial time instant. As can be seen, the pulse propagation velocity is on the order of 1500 m/s, which corresponds to the sound velocity in water. The pulse amplitude decreases with increasing distance from the surface. According to [5], changes in the shape of a macromolecule are small until the absolute value of the

rate of straining of the surrounding medium is smaller than

$$(\partial v/\partial y)_{cr} = kT/(\mu\langle h^2\rangle^{3/2}), \quad (4)$$

where k is the Boltzmann constant and $\langle h^2\rangle^{1/2}$ is the rms distance between the free ends of a macromolecule. For a molecule of amylopectin, $\langle h^2\rangle^{1/2} = 0.214$ μm [6], which corresponds to a critical straining rate of $(\partial v/\partial y)_{cr} = 500$ s^{-1}. This coincides in the order of magnitude with the straining rate calculated for water at a radiation power of $Q_1 = 50$ W (see the figure). For $Q_2 = 200$ W and $t = 0.5$ μs, a maximum shear rate $\partial v/\partial y = 6825$ s^{-1} is one order of magnitude higher than $(\partial v/\partial y)_{cr}$. Thus, laser powers employed in our experiments allow a critical water straining rate to be reached at which the molecules of amylopectin begin to change in shape. This explains the process of laser-induced modification of polysaccharides reported in [1].

Acknowledgments. The authors are grateful to N.F. Morozov, D.A. Indeĭtsev, A.B. Freĭdin, and B.N. Semenov (Institute of Mechanical Engineering Problems, Russian Academy of Sciences, St. Petersburg) for fruitful discussions at all stages of this study. Special thanks to A.K. Zinchenko, P.G. Lyashed'ko, and G.V. Tsvetkov for participating in the creation and use of the experimental setup.

This study was supported by the Russian Foundation for Basic Research, project no. 01-01-00325.

REFERENCES

1. G. A. Baranov, S. B. Onikienko, V. V. Khukharev, *et al.*, in *Proceedings of the 8th International Congress of European Medical Laser Association and 1st Russian Congress of Medical Laser Association, Moscow, 2001*, p. 15.
2. D. V. Sivukhin, *General Course of Physics. Optics* (Nauka, Moscow, 1980).
3. V. M. Zolotarev, V. N. Morozov, and E. V. Smirnova, *Optical Constants of Natural and Technical Media* (Khimiya, Leningrad, 1984).
4. V. V. Korneev, Teplofiz. Vys. Temp. **28** (3), 536 (1990).
5. J. Batchelor, in *Theoretical and Applied Mechanics: Proceedings of the 14th IUTAM Congress, Delft, The Netherlands, 1976*, Ed. by W. T. Koiter (North-Holland, Amsterdam, 1977; Mir, Moscow, 1979).
6. M. Fiedorowicz and P. Tomasik, Carbohydrate Polym. **45** (1), 79 (2001).

Translated by P. Pozdeev

Technical Physics Letters, Vol. 28, No. 9, 2002, pp. 722–724. Translated from Pis'ma v Zhurnal Tekhnicheskoĭ Fiziki, Vol. 28, No. 17, 2002, pp. 31–36.

The Effect of a Diaphragm on the Vortex Thermoinsulation of Arc in a Plasmatron Channel

V. M. Lelevkin and V. F. Semenov

Kyrgyz-Russian Slavonic University, Bishkek, Kyrgyzstan

e-mail: aral@krsu.edu.kg

Received January 14, 2002; in final form, March 18, 2002

Abstract—The pattern of gas (argon) flow and heating in a diaphragmed plasmatron channel is calculated within the framework of an equilibrium magnetogasdynamic model, depending on the diaphragm position and hole size and on the gas flow rate and twist momentum. Special features of the arc characteristics in a channel of variable cross section are established for streams with and without twist. *© 2002 MAIK "Nauka/Interperiodica".*

An important factor for the formation of a gas stream with required characteristics in a plasmatron channel is the gasdynamic flow pattern. For example, stabilization of an arc and thermal insulation of the arc from the plasmatron channel walls can be reached by using porous injectors, axial streams, or twisted gas flows [1, 2]. In order to obtain the desired pattern of flow, plasmatron channels are provided with various hollows, steps, diaphragms, interelectrode inserts, etc. [1–4].

The aim of this study was to determine the effect of a diaphragm and the influence of a flow twist on the thermal insulation of arc in a plasmatron channel (Fig. 1) by solving equations of magnetogasdynamics (MGD) for this system.

We assume that processes in the system studied are stationary, the flow is laminar and axisymmetric, the radiation has a volume character, and the plasma occurs in the state of local thermodynamic equilibrium [5]. The MGD equations [5, 6] will be solved in terms of physical variables by a finite-difference method using a SIMPLE procedure [7]. Discretization of the differential equations is performed on a nonuniform lattice (31×151) by the method of control volume, which ensures validity of the laws of mass, momentum, and energy conservation for any group of the control volumes [7]. We will calculate the stream of a plasma ejected from a cathode mouthpiece with an internal radius of $R_0 = 2.5$ mm, a wall thickness of 10 mm, and a flow rate $G_0 = 0.01$ g/s, into a plasmatron channel with a diameter of $2R = 30$ mm, a total flow rate of $G = G_0 + G_1 = 1$, 3, or 6 g/s, a flow twist momentum of $M \sim G_1$ [6], a wall temperature of 300 K, a current of $I = 100$ A, a confuser diaphragm length of 2 cm, a diaphragm hole radius $R_d = 5$ or 10 mm, and a diaphragm position in the channel of $z_d = 2$, 4, 6, …, or 14 cm.

As can be seen from the results of numerical calculations (Figs. 2 and 3), an increase in the flow twist momentum in the diaphragmed channel is accompanied by a qualitative change in distribution of the flow characteristics. In the channel part before diaphragm, the pattern reveals a clear boundary between the plasma stream and the external vortex gas flow, which is indicative of a weak heat and mass transfer between these regions (Fig. 2). The wall heating in this part of the channel is determined by radiation. A maximum distance z_d at which the arc column retains a cylindrical shape does not exceed 5–10 diaphragm calibers ($z_d < 10R_d$ for $R/R_d = 1.5$ and $z_d < 20R_d$ for $R/R_d = 3$). If the diaphragm is absent or shifted to $z_d = 14$ cm, the flow twist effect upon the arc localization in the paraxial region significantly decreases and the distribution of flow characteristics resembles that in the flow without twist.

The presence of a cathode mouthpiece in the channel results in the formation of a recirculation zone behind the output edge, the length of this zone depending on the gas flow rate and twist momentum. In the absence of twist, the recirculation zone expands with increasing gas flow rate and involves plasma from the paraxial region into the vortex motion. The appearance of reverse flows near the axis leads to increased heat

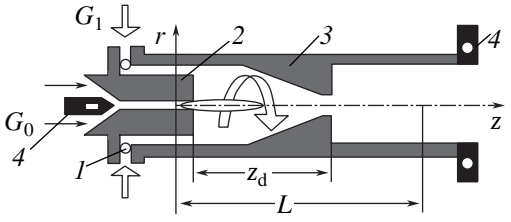

Fig. 1. Schematic diagram of a plasmatron with diaphragmed channel: (*1*) twist device; (*2*) cathode mouthpiece; (*3*) confuser diaphragm; (*4*) electrodes; (*L*) calculation region.

1063-7850/02/2809-0722$22.00 © 2002 MAIK "Nauka/Interperiodica"

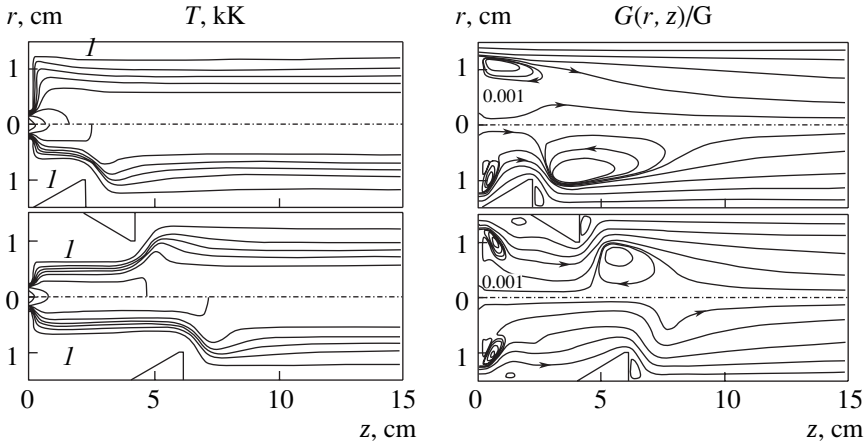

Fig. 2. Effect of the diaphragm position on the field of isotherms (at a 2 kK step) and gas flow lines $G(r, z)/G = \pm 0.001$, 0.01, 0.05, 0.2, 0.6, and 1.2; $R_d = 10$ mm, $I = 100$ A, $G = 6$ g/s, $M \neq 0$.

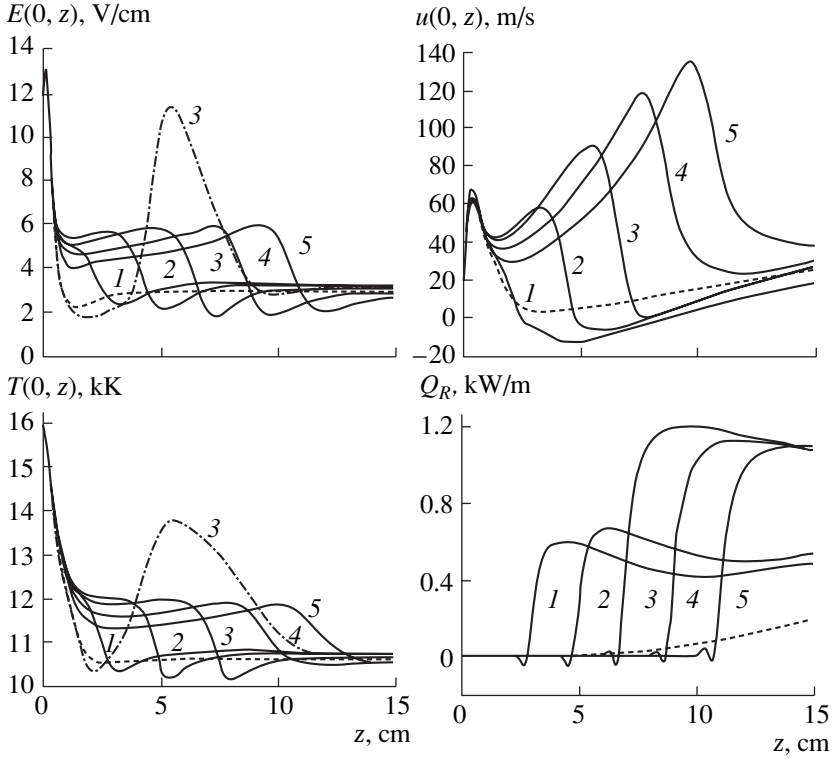

Fig. 3. Axial distributions of the electric field strength, axial flow velocity, axial temperature, and conductive thermal flux to walls depending on the diaphragm position $z_d = 2$ (*1*), 4 (*2*), 6 (*3*), 8 (*4*), 10 cm (*5*). Dashed curves refer to the channel without diaphragm; dash-dot curves refer to the absence of flow twist; $R_d = 10$ mm, $G = 6$ g/s, $I = 100$ A.

and mass exchange between the plasma stream and cocurrent gas flow, nonmonotonic variation of the plasma parameters in both radial and axial directions (Fig. 3), and rapid expansion of the thermal boundary of the arc immediately behind the mouthpiece nozzle edge.

In the presence of twist, no reverse flows appear in the paraxial region before diaphragm (Fig. 2). A recirculation zone is formed only at the outer rib of the mouthpiece edge and is characterized by a much smaller length as compared to the case of untwisted flow. The flow twist increases pressure gradient toward the channel walls, so that the plasma stream is localized in the paraxial region. This pattern is more pronounced with increasing the twist momentum and the diaphragm ratio R/R_d. The peripheral region of the arc features a kind of cylindrical interface characterized by a small radial velocity, which is indicative of a weak heat and mass transfer between the paraxial stream and the main flow.

We can distinguish two regions in the flow: external, in which the tangential velocity w corresponds to the law of quasi-potential flow ($w \sim 1/r$), and internal, where rotation obeys the law of solids ($w \sim r$). This pattern is confirmed in experiment [3]. A maximum of w occurs in the vicinity of the current-carrying boundary and shifts toward the axis with increasing gas flow rate and the diaphragm ratio. The untwisted plasma stream ejected from the mouthpiece is involved into quasi-solid rotation at a distance of $z/R_0 > 1$ from the mouthpiece nozzle edge. As the diaphragm ratio increases to $R/R_d = 1.5$–3, the flow rotation velocity grows and the arc is confined to the channel axis. In the absence of diaphragm, the radial pressure gradient drops and the tangential velocity w significantly decreases, which corresponds to an untwisted gas flow. Therefore, in order to ensure the arc localization in the paraxial region and thermoinsulation from the channel walls, it is necessary both to twist the flow and to diaphragm the channel, positioning the diaphragm at a definite distance z_d from the input section. This result agrees with experimental data on the diaphragmed vortex chambers [2] and confirms a significant dependence of the diameter of the stable surface of an arc plasma flow on the output hole size of the diaphragm.

In the region of a confuser diaphragm, the arc exhibits narrowing with the resulting increase in the gas velocity, current density, and electric field strength. These changes are more pronounced for the flow without twist (Fig. 3). The major amount of gas passes along the confuser surface, while the radial convective thermal flux toward the axis favors return of heat (transferred due to thermal conductivity) back to the arc column and protects the channel walls from overheating. A similar pattern is observed when the gas is injected through porous channel walls.

In the part of the channel behind the confuser diaphragm, recirculation zones in the near-wall region are formed in both twisted and untwisted flows. In the former case, an additional recirculation zone appears in the paraxial region (Fig. 2) and increases in size with the twist momentum. Thus, the gas flow twist suppresses the formation of paraxial reverse flows in the part of the channel before the diaphragm and favors the formation of such flows behind the diaphragm, so that no vortex thermoinsulation of the arc takes place. As the diaphragm is shifted downstream along the channel, the axial flow velocity rapidly increases (Fig. 3, $w_{max} \sim$ 50 m/s), the flow twist parameter $w_{max}/\langle u \rangle$ drops [1], and the region of paraxial reverse flows decreases to vanish completely at $z_d > 6$ cm (Fig. 2). Near the boundary of the region where the plasma touches the channel wall, there is a rapid buildup of conductive thermal flux Q_R (Fig. 3), the maximum value of which decreases upon the formation of a paraxial zone of reverse flows. As the flow twist momentum grows ($M \sim G_1$ [6]), the relative length of the flow separation from the wall at the edge decreases. For example, in the case of $z_d =$ 4 cm, $\Delta h = R - R_d = 10$ mm, and the flow rate varied within $G = 1$–6 g/s, $L_{off}/\Delta h = 9.2$–1.6 with twist and $L_{off}/\Delta h = 9.2$–5.0 without twist. For $z_d > 10R_d$, the influence of twist on the flow pattern behind the diaphragm decreases and $L_{off}/\Delta h$ increases. When the diaphragm ratio R/R_d grows, the value of $L_{off}/\Delta h$ increases in a twisted flow and decreases in the absence of twist.

In extended channels, axial stabilization of the arc can be ensured by arranging diaphragms along the channel. According to the results of calculations, additional twisted gas flows have to be introduced into the channel after each diaphragm in order to provide for a stable paraxial plasma flow. This scheme was realized in experiment [4].

Thus, the results of numerical calculations of the arc characteristics in a plasmatron channel with a cathode mouthpiece show the following:

(i) diaphragming the channel under the conditions of intensive gas flow twist ensures localization of the plasma flow in front of the diaphragm within a narrow paraxial region with a clear thermal interface between the plasma stream and the outer gas flow (vortex thermoinsulation of the plasma);

(ii) extension of the region of stabilization depends on the diaphragm hole size and position in the channel ($z_d < 10R_d$ for $R/R_d = 1.5$ and $z_d < 20R_d$ for $R/R_d = 3$);

(iii) diaphragming the channel in the absence of twist does not provide for arc thermoinsulation from the channel walls;

(iv) no vortex thermoinsulation of the plasma can be achieved without the diaphragm.

REFERENCES

1. M. F. Zhukov, A. S. Koroteev, and B. A. Uryukov, *Applied Dynamics of Thermal Plasma* (Nauka, Novosibirsk, 1975).
2. M. F. Zhukov, I. M. Zasypkin, A. N. Timoshevskiĭ, *et al.*, in *Low Temperature Plasma*, Vol. 17: *Electric Arc Generators of Thermal Plasma*, Ed. by M. F. Zhukov and I. M. Zasypkin (Nauka, Novosibirsk, 1999).
3. B. I. Mikhaĭlov, Teplofiz. Aéromekh. **8** (1), 133 (2001).
4. A. S. An'shakov, M. F. Zhukov, A. N. Timoshevskiĭ, *et al.*, in *Proceedings of the 8th All-Union Conference on Hydrodynamics of Low-Temperature Plasma, Novosibirsk, 1980*, Part 3, p. 57.
5. V. S. Éngel'sht, V. Ts. Gurovich, G. A. Desyatkov, *et al.*, in *Low-Temperature Plasma*, Vol. 1: *Theory of Electric Arc Column*, Ed. by V. S. Éngel'sht and B. A. Uryukov (Nauka, Novosibirsk, 1990).
6. G. Biĭbosunova, V. M. Lelevkin, V. V. Liventsov, *et al.*, Preprint IAÉ-4697/6 (TsNIIatominform, Moscow, 1988).
7. S. V. Patankar, *Numerical Heat Transfer and Fluid Flow* (McGraw-Hill, New York, 1980; Énergoatomizdat, Moscow, 1984).

Translated by P. Pozdeev

Technical Physics Letters, Vol. 28, No. 9, 2002, pp. 725–728. Translated from Pis'ma v Zhurnal Tekhnicheskoĭ Fiziki, Vol. 28, No. 17, 2002, pp. 37–44.

Multilayer Co/Pd Films with Nanocrystalline and Amorphous Co Layers: Coercive Force, Random Anisotropy, and Exchange Coupling of Grains

R. S. Iskhakov, S. V. Komogortsev, A. D. Balaev, and L. A. Chekanova

Kirensky Institute of Physics, Siberian Division, Russian Academy of Sciences, Krasnoyarsk, Russia

e-mail: rauf@iph.krasn.ru

Received January 18, 2002

Abstract—The values of saturation magnetization M_s, exchange coupling constant A, local magnetic anisotropy field H_a, random anisotropy correlation radius R_c, and coercive force H_c were independently measured for multilayer Co/Pd films with nanocrystalline and amorphous Co layers. It is shown that variation of the coercive force $H_c(t_{Co})$ as a function of the cobalt layer thickness t_{Co} is related to changes in characteristics of the magnetic microstructure. The main factor determining changes in the ferromagnetic correlation radius R_f and the average anisotropy $\langle K \rangle$ of a magnetic block in multilayer Co/Pd films is variation of exchange coupling constant $A(t_{Co})$. © *2002 MAIK "Nauka/Interperiodica".*

The magnetic structure of nanocrystalline and amorphous ferromagnets is determined by their random magnetic anisotropy (RMA) and results from a competition of the ordering action of exchange interactions and the disordering effect of random local anisotropy K breaking the long-range ferromagnetic order [1]. In such materials, the ferromagnetic order is established at a characteristic length $R_f = R_c(H_{ex}/D^{1/2}H_a)^2$, where $H_a = 2K/M_s$ is the local magnetic anisotropy field, R_c is the random anisotropy correlation radius, H_{ex} is the exchange field, D is a numerical coefficient of the symmetry (equal to 1/15 in the case of a uniaxial anisotropy), and M_s is the saturation magnetization. The resulting magnetic structure can be described in terms of an ensemble of weakly coupled magnetic blocks [1, 2] with an average dimension of $2R_f$, an average block anisotropy of $\langle K \rangle = K/N^{1/2} = K(R_c/R_f)^{3/2}$, and randomly oriented unit anisotropy vectors **n**.

To the present, researchers engaged in the magnetic properties of such materials believed that this type of magnetic structure is just what accounts for the observed values of characteristics of the magnetically soft amorphous and nanocrystalline alloys [2–4]. It should be noted that an analysis of the behavior of the coercive force H_c within the framework of the RMA model used in [2–4] is directed mostly to the study of H_c as a function of the nanograin size, $H_c(R_c)$, thereby assuming that the values of anisotropy $K(R_c)$, exchange coupling $A(R_c)$, and saturation magnetization $M_s(R_c)$ are constant (or their changes can be ignored). However, now there are prerequisites for undertaking complex measurements of all the parameters entering into theoretical expressions for H_c (R_c, H_a, A, and M_s) and revealing the corresponding dependences. In particular, the RMA and magnetic block structure can be studied using small-angle neutron diffraction [5–7] and measurements of magnetization curves in the region of magnetizations close to saturation [8–10]. The exchange coupling constants are widely determined using methods based on the spin-wave resonance (SWR) [11] and Bloch's $T^{3/2}$ law [12].

The results of our preliminary investigation of the magnetization behavior $M(H)$ in multilayer Co/Pd film structures [9] showed that these films are characterized by a two-dimensional inhomogeneity of the magnetic anisotropy. In particular, it was found that the experimental curve of $M(H)$ measured in the range of field strengths from 5 to 25 kOe can be described by the expression

$$\frac{\Delta M}{M_s} = \frac{D^{1/2}\langle H_a \rangle}{H}, \qquad (1)$$

which corresponds to a ferromagnet with an anisotropy inhomogeneity dimension $d = 2$ and an experimental condition of $H < H_{ex}$. Applying expression (1) to the analysis of the experimental $M(H)$ curve, we determined the values of $\langle H_a \rangle$ and $R_f = (A/D^{1/2}\langle K \rangle)^{1/2}$ (where $\langle K \rangle = M_s\langle H_a \rangle/2$ and the coefficient D was selected equal to 1/15 [8]). It was established that the value of H_c correlates to $\langle H_a \rangle$ (Fig. 1), which implies that $\langle H_a \rangle$ plays the role of effective anisotropy in the Co/Pd films studied. Therefore, an analysis of the effective anisotropy and the related coercive force in these systems can be performed using expressions obtained within the framework of the RMA model.

1063-7850/02/2809-0725$22.00 © 2002 MAIK "Nauka/Interperiodica"

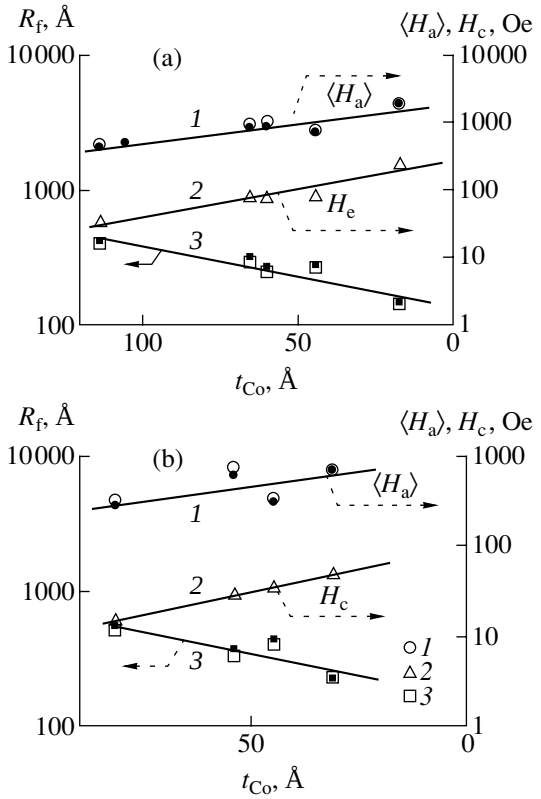

Fig. 1. Micromagnetic structure parameters (*1*) $\langle H_a \rangle$ and (*3*) R_f determined from the experimental $M(H)$ curve approximated by Eq. (1) [9] (open symbols) and calculated by formulas (2) and (3) (small black symbols) and (*2*) coercive force H_c of multilayer Co/Pd films: (a) $[Co_{90}P_{10}(t_{Co})/Pd\ (14\ Å)]_{20}$; (b) $[Co_{93}P_7(t_{Co})/Pd\ (14\ Å)]_{20}$.

However, the aforementioned method of determining $\langle H_a \rangle$ and R_f cannot disclose the relationship between the changes of these parameters and variations of the main magnetic quantities (H_a, A, M_s) and the main parameter of the magnetic nanostructure (R_c). Indeed, the theoretical expressions for $\langle H_a \rangle$ and R_f of an amorphous or nanocrystalline ferromagnet with a two-dimensional inhomogeneity of the magnetic anisotropy are as follows [9]:

$$R_f = \frac{2A}{\sqrt{D}H_a M_s R_c}, \quad (2)$$

$$\langle H_a \rangle = \frac{\sqrt{D}H_a^2 M_s R_c^2}{2A}. \quad (3)$$

According to formula (3), in a material with equiaxial grains ($2R_c = t_{Co}$, where t_{Co} is the cobalt layer thickness) and constant values of H_a, A, and M_s, the values of $\langle H_a \rangle$ and H_c must increase in proportion to t_{Co}^2. This is at variance with the experimental curves of $\langle H_a \rangle$ and H_c, which are described by decreasing functions of t_{Co} (Figs. 1a and 1b).

In this study, the saturation magnetization M_s, exchange coupling constant A, local magnetic anisotropy field H_a, random anisotropy correlation radius R_c, and coercive force H_c were independently measured for multilayer Co/Pd films with nanocrystalline and amorphous Co layers. The aim of these measurements was to determine the contribution of each of these parameters to the change of magnetic microstructure characteristics R_f and $\langle H_a \rangle$ and, hence, to the change of coercive force H_c.

The thermomagnetic curves and magnetization curves of these ferromagnetic films were measured in a wide range of temperatures (0–200 K) and magnetic fields (0–30 kOe) using an automated vibrating-sample magnetometer with a superconducting coil.

Multilayer Co/Pd films were prepared by sequential chemical deposition of components onto glass substrates. We studied two series of samples: (i) $[Co_{93}P_7(t_{Co})/Pd\ (14\ Å)]_{20}$, where t_{Co} = 6, 30, 45, 55, or 80 Å and (ii) $[Co_{90}P_{10}(t_{Co})/Pd\ (14\ Å)]_{20}$, where t_{Co} = 20, 45, 60, 65, or 115 Å. Small phosphorus additives in the cobalt layers of Co/Pd ensured the obtaining of ferromagnetic layers composed of metastable Co(P) solid solutions featuring various short-range order structures [13]. Previously [13], it was established that Co(P) layers containing 5–8 at.% P possess an fcc structure, while the layers containing above 9 at.% P occur in the amorphous state.

The experimental temperature dependence $M(T)$ of multilayer Co/Pd films measured in the temperature range from 50 to 200 K can be described by the equation

$$M(T) = M_{s0}(1 - BT^{3/2}). \quad (4)$$

The values of magnetization M_{s0} and constant A, calculated from the Bloch constant B by the formula

$$A = \frac{k_B}{8\pi}\left(\frac{g\mu_B}{M_{s0}}\right)^{1/3}\left(\frac{2.612}{B}\right)^{2/3}, \quad (5)$$

are listed in the table.

In order to determine the parameters H_a and R_c characterizing the orientational inhomogeneity of the magnetic anisotropy, it is necessary to measure the magnetization curves both in the fields smaller than the exchange field H_{ex} and in the fields significantly exceeding H_{ex}, that is, to find two experimental asymptotes $M(H)$. Indeed, in the fields $H > H_{ex}$, the magnetization approaches the saturation level according to the law

$$\frac{\Delta M}{M_s} = \left(\frac{D^{1/2}H_a}{H}\right)^2. \quad (6)$$

Measuring this asymptotic region of the $M(H)$ curve, we can determine the value of $D^{1/2}H_a$. The field strength at which the behavior according to Eq. (1)

changes to the behavior described by Eq. (6), $H_{ex} = 2A/MR_c^2$, is used to calculate the correlation radius R_c.

As was noted above, the values of H_{ex} for the multilayer Co/Pd films studied varied within 20–25 kOe, which is very close to the maximum field strengths used in our experiments. Therefore, direct determination of the H_a and R_c values from the asymptotic regimes using Eqs. (1) and (6) was impossible. However, measurements in the fields of 25–30 kOe revealed certain deviations of the experimental $M(H)$ curves from the power dependence $M(H) \sim H^{-1}$, which were related to the onset of the transition of the magnetic system to the regime described by expression (6). Based on these deviations, we determined the parameters H_a and R_c using approximation of the portions of $M(H)$ curves in the fields from 5 to 30 kOe by a theoretical expression obtained previously [14] for a two-dimensional inhomogeneity of the magnetic anisotropy. This analytical expression (the law of magnetization variation close to saturation) for $d = 2$ is as follows:

$$\frac{\Delta M(H)}{M_s} = \frac{DH_a^2}{H\left(\frac{2A}{MR_c^2} + H\right)}. \quad (7)$$

Figure 2 shows a typical experimental magnetization curve approximated by expression (7); the inset presents a plot of the square deviation s^2 of the experimental plot $M(H)$ from the theoretical curve (7) in relative units versus the fitting parameter R_c. The data refer to the $M(H)$ measurements for a $[Co_{90}P_{10}(t_{Co})/Pd\ (14\ Å)]_{20}$ sample with $t_{Co} = 115$ Å. The minimum of s^2 (in absolute units) agrees well with the experimental mean-square error of M_s. The values of H_a and R_c corresponding to the s^2 minimum for the Co/Pd films studied are presented in the table.

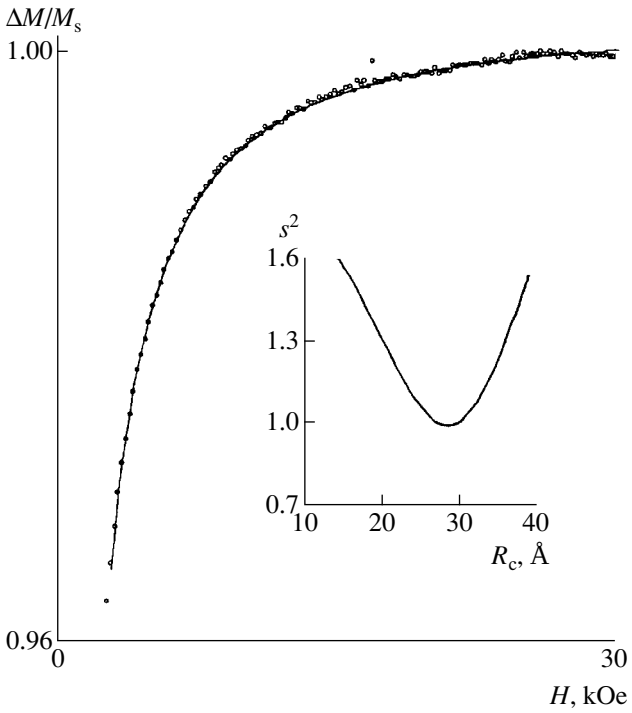

Fig. 2. Magnetization curve of the $[Co_{90}P_{10}(t_{Co})/Pd\ (14\ Å)]_{20}$ sample with $t_{Co} = 115$ Å measured in the region of approaching saturation (points) and approximation using expression (7) (solid curve). The inset shows a plot of the square deviation s^2 of the given experimental plot $M(H)$ from the theoretical curve in relative units versus the fitting parameter R_c.

Once the numerical values of H_a, A, M_s, and R_c are determined, we can calculate $\langle H_a \rangle$ and R_f using formulas (2) and (3). The results of these calculations are presented by small black symbols in Fig. 1. As can be seen, the $\langle H_a \rangle$ and R_f vales determined directly via Eq. (1) and those calculated by formulas (2) and (3) show a good coincidence. An analysis of the dependences $H_a(t_{Co})$,

The main magnetic constants and parameters of the random anisotropy, magnetic microstructure, and coercive force of Co/Pd films with amorphous and nanocrystalline Co layers

Type of samples	t_{Co}, Å	A, 10^{-6} erg/cm^3	M_s, G	H_c, Oe	R_c, Å	$D^{1/2}H_a$, kOe
Nanocrystalline Co, $[Co_{93}P_7(t_{Co})/Pd\ (14\ Å)]_{20}$	30	0.37	800	49	21	2
	45	0.63	870	34	26	1.4
	55	0.92	885	28	30	2.1
	80	0.93	914	11	26	1.5
Amorphous Co, $[Co_{90}P_{10}(t_{Co})/Pd\ (14\ Å)]_{20}$	20	0.17	483	300	18	3.3
	45	0.34	720	85	18	2.4
	60	0.51	916	76	24	2.2
	65	0.62	913	76	25	2.2
	115	0.63	888	33	26	1.6

$R_c(t_{Co})$, $A(t_{Co})$, and $M_s(t_{Co})$ presented numerically in the table shows that a maximum gradient is characteristic of the exchange coupling constant A, which varies by a factor of almost 4. This is evidence that the main factor determining changes in the characteristics $\langle H_a \rangle$ and R_f of the magnetic microstructure of multilayer Co/Pd films and, hence, of their coercive force H_c, is variation of the exchange coupling constant A (one of the main magnetic parameters) related to a decrease in the thickness of Co layers, rather than a change in the anisotropy correlation radius R_c or the grain size. We believe that a similar situation takes place in nanocrystalline ferromagnetic alloys of the finemet type, extensively developed and studied in recent years.

REFERENCES

1. Y. Imry and S.-K. Ma, Phys. Rev. Lett. **35**, 1399 (1975).
2. G. Herzer, IEEE Trans. Magn. **26**, 1397 (1990).
3. M. Muller and N. Mattern, J. Magn. Magn. Mater. **136**, 79 (1994).
4. K. Suzuki, G. Herzer, and J. M. Cadogan, J. Magn. Magn. Mater. **177-181**, 949 (1998).
5. N. Murillo and J. Gonzalez, J. Magn. Magn. Mater. **218**, 53 (2000).
6. J. J. Ryne, IEEE Trans. Magn. **MAG-21**, 1990 (1985).
7. J. F. Löffler, J. P. Meier, B. Doudin, *et al.*, Phys. Rev. B **57** (5), 2915 (1998).
8. V. A. Ignatchenko, R. S. Iskhakov, and G. V. Popov, Zh. Éksp. Teor. Fiz. **82** (5), 1518 (1982) [Sov. Phys. JETP **55**, 878 (1982)].
9. R. S. Iskhakov, S. V. Komogortsev, A. D. Balaev, and L. A. Chekanova, Pis'ma Zh. Éksp. Teor. Fiz. **72** (6), 440 (2000) [JETP Lett. **72**, 304 (2000)].
10. R. S. Iskhakov, S. V. Komogortsev, Zh. M. Moroz, and E. E. Shalygina, Pis'ma Zh. Éksp. Teor. Fiz. **72** (12), 872 (2000) [JETP Lett. **72**, 603 (2000)].
11. R. S. Iskhakov, S. V. Stolyar, L. A. Chekanova, *et al.*, Fiz. Tverd. Tela (St. Petersburg) **43**, 1072 (2001) [Phys. Solid State **43**, 1108 (2001)].
12. R. S. Iskhakov, S. V. Komogortsev, S. V. Stolyar, *et al.*, Pis'ma Zh. Éksp. Teor. Fiz. **70** (11), 727 (1999) [JETP Lett. **70**, 736 (1999)].
13. L. A. Chekanova, R. S. Iskhakov, G. I. Fish, *et al.*, Pis'ma Zh. Éksp. Teor. Fiz. **20**, 73 (1974) [JETP Lett. **20**, 31 (1974)].
14. V. A. Ignatchenko and R. S. Iskhakov, Fiz. Met. Metalloved., No. 6, 75 (1992).

Translated by P. Pozdeev

Technical Physics Letters, Vol. 28, No. 9, 2002, pp. 729–731. Translated from Pis'ma v Zhurnal Tekhnicheskoĭ Fiziki, Vol. 28, No. 17, 2002, pp. 45–50.

The Interaction of Porous Silicon with Water: A Chemographic Effect

E. A. Tutov, M. N. Pavlenko, I. V. Protasova, and V. M. Kashkarov

Voronezh State University, Voronezh, Russia

e-mail: phssd2@main.vsu.ru

Received March 27, 2002

Abstract—Based on the results of pH and chemographic measurements, it is shown for the first time that the oxidation of porous silicon in aqueous media is accompanied by the liberation of hydrogen in the ionic and atomic forms. © *2002 MAIK "Nauka/Interperiodica".*

Investigation of the interaction of porous silicon (por-Si) with water is important for several reasons. First, por-Si layers for semiconductor devices are obtained by anodizing in aqueous electrolytes [1]; subsequent washing and storage also involve exposure to water and moisture. Second, por-Si is now extensively studied as a potential material for water adsorption sensors [2–5]. The possible analysis of gases dissolved in capillary-condensed water [6] provides for a link between gas and liquid sensors (i.e., between electronic "nose" and "tongue" devices). Third, analysis of this interaction allows some physicochemical characteristics of por-Si [2, 4] and their time variation to be determined [7, 8].

The results of previous investigations of the interaction of por-Si with water, which were performed mostly by the vibrational spectroscopy techniques, can be summarized as follows. Immediately after the por-Si formation, dangling bonds present on the surface of pores are mostly passivated by hydrogen, which is gradually replaced by oxygen. The process of phase transformation of the surface of por-Si takes a long time (several months) [8], proceeds at a higher rate in aqueous media than in air [7, 9], and includes both reversible and irreversible reactions [7].

A change in the morphology and composition of surface phases during heterogeneous reactions in thermodynamically nonequilibrium systems (to which por-Si belongs) may be accompanied by the emission of active species (atoms, radicals, ions) gaining energy for the desorption at the expense of chemical reactions and/or relaxation of mechanical stresses in the surface layers of a disordered material. Such processes are widely studied with the aid of semiconductor sensors [11–13], which offer a unique sensitivity at a sufficient selectivity.

A less known method for the investigation (and imaging) of redox reactions in aqueous media is based on the so-called chemographic effect [14–16]. The process of chemography consists essentially in recording a spatial pattern of evolution of the chemically active reaction products on a photosensitive material (photographic film or paper). Similar to optical radiation, the products of redox reactions are capable of reducing silver halides [17] and produce blackening of the photosensitive material (immediately or after developing). In addition, there is a possibility of detecting oxidizing species by clarification of a fog on the photosensitive material.

Since the interaction of por-Si with water and dissolved oxygen represents an oxidation process, which may be accompanied by the liberation of hydrogen in the form of ions, atoms, and/or molecules, the measurements of chemographic activity of por-Si were supplemented by determination of the hydrogen index (pH) [18].

The experiments were performed with por-Si prepared from (100)-oriented KEF-grade single crystal silicon wafers with an electron concentration of 1.3×10^{16} cm^{-3} by standard electrochemical etching in a mixed $HF/H_2O–C_3H_8O–H_2O_2$ (2 : 2 : 1) electrolyte for 5 min at a current density of 15 mA/cm^2. The por-Si samples had a relative porosity estimated at 50–70% [2] and a specific surface area (determined by adsorption - capacitive porosimetry [4]) of about 200 m^2/cm^3. This (for a porous layer thickness of 10 μm) is 2000 times greater than the visible area of particles. These estimates agree well with the analogous published data.

Proceeding from an average number density of silicon atoms on the surface (8×10^{14} cm^{-2} [19]), and assuming (for estimation purposes) that each silicon atom on the pore wall surface has a single dangling bond passivated by hydrogen, we can calculate the upper limit of pH variation in the case when all hydrogen would pass into solution in the form of H^+ (more strictly speaking, H_3O^+) ions. For a por-Si sample with a geometric area of 1.58 cm^2 and a water (doubly distilled, pH 7.0 at 300 K) volume of 7 cm^3, the hydrogen

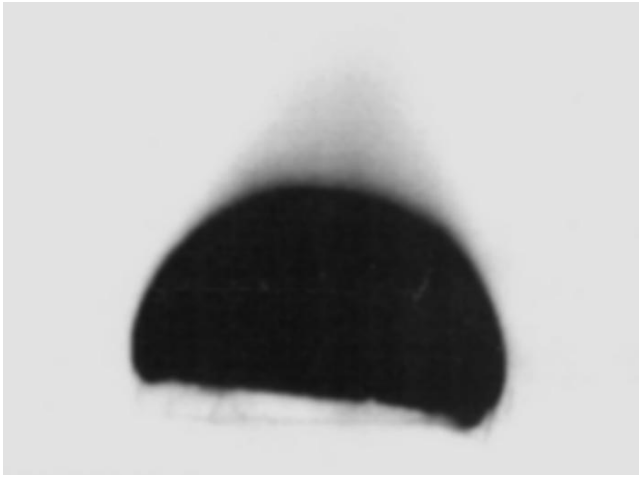

A typical chemographic image of the surface of a por-Si plate (sample diameter, 30 mm).

index of the medium upon placing the sample into water must not drop below 3.2 (acid medium).

The pH measurements were performed using a glass working electrode and a silver chloride reference electrode, with preliminary calibration in a series of standard buffer solutions. In the experiment, the pH value of doubly distilled water decreased to 5.6 within 15 min of being in contact with por-Si. The possibility of measuring pH to within a few tenths allowed us to ignore possible variations of temperature, dissolved gases, etc.

Thus, the process of por-Si oxidation in water (and aqueous solutions) is accompanied by the liberation of hydrogen chemisorbed on the pore walls. A part of hydrogen is desorbed in the form of H^+ ions, which accounts for the pH being shifted toward lower values (acid medium).

A change in pH may also take place as a result of the dissociation of water molecules during direct interaction between H_2O and Si [10], and the dissociation of silanol groups

$$\equiv\text{Si–OH} \longleftrightarrow \equiv\text{Si–O}^- + \text{H}^+,$$

the latter reaction being reversible. However, the yield of these reactions is determined by the concentration of active centers on the surface of por-Si, which eventually does not exceed the surface density of silicon atoms. Since the change in pH is affected by the initial degree of oxidation of por-Si, the discharge of H^+ ions with the formation of atomic and molecular hydrogen, the diffusion limitations of the hydrogen transport in the pores, and some other factors, we consider the results of pH measurements as being well consistent with the initial assumptions and estimates.

An increase in the concentration of positively charged hydrogen ions in water is compensated by the formation of an excess negative charge on por-Si, which can be experimentally detected by a change in the electrode potential.

These results are partly at variance with the considerations [9] concerning the oxidation of silicon by hydrogen ions (H_3O^+ or D_3O^+), since these ions are in fact the products of the reaction of por-Si oxidation.

The liberation of reducing species during the interaction of por-Si with water was studied by chemographic techniques (see the figure). A positive image was obtained on photographic paper exposed for 15 min (in contrast to [14–16], where a more sensitive film was employed); the blackening was distinguishable even before development. The chemographic image reveals the boundaries of a silicon substrate and exhibits intense homogeneous blackening of the photosensitive material against the por-S layer.

The character of the image, in particular, a diffuse shadowing in the upper part extending outside the boundaries of the por-Si sample (probably related to a flow of chemographically active particles), allows us to exclude the optical effect of chemiluminescence of por-Si from the possible factors and mechanisms of the observed phenomenon. This conclusion agrees with the results of investigation of the chemographic activity of water upon extraction of the por-Si sample [14].

This experiment was not planned to provide any quantitative information. However, it is obvious that the chemographic technique possesses a unique illustrative power and has good prospects and high potential for physicochemical research.

In contrast to pH measurements, which showed evidence of the liberation of H^+ ions during the interaction of por-Si with water, the chemographic experiment is probably indicative of the presence of atomic hydrogen in the aqueous medium. Atomic hydrogen is the most probable reducer of silver halides in the emulsion layer of photosensitive materials (this is consistent with a conclusion made in [16]). In addition, molecular hydrogen can be subjected to atomization on catalytically active silver microparticles liberated at the stage of primary reduction by atomic hydrogen. This factor, by the well-known mechanism based on the spill-over effect [13, 20], will lead to further silver reduction from AgHal. In this respect, we may speak of an autocatalytical process of chemical sensitization of the photosensitive material [17]. A large specific area of por-Si provides for a high rate of heterogeneous reactions and accounts for large magnitudes of the observed effects.

Thus, we have demonstrated for the first time that the interaction of por-Si with water is accompanied by the liberation of hydrogen in the ionic and atomic forms. Under certain conditions, the former effect (ΔpH) can be used for nondestructive evaluation of the quality of surface passivation (degree of oxidation) of por-Si. The second effect (chemography) offers the possibility of imaging the spatial (lateral) pattern of the state of the por-Si surface and the intensity of the interaction of por-Si with water.

REFERENCES

1. V. P. Bondarenko, V. E. Borisenko, L. N. Glinenko, and V. A. Raĭko, Zarubezh. Élektron. Tekh., No. 9, 55 (1989).
2. E. A. Tutov, A. Yu. Andryukov, and V. M. Kashkarov, Zh. Prikl. Khim. (St. Petersburg) **73** (7), 1071 (2000).
3. E. A. Tutov, A. Yu. Andryukov, and S. V. Ryabtsev, Pis'ma Zh. Tekh. Fiz. **26** (17), 53 (2000) [Tech. Phys. Lett. **26**, 778 (2000)].
4. E. A. Tutov, A. Yu. Andryukov, and E. N. Bormontov, Fiz. Tekh. Poluprovodn. (St. Petersburg) **35** (7), 850 (2001) [Semiconductors **35**, 816 (2001)].
5. E. A. Tutov, S. V. Ryabtsev, and A. Yu. Andryukov, Kondens. Sredy Mezhfaznye Granitsy **4** (1) (2002) (in press).
6. B. I. Podlepetskiĭ and A. B. Simakov, Zarubezh. Élektron. Tekh., No. 2, 64 (1987).
7. B. R. Dzhumaev, Fiz. Tekh. Poluprovodn. (St. Petersburg) **33** (11), 1379 (1999) [Semiconductors **33**, 1247 (1999)].
8. A. M. Orlov, A. A. Skvortsov, A. G. Klement'ev, and A. V. Sindyaev, Pis'ma Zh. Tekh. Fiz. **27** (2), 76 (2001) [Tech. Phys. Lett. **27**, 77 (2001)].
9. D. N. Goryachev, G. Polisskiĭ, and O. M. Sreseli, Fiz. Tekh. Poluprovodn. (St. Petersburg) **32** (8), 1016 (1998) [Semiconductors **32**, 910 (1998)].
10. J. Salonen, V. P. Lehto, and E. Laine, Appl. Surf. Sci. **120**, 191 (1997).
11. T. Wadayama, T. Arigane, K. Fujine, and A. Hatta, J. Lumin. **78**, 111 (1998).
12. B. M. Kostishko and Yu. S. Nagornov, Zh. Tekh. Fiz. **71** (7), 60 (2001) [Tech. Phys. **46**, 847 (2001)].
13. I. A. Myasnikov, V. Ya. Sukharev, L. Yu. Kupriyanov, and S. A. Zav'yalov, *Semiconductor Sensors in Physicochemical Studies* (Nauka, Moscow, 1991).
14. A. I. Elizarov and V. L. Tereshchenko, Kondens. Sredy Mezhfaznye Granitsy **1** (2), 129 (1999).
15. A. I. Elizarov, V. V. Bogoboyashchiĭ, A. V. Sukachev, and A. Yu. Glybin, Kondens. Sredy Mezhfaznye Granitsy **1** (3, 4), 250 (1999).
16. A. I. Elizarov, V. V. Bogoboyashchiĭ, and A. Yu. Glybin, Kondens. Sredy Mezhfaznye Granitsy **2** (4), 342 (2000).
17. *The Theory of the Photographic Process*, Ed. by T. H. James (Macmillan, New York, 1977; Khimiya, Leningrad, 1980).
18. R. G. Bates, *Determination of pH: Theory and Practice* (Wiley, New York, 1964; Khimiya, Leningrad, 1968).
19. A. H. Boonstra, Philips Res. Rep., Suppl., No. 3, 3 (1968).
20. V. V. Rozanov and O. V. Krylov, Usp. Khim. **66** (2), 117 (1997).

Translated by P. Pozdeev

Technical Physics Letters, Vol. 28, No. 9, 2002, pp. 732–734. Translated from Pis'ma v Zhurnal Tekhnicheskoĭ Fiziki, Vol. 28, No. 17, 2002, pp. 51–56.

Bound *S*-States of a Two-Electron Atom

A. A. Kiselev and S. I. Nikitin

St. Petersburg State University, St. Petersburg, Russia

e-mail: antchis@pcqnt2.phys.spbu.ru

Received January 22, 2002

Abstract—A special selection of the Euler angles is made, according to which one axis of the rotating coordinate system is related to the center of mass of electrons. The hierarchy of the hyperspherical coordinates R, α, and θ allows sequential quantization with respect to these variables to be performed. The complex structure of the potential with respect to the R coordinate leads to the use of a quasi-classical approximation. The energy spectrum of doubly excited S-states of a He atom is determined. The results are compared to other published data. © *2002 MAIK "Nauka/Interperiodica".*

Investigation of the excited states of a two-electron atom is still an important problem in atomic physics. A hyperspherical coordinate system was originally used by Fock [1]. Herrick and Kellman [2] considered a hypothetical helium atom in a doubly excited state as the analog of a linear symmetric three-atomic molecule. A classification of doubly excited states in terms of the quantum numbers K and T was originally proposed by Herrick and Sinanoglu [3].

A spherical model with electrons moving on the surface $r_1 = r_2 = \text{const}$ was considered in [4, 5]. An analytical investigation of the model problem was undertaken in [6]. A classification of doubly excited states necessary for comparison of the results of analytical calculations to the experimental data was given in [3, 7]. Data on the energies of various states were reported in [8–12].

Let us place the nucleus at the origin and let r_1 and r_2 be the distances from the nucleus to the first and second electron, respectively. Let $X'Y'Z'$ denote a rotated coordinate system obtained by sequentially rotating the system through the Euler angles α, β, and γ: first, by angle α about the Z axis, then by angle β about the new position of the Y axis and, finally, by angle γ about the final position of the Z axis. In the figure, γ is the angle between the X' and Y axes, the X' axis passing through a triangle with r_1 and r_2 sides. Let us consider X' as the median of this triangle. Then one of the Euler angles, γ, will change; the new angle, also denoted by γ, differs from the old γ value by angle δ [6]. Below we use the atomic system of units in which $\hbar = m = e = 1$.

The Hamiltonian of a two-electron atom can be written as

$$\hat{H} = -\frac{1}{2}\Delta_1 - \frac{1}{2}\Delta_2 - \frac{Z}{r_1} - \frac{Z}{r_2} + \frac{\lambda}{r_{12}}, \qquad (1)$$

where Z is the charge of the nucleus and λ is a parameter, which is close to unity. Let us separate the variables in Eq. (1) by a conventional method using the Wigner–Hirschfelder formula

$$\Psi_{LM}(r_1, r_2) = \sum_{K=0}^{L} f^{+}_{LK}(r_1, r_2) D^{L+}_{MK}(\Omega) + f^{-}_{LK}(r_1, r_2, \theta) D^{L-}_{MK}(\Omega),$$

where

$$\Omega = \{\theta, \beta, \gamma\},$$

$$D^{L+}_{MK} = (\sqrt{2} + (2-\sqrt{2})\delta_{ok})^{-1}[D^{L}_{MK} + (-1)^{K} D^{L}_{M-K}], \qquad (2)$$

$$D^{L-}_{MK} = (i\sqrt{2})^{-1}[D^{L}_{MK} - (-1)^{K} D^{L}_{M-K}].$$

L is the total orbital momentum; M and K are the projections of the total momentum onto the Z and Z' axes, respectively; note also that $\mathbf{L} = \mathbf{l}_1 + \mathbf{l}_2$ and $\mathbf{l} = \mathbf{l}_1 - \mathbf{l}_2$, where $\mathbf{l}_1$ and $\mathbf{l}_2$ are the orbital moments of electrons.

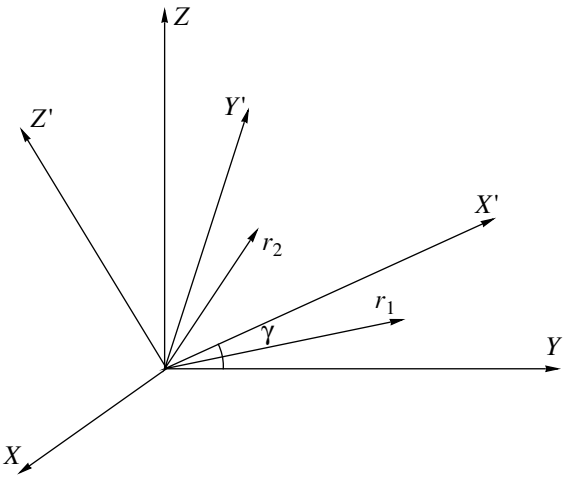

Figure.

1063-7850/02/2809-0732$22.00 © 2002 MAIK "Nauka/Interperiodica"

Finally, we arrive at the following system of equations:

$$\left[\frac{1}{r_1^2}\frac{\partial}{\partial r_1}r_1^2\frac{\partial}{\partial r_1}+\frac{1}{r_2^2}\frac{\partial}{\partial r_2}r_2^2\frac{\partial}{\partial r_2}-\frac{2\sin\theta}{Q}\left(-Kr_2\frac{\partial}{\partial r_1}+Kr_1\frac{\partial}{\partial r_2}\right)\right.$$
$$+\left(\frac{1}{r_1^2}+\frac{1}{r_2^2}\right)\left(\frac{1}{\sin\theta}\frac{\partial}{\partial\theta}\sin\theta\frac{\partial}{\partial\theta}-\frac{L(L+1)-K^2}{2\sin^2\theta}\right)$$
$$\left.-\frac{2K^2}{Q}+\frac{2Z}{r_1}+\frac{2Z}{r_2}-\frac{2\lambda}{r_{12}}+2E\right]f_{LK}^{+}+\frac{1}{2\sin^2\theta}\left(\frac{1}{r_1^2}+\frac{1}{r_2^2}\right)$$
$$\times[(1-\delta_{0K}-\delta_{1K}+(\sqrt{2}-1)\delta_{2K})\beta_{K-2}\beta_{K-1}e^{-2i\delta}f_{LK-2}^{+}$$
$$+(1+(\sqrt{2}-1)\delta_{0K})\beta_{-K-2}\beta_{-K-1}e^{2i\delta}f_{LK+2}^{+}$$
$$+L(L+1)\delta_{1K}f_{LK}^{+}]+\frac{2}{Q}\frac{r_1^2-r_2^2}{r_1r_2\sin\theta}\left[\frac{K}{2}-\frac{1}{2}(1-\delta_{0K}\right.$$
$$-\delta_{1K}-\delta_{2K})\beta_{K-2}\beta_{K-1}e^{-2i\delta}f_{LK+2}^{-}+L(L+1)\delta_{1K}f_{LK}^{-}$$
$$-(1+(\sqrt{2}-1)\delta_{0K})\beta_{-K-2}\beta_{-K-1}e^{-2i\delta}f_{LK+2}^{-} \quad (3)$$
$$\left.-\frac{2K^2}{Q}f_{LK}^{-}-\frac{K}{2}\sin2\theta\frac{\partial}{\partial\theta}f_{LK}^{-}\right]$$
$$+\frac{2}{Q}((1+(\sqrt{2}-1)\delta_{0K})\beta_{-K-2}\beta_{-K-1}e^{2i\delta}f_{LK+2}^{-})$$
$$+\frac{2}{Q}[(1-\delta_{0K}-\delta_{1K}-(\sqrt{2}-1)\delta_{2K})\beta_{K-2}\beta_{K-1}e^{-2i\delta}f_{LK-2}^{+}$$
$$+(1+(\sqrt{2}-1)\delta_{0K})\beta_{-K-2}\beta_{-K-1}e^{2i\delta}f_{LK+2}^{+}]=0.$$

$$Q=r_1^2+r_2^2+2r_1r_2\cos\theta,$$
$$r_{12}=\sqrt{r_1^2+r_2^2-2r_1r_2\cos\theta}.$$

Let us consider the *S*-state, $L = K = 0$, and pass to the new variables. These will be the hyperradius $R = \sqrt{r_1^2+r_2^2}$, hyperangle $\alpha = \arctan\frac{r_1}{r_2}$, and angle θ (remaining unchanged). Upon recalculating the derivatives $\frac{\partial}{\partial r_1}$, $\frac{\partial}{\partial r_2}$, the factor $\frac{1}{r_1^2}+\frac{1}{r_2^2}$, and the interelectron distance r_{12}, we obtain an equation in the new variables R, α, and θ:

$$\left[\frac{1}{R^5}\frac{\partial}{\partial R}R^5\frac{\partial}{\partial R}+\frac{1}{R^2}\frac{1}{\sin^2\alpha\cos^2\alpha}\frac{\partial}{\partial\alpha}\sin^2\alpha\cos^2\alpha\frac{\partial}{\partial\alpha}\right.$$
$$+\frac{1}{R^2\sin^2\alpha\cos^2\alpha}\frac{1}{\sin\theta}\frac{\partial}{\partial\theta}\sin\theta\frac{\partial}{\partial\theta}+\frac{2Z(\sin\alpha+\cos\alpha)}{R\sin\alpha\cos\alpha} \quad (4)$$
$$\left.-\frac{2\lambda}{R\sqrt{1-\sin2\alpha\cos\theta}}+2E\right]f_{00}^{+}=0.$$

The energies of a two-electron atom in the *S*-state

m	n	k	$-E_0$	Refs.
1	1	2	0.763	0.766 [8, 10, 11]
		3	0.431	
		4	0.272	
1	0	2	0.778	0.778 [8, 10, 11]
		3	0.439	
		4	0.278	
2	0	3	0.141	0.138 [9]
		4	0.119	
		5	0.102	
3	0	3	0.139	0.138 [9]
		4	0.109	
		5	0.085	
4	0	4	0.082	0.079 [12]
		5	0.055	0.051 [12]
5	0	4	0.068	0.069 [12]
		5	0.052	0.051 [12]

A hierarchy of the new coordinates is as follows: θ is the most rapid, α is less rapid, and R is the slowest variable. We are interested in solutions in the vicinity of $\theta = \pi$, $\alpha = \frac{\pi}{4}$.

The spectrum of χ is written as

$$\chi=\frac{4\sqrt{2}Z}{R}-\frac{\sqrt{2}\lambda}{R}+\frac{\sqrt{\lambda}}{2\sqrt{R^3}}(4n-2-\sqrt{3})+\frac{4}{R^2} \quad (5)$$
$$-\frac{(2m+1)\sqrt{16-6\sqrt{2}ZR+\frac{\sqrt{2}}{2}\lambda R+\frac{\sqrt{\lambda R}}{4}(4n-2-\sqrt{3})}}{R^2},$$

where $m = 0, 1, 2, \ldots$ and n is the quantum number obtained from the equation with respect to θ. Note that even and odd m correspond to the singlet and triplet states, respectively.

The classical momentum of the system under consideration is

$$p=\sqrt{2E+\chi}. \quad (6)$$

Using the Bohr–Sommerfeld quantization conditions, we obtain

$$\int_{R_1}^{R_2}dR\sqrt{\chi+2E}=\pi(2k+1),\quad k=0,1,2\ldots, \quad (7)$$

where R_1 and R_2 are the turning points. The values of the energy E_0 obtained in the case of the *S*-state are

listed in the table. As can be see from these data, most of the energy values are in good agreement with the data reported in [8–12].

REFERENCES

1. V. A. Fock, Izv. Akad. Nauk SSSR, Ser. Fiz. **18** (1), 2 (1954).
2. D. K. Herrick and M. E. Kellman, Phys. Rev. A **21** (2), 418 (1980).
3. D. H. Herrick and O. Sinanoglu, Phys. Rev. A **97** (1), 97 (1975).
4. G. Breit, Phys. Rev. **35** (6), 569 (1930).
5. G. S. Ezra and R. S. Berry, Phys. Rev. A **25** (3), 1513 (1982).
6. S. I. Nikitin and V. N. Ostrovsky, J. Phys. B **18** (22), 4349 (1985).
7. C. D. Lin, Phys. Rev. A **76** (1), 76 (1982).
8. M. K. Chen, Phys. Rev. A **56** (6), 4537 (1997).
9. Y. K. Ho, Phys. Rev. A **56** (5), 3634 (1997).
10. Y. K. Ho, Phys. Rev. A **34** (5), 4402 (1986).
11. J. E. Lindroth, Phys. Rev. A **49** (6), 4473 (1994).
12. Y. K. Ho, J. Phys. B **23** (6), L71 (1990).

Translated by P. Pozdeev

Technical Physics Letters, Vol. 28, No. 9, 2002, pp. 735–739. Translated from Pis'ma v Zhurnal Tekhnicheskoĭ Fiziki, Vol. 28, No. 17, 2002, pp. 57–66.

Structural and Electrical Characteristics of Epitaxial InP Layers on Porous Substrates and the Parameters of Related Au–Ti Schottky Barriers

I. N. Arsent'ev, M. V. Baĭdakova, A. V. Bobyl', L. S. Vavilova, S. G. Konnikov, V. P. Ulin, N. S. Boltovets, R. V. Konakova, V. V. Milenin, and D. I. Voĭtsikhovskiĭ

Ioffe Physicotechnical Institute, Russian Academy of Sciences, St. Petersburg, 194021 Russia
e-mail: bobyl@theory.ioffe.rssi.ru
"Orion" State Research Institute, Kiev, Ukraine
e-mail: bms@i.kiev.ua
Institute of Semiconductor Physics, National Academy of Sciences of Ukraine, Kiev, Ukraine
e-mail: konakova@eee.semicond.kiev.ua
Received January 14, 2002

Abstract—The structures comprising three epitaxial InP layers—buffer (n^{++}), active (n), and contact (n^{+})—were grown by liquid phase epitaxy on porous and compact (control) InP(100) substrates. High quality of the active n-InP layer obtained on a porous substrate (in comparison to the control samples) is confirmed by the values of the halfwidths of the (311) X-ray diffraction reflections (54″ versus 76″), dislocation concentration (5×10^2–5×10^3 cm^{-2} versus 5×10^4–5×10^5 cm^{-2}), and electron mobility (4000 cm^2/V s versus 3000–3500 cm^2/V s). Using these homoepitaxial InP structures, Au–Ti Schottky diodes with a working mesastructure area of ~1.8×10^{-6} cm^2 were prepared. It was found that diodes based on the porous substrates are characterized by significantly smaller leak currents and higher breakdown voltages as compared to those of the control diodes: 1 nA, 27 V versus 200 nA, 15 V. © *2002 MAIK "Nauka/Interperiodica".*

Use of thin-film homo- and heteroepitaxial structures based on $A^{III}B^{V}$ compounds in semiconductor devices of various types possess increased requirements on the structural perfection and stability of the epitaxial layers. Meeting these requirements is especially important in microwave devices such as Schottky barrier diodes, Gunn diodes, and field-effect transistors [1], which makes the development of new methods for obtaining high-quality epitaxial structures a currently important task. A promising method is offered by the use of "soft" porous substrates, which leads to a significant decrease in the level of internal mechanical stresses in the epitaxial layers [2] and to an increase in the structural perfection of various heterostructures, in particular, those based on the $A^{III}B^{V}$ semiconductor compounds [3, 4].

The main method of characterizing the quality of epitaxial layers is based on the luminescence measurements. Previously, we performed such investigations for GaN [3] and InGaAs [4] layers grown by molecular beam epitaxy (MBE) and liquid phase epitaxy (LPE) on porous GaAs substrates. However, the electrical properties of such epitaxial layers and the related metal–semiconductor junctions have remained all but unstudied. No detailed comparison was made between the properties of layers grown on the porous ("soft") and compact ("hard") substrates under otherwise equal growth conditions and subsequent technological stages (contact formation).

The aim of this work was to study the structural and electrical properties of homoepitaxial InP structures comprising three layers—buffer (n^{++}), active (n), and contact (n^{+})—which were grown by liquid phase epitaxy on porous and compact (control) InP(100) substrates. This combination of layers was selected because such systems are usually employed in Schottky barrier structures as well as in some other structures for microwave diodes and transistors [1, 5]. The homoepitaxial configuration and the LPE growth technique were chosen for the following reasons.

(i) Although extensive investigations of the heteroepitaxy of InP layers on various porous substrates [6, 7] are in progress, the task of increasing the quality of homoepitaxial layers still remains important. The presence of even insignificant lattices of microdeformations (~10^{-3}) in the working layers leads to rapid degradation and defect formation, thence to increased leak currents [1], flicker noise [8], and the concentration of nonradiative recombination centers [9]. This results in a drop in the useful yield of devices produced on the basis of these structures.

(ii) The LPE technique, despite obvious disadvantages (in particular, primary etching of the substrate

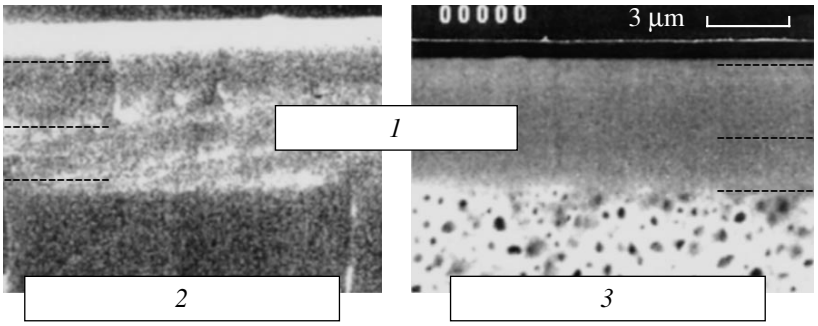

Fig. 1. SEM micrographs of the cleavages of three-layer epitaxial InP structures (*1*) grown on the (*2*) "hard" (sample 18) and (*3*) porous (sample 19) InP substrates. The SEM measurements were performed in the reflection mode at a maximum contrast. Dashed lines indicate approximate positions of the interfaces between buffer, active, and contact InP layers.

surface), still offers the least expensive and most flexible method for conducting a series of technological tests [10]. Below, the parameters of Schottky diodes obtained in our experiments will be compared to analogous characteristics of control diodes (sample 1) prepared using commercial structures grown from the gas phase on hard substrates.

Three-layer epitaxial InP films were grown by LPE on specially prepared InP(100) substrates with dimensions of 10 × 15 mm, doped with tin to $n^{+++} = 1–2 \times 10^{18}$ cm^{-3}. Porous layers (9–12 μm thick) in the substrate material were obtained by electrochemical etching in aqueous chloride and bromide solutions. Epitaxial growth was effected in InP–In solution melt at a crystallization onset temperature of 655°C. The LPE regimes were optimized with respect to the duration of substrate annealing prior to contact with the liquid phase, which was necessary to remove the products formed at the stage of pore formation. In order to suppress the primary etching of substrates and the penetration of the liquid phase into the porous volume, the initially saturated melt was overcooled by 10°C before bringing it in contact with a porous substrate [10].

For comparison, three-layer InP films were also grown on the usual "hard" single crystal substrates. The parameters of the epitaxial structures are listed in Table 1. The Schottky barriers were obtained by metallization with titanium, followed by gold deposition, and represented direct mesastructures with a working area of ~1.8×10^{-6} cm^2. The ohmic contacts were prepared using a gold–germanium eutectic.

The structure of the samples was studied by X-ray diffraction and by scanning electron microscopy (SEM) in the reflection mode. The Hall mobilities of charge carriers and the current–voltage (*I–V*) characteristics of the Schottky barrier diodes were measured immediately on the wafer. Figure 1 shows the SEM micrographs of the transverse cleavages of two samples prepared on different substrates. As can be seen, the epitaxial layer on a porous substrate exhibits a homogeneous morphology of the cleavage surface. This may be indicative of the absence (or low density) of small-angle block boundaries, which are known to give rise to mechanical stresses and generate competitive cleavage surfaces (such as those observed on the cleavages of layers grown on a "hard" substrate). Note that, as is seen on the micrographs, the melt does not penetrate into the porous InP layer under the growth conditions employed.

The structural perfection of samples was evaluated using the data of X-ray diffraction measurements. The two-crystal diffraction curves were measured in the (θ, 2θ) geometry near InP(004) and InP(311) reflections using CuK_α radiation (λ = 1.5406 Å) monochro-

Table 1. The parameters of InP layers grown on compact ("hard") and porous ("soft") n^{+++}-InP substrates

Sample no.	Structure type	Parameters									
		n^{+++}, cm^{-3}	$d_{n^{+++}}$, μm	n^{++}, cm^{-3}	$d_{n^{++}}$, μm	n, cm^{-3}	d_n, μm	n^+, cm^{-3}	d_{n^+}, μm	μ$_n$, cm^2/(V s)	N_d, cm^{-2}
18	n^{+++}-n-n^+, "hard" substrate	$(1–2) \times 10^{18}$	300		1	$(1–3) \times 10^{16}$	1.5–2	$(1–3) \times 10^{18}$	0.1–0.12	3000–3500	5×10^4–10^5
19	n^{+++}-n^{++}-n-n^{+++}, porous substrate	1×10^{18}	300	2×10^{17}	1	$(1–3) \times 10^{16}$	2–2.5		0.1–0.12	4000	5×10^2–10^3

Note: μm is the electron mobility in the *n*-InP layer; N_d is the dislocation density in the *n*-InP layer.

matized by a Ge(001) crystal. Figure 2 shows the diffraction curves of the initial porous substrate before epitaxy and of the two samples (Nos. 18 and 19, see Table 1) with epitaxial layers grown on different substrates. As can be seen, the X-ray diffraction pattern obtained in the symmetric geometry near the InP(004) reflection represents a narrow peak with a full width at half-maximum (FWHM) ~20″, situated on a broad diffuse reflection related to the radiation scattered in the porous material (Fig. 2*a*). After LPE, the (004) diffraction peaks for the samples grown on both usual (Fig. 2*b*) and porous (Fig. 2*c*) substrates exhibit broadening to FWHM ~25″ and 31″, respectively. Note that the diffuse pedestal observed for the porous substrate is more intense as compared to that for the "hard" substrate.

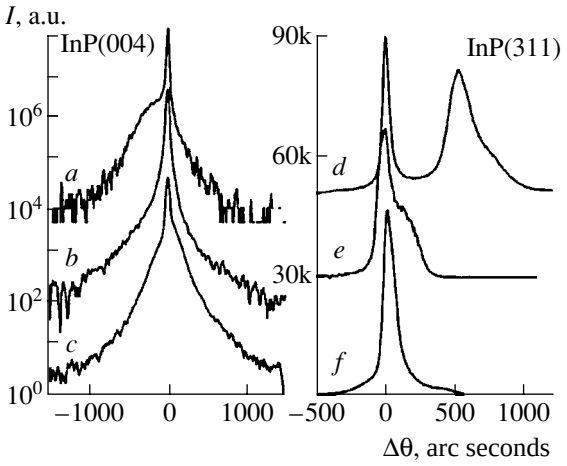

Fig. 2. X-ray diffraction patterns in the vicinity of (*a*–*c*) InP(004) and (*d*–*f*) InP(311) reflections: (*a*, *d*) the initial porous InP substrate before LPE; (*b*, *e*) sample 18 with epitaxial layers grown on a "hard" substrate; (*c*, *f*) sample 19 with epitaxial layers grown on a porous substrate.

The greater broadening effect for the samples grown on porous substrates is explained by the fact that the diffraction curves near the InP(004) reflection represent a superposition of the coherent X-ray radiation components diffracted from (i) a compact part of the InP substrate and (ii) epitaxial InP layer and (iii) of the diffuse diffraction component from the porous (disordered) part of the substrate. In order to separate the contributions from the three diffraction components, we measured the diffraction curves in the region of the InP(311) reflection (Figs. 2*d*–2*f*). As can be seen, the diffraction curve from the porous substrate (Fig. 2*d*) exhibits two peaks: one with FWHM ~54″, from a thin (<100 nm) near-surface layer of the porous InP substrate, and another with FWHM ~300″, from the volume of the layer with a developed branched porous structure. The distance between these peaks (540″) corresponds to a lattice parameter mismatch of $\Delta a/a \sim 5 \times 10^{-3}$.

Figures 2*e* and 2*f* show the X-ray diffraction patterns in the regions of the InP(311) reflection for the samples grown on the usual and porous substrates. As can be seen from Fig. 2*e*, the diffraction curve of sample 18 contains two components: from the working (active) layer and the narrow contact layer. In sample 19 grown on the porous substrate, the ratio of thicknesses of the buffer, working, and contact layers was different. For this reason, only one peak is clearly distinguished on the corresponding diffraction curve (Fig. 2*f*). In determining the peak halfwidths, we may conclude that the structural perfection of the working layer in the sample grown on the porous substrate is significantly higher as compared to that in the sample on the standard ("hard") substrate: FWHM ~54″ for sample 19 against ~76″ for sample 18. A halfwidths of the reflection component from the thin strongly doped surface layer in both cases is approximately the same (~250″). Note that the micrographs of cleavages show evidence of a structurally perfect, transition epitaxial InP layer formed on the porous substrate surface. We believe that this layer is responsible for the narrow diffraction peak in Fig. 2*d* and that the good structural parameters of this very layer account for the high quality of the subsequent working InP layer and for the unique characteristics of the Schottky diodes based on such layers.

As can be seen from the data in Table 1, the working InP layers with a thickness of 1.5–2 μm and a donor concentration of $(1–3) \times 10^{16}$ cm^{-3}, grown on porous substrates with a ~1-μm-thick buffer layer doped to $\sim 2 \times 10^{17}$ cm^{-3}, possess a more perfect structure and a higher electron mobility than the analogous working layers grown on the porous substrates without buffer.

Table 2. Electrical characteristics of the diode structures with Schottky barriers based on InP layers grown on different substrates

Sample no.	Structure type	φ_b, eV	n	I_1, nA (V = 4 V)	V_B, V
18	n^{+++}-n-n^{+}-Ti–Au "hard" substrate	0.46	1.27	200	15
1	n^{+++}-n^{++}-n-Ti–Au "hard" substrate (commercial, gas-phase growth)	0.55	1.17	20	20
19	n^{+++}-n^{++}-n-Ti–Au porous substrate	0.54	1.09	1	27

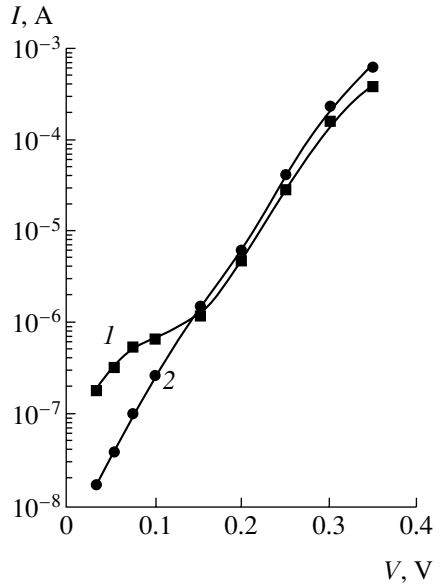

Fig. 3. Current–voltage characteristics of the diode structures with Schottky barriers based on InP layers grown on (*1*) "hard" and (*2*) porous n^{+++}-InP substrates (samples 18 and 19, respectively).

The InP layers formed on the porous substrates without buffer grow (due to the features of dysprosium doping) by the island mechanism and contain a greater number of defects.

Table 2 presents characteristics of the Schottky diodes based on the epitaxial InP structures. As can be seen from these data, the best parameters are observed for the Au–Ti–n-n^{++}-n^{+++}-InP Schottky barrier diodes based on the porous InP substrates with a buffer layer. The Schottky diodes based on the commercial structure grown from the gas phase on a "hard" n^{+++}-InP substrate (sample 1) exhibit characteristics typical of such devices [1]. At the same time, the Schottky diodes based on the n^{+++}-n^{++}-n-n^{+}-Ti–Au and n^{+++}-n-n^{+}-Ti–Au structures, with the Schottky barrier to a strongly doped n^{+}-InP layer, possess a barrier height 0.08–0.09 eV lower as compared to that of the diodes without a contact n^{+}-InP layer. This agrees with the notions about the effect of the image forces on the Schottky barrier height [11].

Figure 3 shows direct branches of the typical *I–V* curves of Schottky diodes of the Au–Ti–n-n^{++}-n^{+++}-InP type, based on porous n^{+++}-InP substrates with buffer layers (curve *2*, sample 19) and on "hard" InP substrates with buffer layers (curve *1*, sample 18). As can be seen, the direct branches of the *I–V* curves of both diodes exhibit extended portions described by the equation

$$I = I_s \exp\left(\frac{eV}{nkT} - 1\right), \qquad (1)$$

where I_s is the saturation current, n is the ideality factor, e is the electron charge, and V is the applied direct voltage. However, the initial part of the direct branch of the *I–V* curve of a diode employing the Au–Ti–n-n^{++}-n^{+++}-InP structure grown on the porous substrate does not obey Eq. (1) in the interval of voltages from 0.03 to 0.15 V. The ideality factor is 1.09 and 1.17 for curves *1* and *2*, respectively. This n value, as well as a high mobility of electrons in the active InP layers and the validity of criterion $\vartheta_D > \vartheta_R$ (where ϑ_D is the effective rate of electron diffusion from the depleted layer boundary to the point of maximum potential energy and ϑ_R is the effective rate of the surface recombination at this point), indicate that the saturation current can be described by the equation of thermoelectron emission. The Schottky barrier height determined using this equation for diodes based on the porous substrates was φ_b = 0.54 eV, while the value for the Au–Ti–n-n^{++}-n^{+++}-InP diodes based on the "hard" substrate is 0.55 eV.

The Schottky barrier diodes based on the porous substrates with buffer layers are characterized by high reproducibility of the parameters φ_b and n and by minimum values of the reverse current I_1 (on the order of 1–3 nA) in the entire range of applied voltages up to the avalanche breakdown voltage V_B. For a dopant concentration of $N_B = 3.8 \times 10^{16}$ cm^{-3}, the latter value is V_B = 27 V and agrees well with the empirical formula [12]

$$V_B = 60\left(\frac{E_g}{1.1}\right)^{1.5}\left(\frac{N_B}{10^{16}}\right)^{-0.75}, \qquad (2)$$

where E_g is the InP bandgap width.

Thus, using porous n^{+++}-InP substrates for the formation of n^{++}-n-InP epitaxial strictures, it is possible to obtain structurally perfect, active epitaxial n-InP layers possessing high electron mobilities, which can serve as a basis for the fabrication of high-quality microwave Schottky diodes.

Acknowledgments. The authors are grateful to I.S. Tarasov for fruitful discussions and interest in this study, and to P.S. Kop'ev, V.V Kuznetsov, and R.A. Suris for support and useful remarks.

This study was supported by the Russian Foundation for Basic Research, project no. 01-02-17585.

REFERENCES

1. E. F. Venger, R. V. Konakova, G. S. Korotchenkov, V. V. Mileni, É. V. Russu, and I. V. Prokopenko, *Interphase Interactions and Degradation Mechanisms in Metal–InP and Metall–GaAs Structures* (Inst. Fiz. Poluprovodn. Nats. Akad. Nauk Ukr., Kiev, 1999).
2. S. Luryi and E. Suhir, Appl. Phys. Lett. **49**, 140 (1986).
3. V. V. Mamutin, V. P. Ulin, V. V. Tret'yakov, *et al.*, Pis'ma Zh. Tekh. Fiz. **25** (1), 3 (1999) [Tech. Phys. Lett. **25**, 1 (1999)].

4. F. Yu. Soldatenko, V. P. Ulin, A. A. Yakovenko, *et al.*, Pis'ma Zh. Tekh. Fiz. **25** (21), 15 (1999) [Tech. Phys. Lett. **25**, 852 (1999)].
5. A. V. Bobyl', G. D. Varenko, S. A. Evdokimov, *et al.*, in *Reviews on Electron Technology, Series 8* (TsNII "Élektronika," Moscow, 1990), No. 1 (1572).
6. H. Fujikura, A. Liu, A. Hamamatsu, *et al.*, Jpn. J. Appl. Phys. **39**, 4616 (2000).
7. A. Liu and C. Duan, Appl. Phys. Lett. **78**, 43 (2001).
8. A. V. Bobyl, M. E. Gaevskii, S. F. Karmanenko, *et al.*, J. Appl. Phys. **82**, 1274 (1997).
9. A. V. Bobyl, R. N. Kyutt, and V. V. Tret'yakov, Semicond. Sci. Technol. **14**, 589 (1999).
10. Zh. I. Alferov, I. N. Arsent'ev, L. S. Vavilova, *et al.*, Fiz. Tekh. Poluprovodn. (Leningrad) **19** (6), 1115 (1985) [Sov. Phys. Semicond. **19**, 683 (1985)].
11. S. Sze, *Physics of Semiconductor Devices* (Wiley, New York, 1981; Mir, Moscow, 1984), Vol. 1.
12. C.-W. Kao and C. R. Crowell, Solid-State Electron. **23** (8), 881 (1980).

Translated by P. Pozdeev

Technical Physics Letters, Vol. 28, No. 9, 2002, pp. 740–742. Translated from Pis'ma v Zhurnal Tekhnicheskoĭ Fiziki, Vol. 28, No. 17, 2002, pp. 67–73.

Ultrasound-Stimulated Translation of Microparticles on the Surface of a $LiNbO_3$ Plate

A. N. Gorb and O. A. Korotchenkov

Kiev National University, Kiev, Ukraine

Received April 1, 2002

Abstract—We observed the translation of SiC microparticles on the surface of a $LiNbO_3$ waveguide plate, stimulated by ultrasound of various frequencies. It was established that probabilities of the forward and reverse translations (along and against the ultrasound propagation direction, respectively) are close for the a_1 mode of the Lamb waves, while excitation of the s_1 mode leads to preferential direct translation of the microparticles. Metallization of the surface of the $LiNbO_3$ plate leads to a significant decrease in the fraction of particles translated by the s_1 mode. The observed phenomenon is interpreted within the framework of a model taking into account the character of oscillations of particles at the $LiNbO_3$ surface excited in the a_1 and s_1 modes, as well as the existence of a variable piezoelectric field accompanying the ultrasonic action. It is suggested that the observed effect can be used for the translation of neutral and charged microparticles, including biological objects. © *2002 MAIK "Nauka/Interperiodica".*

Investigation of the transfer of substances in various states by means of ultrasonic waves is of interest from the standpoint of both basic science and applications. The dynamics of an ensemble of microparticles in the vicinity of a waveguide plate reveals the features typical of both liquids and solids. However, the features of this dynamics still remain insufficiently studied [1, 2]. Practical applications of these effects are related to a considerable extent to the possibility of driving cyclic motions of liquids (and suspended particles) in contact with a waveguide plate [3]. In particular, this technique can find applications in molecular micromechanics, transfer of microbiological objects, etc. [4].

Taking into account differences in the character of the ratio of components of elastic displacements for various wave modes in piezoelectric plates, we may expect significant features in the translation of microparticles on the surface of a $LiNbO_3$ plate upon the excitation of different modes. In addition, the propagation of ultrasonic waves in a piezoelectric $LiNbO_3$ plate is accompanied by the appearance of a variable piezoelectric field. Since this field extends outside the plate, we may expect that it will also interact with the microparticles and influence the process of their translation on the $LiNbO_3$ plate surface. The aim of this study was to elucidate the two problems indicated above.

The experiments were performed on an *YZ*-cut lithium niobate plate with a thickness of 630 μm. The ultrasonic waves were excited in the plate mounted on a grounded metal base *1* (see the inset in Fig. 1). The top face of the $LiNbO_3$ plate bears 1-mm-wide copper electrode *2*. Application of a high-frequency electric voltage *V* between electrodes *1* and *2* led to excitation of the ultrasonic Lamb waves in the plate [5]. By comparing the experimentally observed resonance modes (detected with the aid of an additional copper electrode spaced ~1 cm from electrode *2*) to the mode frequencies theoretically calculated for the plate [6], it was possible to identify the type of a series of the lowest Lamb wave modes.

Subsequent experiments were conducted using two selected frequencies, f_1 = 3.7 MHz and f_2 = 5.2 MHz, identified with a_1 and s_1 modes, respectively. The applied voltage was selected so as to provide for the equal acoustic power for the two modes. The power was evaluated using the radiation resistance [7], with allowance for the preliminarily measured electromechanical coupling coefficient for the a_1 and s_1 modes [8]. The voltage was set for the free surface of the $LiNbO_3$ plate and remained the same in the experiments with a copper metallization layer *4* (see the inset in Fig. 1), which ensured screening of the piezoelectric field. The sample objects *3* represented SiC particles with an average diameter of about 30 μm and a size scatter within 15 μm. The mass of a particle was estimated to vary between 10^{-6} and 10^{-7} g.

Upon the excitation of various waves, the particles exhibited motions on the piezoelectric plate surface, which was manifested by sequential jumps over a distance (typically) not exceeding 1–2 mm. The translations of particles were monitored with an optical microscope. Using a sequence of measurements, it was possible to follow the tracks of translations for single particles or groups of several particles during equal time intervals. Data in the plots presented below were averaged over several hundred such time intervals, which allowed us to determine the relative probability of a given translation of a microparticle as a function of

1063-7850/02/2809-0740$22.00 © 2002 MAIK "Nauka/Interperiodica"

the translation magnitude for various Lamb wave modes excited in the plate.

The results of our investigation revealed a significant dependence of the translation probability distribution for the free $LiNbO_3$ plate surface on the excited mode type (Figs. 1a and 2a). As can be seen, the microparticles are translated both in the forward direction, coinciding with that of the ultrasonic wave propagation (positive translations in Figs. 1a and 2a), and in the reverse direction (negative translations). It should be emphasized that the probabilities of translations in the opposite directions are close for the Lamb wave mode a_1 (Fig. 2a), while upon excitation of the s_1 mode, the probability of particle translation in the forward direction is significantly higher than that for the reverse direction (Fig. 1a).

The observed regularities can be analyzed taking into account the character of displacements generated on the piezoelectric plate surface upon excitation of the Lamb waves. In our case, the plate features Lamb waves with translation components U_y and U_z [6]. A quantitative analysis of the magnitudes of these components with an allowance for the piezoelectric effect is beyond the scope of this publication. Here, we restrict the consideration to a qualitative pattern, which is fully valid only for an isotropic plate.

The translation components U_y and U_z at a fixed point on the plate surface can be represented in the following form [5]: $U_y = i\alpha\exp(i\omega t)$ and $U_z = \beta\exp(i\omega t)$ for the s_1 mode, and $U_y = \gamma\exp(i\omega t)$ and $U_z = i\delta\exp(i\omega t)$ for the a_1 mode, where i is the imaginary unity, $\omega = 2\pi f$ is the circular frequency, t is the current time, and α, β, δ, and γ are certain constants. Therefore, the particles at the plate surface perform reciprocating motions so as to move along an ellipse, the motion being performed clockwise for the s_1 mode (inset in Fig. 1) and counterclockwise for the a_1 mode (inset in Fig. 2). In accordance with the surface motions in the s_1 mode of the Lamb wave, the microparticles occurring on this surface are subject to the action of forces driving these microparticles to translate predominantly in the positive direction of the Z axis, in agreement with Fig. 1a. As for the a_1 mode, we may expect a significant probability for the particles to be translated in the reverse direction as well, in agreement with Fig. 2a.

Now let us assume that the motion of particles at the $LiNbO_3$ plate surface can considered within the framework of a fluid (hydrodynamic) approach (see, e.g., [9]). In this case, the reciprocating motions considered above will be accompanied by the drift in the direction of the ultrasonic wave propagation. Approximating the microparticle velocity by the expression $v(z, t) = A\cos(\omega t - kz)$, where k is the ultrasound wavenumber and using the continuity equation $\mathrm{div}(\rho v) = -\partial\rho/\partial t$ ($\rho = \rho_0 + \tilde{\rho}$ is the density of microparticles, including the unperturbed value ρ_0 and the "ultrasonic" correction $\tilde{\rho}$), we can determine the drift velocity $v_d = \langle\tilde{\rho} v\rangle/\rho_0 = \rho_0 A^2/2\omega$ (where $\langle\ldots\rangle$ denotes averaging) in the direction of ultrasonic wave propagation. This drift explains a significant proportion of the positive translations of microparticles observed in Fig. 2a.

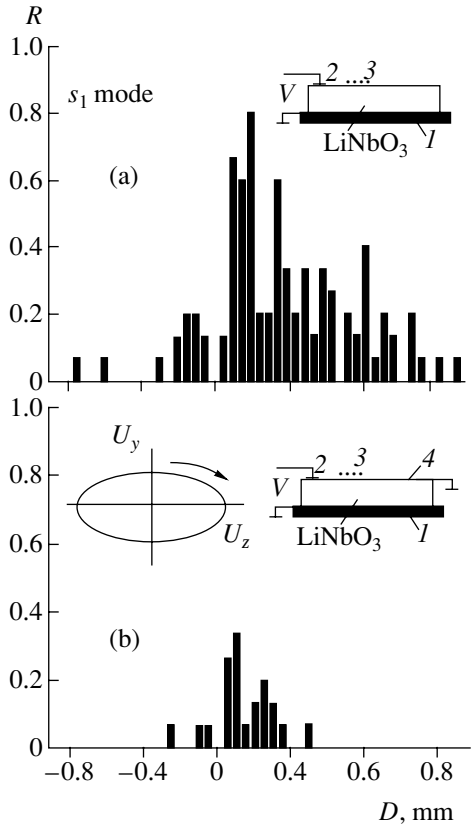

Fig. 1. Distributions of the relative probability R of translations D of SiC microparticles on the surface of (a) free and (b) metal-coated $LiNbO_3$ plate surface excited in the s_1 mode of the Lamb waves. The insets show the experimental geometry (see the text for explanations), the elliptical displacements U_y and U_z of the particles of medium (arrows indicate the direction of motion).

In order to elucidate the role of piezoelectric fields in the observed translations, let us consider the behavior of microparticles on a $LiNbO_3$ plate surface with the screened piezoelectric field (Figs. 1b and 2b). As can be seen, the number of microparticles translated by the s_1 mode has significantly decreased (Fig. 1b). To interpret this fact, note that metallization of the $LiNbO_3$ surface leads to an increase in the phase velocity of the Lamb waves [10] with a corresponding increase in the wavelength (to within 25%). This change accounts for a decrease of the translation components U_y and U_z, although the magnitude of this effect was not previously estimated. However, for the surface waves in $LiNbO_3$, metallization was reported to result in a 10–30% decrease of both components [7]. Therefore, we may suggest that a decrease (by a factor of up to 2.5) in the probability of translating particles upon moralization of the surface cannot be attributed entirely to a

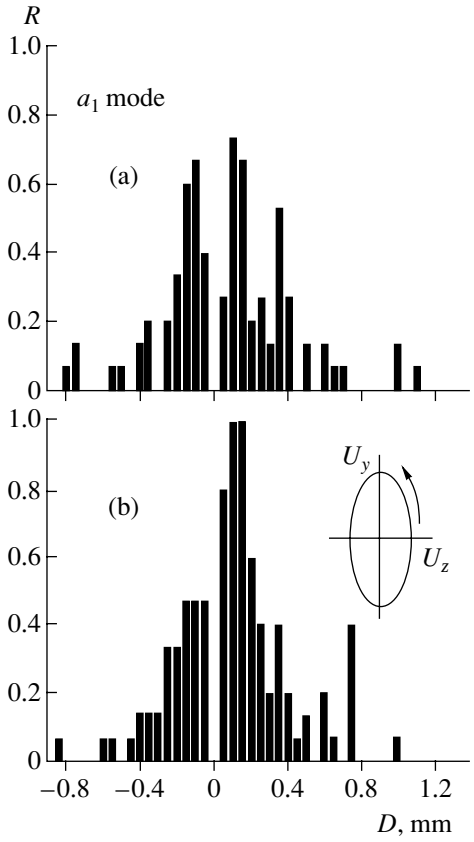

Fig. 2. Same as in Fig. 1, for the a_1 mode of the Lamb waves.

decrease in U_y and U_z. This is confirmed by data for the a_1 mode (Fig. 2b), according to which the metallization differently increases (rather than decreases) the probability of a microparticle to be translated in this mode.

We believe that this behavior can be explained taking into account a piezoelectric field accompanying the ultrasonic wave action. According to this model, microparticles are trapped at the potential minima, formed by the piezoelectric field, and translated in the direction of the ultrasonic wave propagation. This accounts for a considerable increase in the probability of positive translations in Fig. 1a as compared to that in Fig. 1b. At the same time, the probability for a microparticle to be trapped at a potential minimum moving along the *Z* axis for the a_1 mode is significantly lower than that for the s_1 mode (because of the reverse motion of particles of the $LiNbO_3$ surface, see the inset in Fig. 2). This explains the absence of a growth in the number of positive translations with simultaneous increase in the proportion of reverse translations of microparticles in Fig. 2a as compared to that in Fig. 2b. As for a physical mechanism of the proposed trapping process, we believe that this mechanism can be related to the previously described polarization interaction between microparticles and electric field [11, 12].

Thus, we observed a significant influence of the type of the Lamb wave mode excited in a $LiNbO_3$ plate on the character of translations of SiC microparticles on the waveguide surface. The translations are explained by the driving action of the vibrating waveguide surface and the piezoelectric field accompanying the wave. The results can be useful in the development of devices for translation of solid microparticles and their suspensions, including biological objects.

Acknowledgments. The authors are grateful to P.P. Il'in for fruitful discussion of properties of the Lamb waves.

REFERENCES

1. O. A. Korotchenkov and T. Goto, Phys. Rev. B **56** (21), 13646 (1997).
2. O. A. Korotchenkov and T. Goto, J. Appl. Phys. **85** (2), 1153 (1999).
3. R. M. Moroney, R. M. White, and R. T. Howe, Appl. Phys. Lett. **59** (7), 774 (1991).
4. F. Julicher, A. Ajdari, and J. Prost, Rev. Mod. Phys. **69** (4), 1269 (1997).
5. I. A. Viktorov, *Physical Principles of Application of Rayleigh and Lamb Ultrasonic Waves in Engineering* (Nauka, Moscow, 1966).
6. P. V. Burliĭ, A. N. Gorb, I. Ya. Kucherov, *et al.*, Vestn. Kiev. Univ., Ser.: Fiz.-Mat. Nauki, No. 2, 470 (2000).
7. E. Dieulesaint and D. Royer, *Elastic Waves in Solids* (Wiley, New York, 1981; Nauka, Moscow, 1982).
8. P. V. Burliĭ and A. N. Gorb, Vestn. Kiev. Univ., Ser.: Fiz.-Mat. Nauki, No. 1, 421 (2001).
9. *Physical Acoustics: Principles and Methods*, Vol. 2, Part B: *Properties of Polymers and Nonlinear Acoustics*, Ed. by W. P. Mason (Academic, New York, 1965; Mir, Moscow, 1969).
10. P. V. Burliĭ, P. P. Il'in, and I. Ya. Kucherov, Ukr. Fiz. Zh. **23** (10), 1730 (1978).
11. J. Rousselet, L. Salome, A. Ajdari, *et al.*, Nature **370**, 446 (1994).
12. L. P. Faucheux, L. S. Bourdieu, P. D. Kaplan, *et al.*, Phys. Rev. Lett. **74** (9), 1504 (1995).

Translated by P. Pozdeev

Technical Physics Letters, Vol. 28, No. 9, 2002, pp. 743–745. Translated from Pis'ma v Zhurnal Tekhnicheskoĭ Fiziki, Vol. 28, No. 17, 2002, pp. 74–81.

The Features of Photoluminescence from Nanograins of Gallium-Doped Cubic Silicon Carbide

B. M. Kostishko, Yu. S. Nagornov, Sh. R. Atazhanov, and S. N. Mikov

Ul'yanovsk State University, Ul'yanovsk, Russia

e-mail: nagornovys@ulsu.ru

Received June 1, 2002

Abstract—The photoluminescence (PL) and photoexcitation spectra of carbonized porous silicon (por-Si) doped with gallium in the course of a high-temperature annealing were studied. It is shown that carbonization leads to the formation of a heterojunction between 3C-SiC nanograins and silicon quantum wires. The spectrum of PL from gallium-doped silicon carbide nanograins is shifted by 0.35 eV toward higher energies relative to the spectrum of bulk por-Si and exhibits several features related to the radiative annihilation processes involving phonons and donor–acceptor (N–Ga) pairs. The PL excitation spectra of carbonized por-Si display two resonance bands with the energies E_1= 2.8–3.1 eV and E_2 = 3.2–3.7 eV. © *2002 MAIK "Nauka/Interperiodica".*

The light-emitting properties of porous silicon (por-Si) are related to the presence of nanodimensional silicon particles dispersed in the matrix of silicon microcrystals, amorphous silicon, and siloxen formed by electrochemical etching of the initial silicon [1, 2]. This circumstance draws the attention of an increasing number of research groups to study the luminescence properties of this unique material. Despite extensive investigation, the mechanisms of photoluminescence (PL) of por-Si are still a subject of discussion, since no unambiguous evidence in favor of a certain mechanism is available [1, 3]. In this context, one possible approach consists in modifying porous silicon so as to simplify the analysis and interpretation of experimental data. For example, the formation of a surface oxide in the course of rapid high-temperature oxidation or natural aging in air allows the material to be virtually completely purified from dissolved hydrogen known to passivate quantum wires [3]. The experiments with such hydrogen-free material are aimed at the study of the properties of heterojunctions between silicon nanograins and silicon oxide in the absence of desorption processes at the surface of quantum wires [3, 4].

The process of porous silicon carbonization under our experimental conditions was accompanied by the formation of silicon carbide nanograins of a cubic modification (3C-SiC) with a characteristic particle size on the order of 5 nm [5, 6]. This material exhibits improved light-emitting properties as compared to those of the initial por-Si. The advantages include stable PL (which does not decrease even after electron bombardment [7]) and the possibility to modify the PL spectrum by selecting a dopant introduced in the course of carbonization [5, 8]. The experiments with carbonized por-Si provide information both on the properties of 3C-SiC nanograins and on the heterojunction between these nanograins and silicon quantum wires [6, 8].

This study was aimed at determining the spectral characteristics of PL from carbonized por-Si doped with gallium in the course of high-temperature annealing.

The experiments were performed with carbonized por-Si samples prepared by the following technology. The initial por-Si was prepared from (111)-oriented *n*-Si single crystal wafers with a resistivity of 32 Ω cm by a standard electrochemical etching in a mixed HF–C_2H_5OH (1 : 1) electrolyte for 30 min at a current density of 20 mA/cm^2. Wafers with a porous layer were subjected to carbonization for 2–4 min in a reactor at 1270–1470 K in a mixture of carbon-containing (CCl_4 vapor) and carrier (hydrogen) gases. During the carbonization process, the samples were also doped with gallium atoms to a concentration of 5×10^{15} cm^{-3}. This procedure is used for the formation of 10- to 15-nm-thick buffer layers in 3C-SiC/Si heteroepitaxial structures.

The PL and photoexcitation spectra were measured at room temperature on a DFS-52 spectrometer. The PL spectra were excited by a DKSSh-150 lamp operating at a radiant power density not exceeding 70 mW/cm^2, which excluded the thermal effects on the sample surface.

As is known, the cubic modification of silicon carbide is formed when the flux of silicon atoms in the course of epitaxy exceeds the flux of carbon atoms [9]. Under our experimental conditions, the flux of Si atoms was absent and, hence, the formation of silicon carbide can take place only as a result of sublimation of Si atoms from the surface and/or diffusion of C atoms into silicon grains. Upon termination of the carbonization process, the PL spectrum of the samples exhibited no

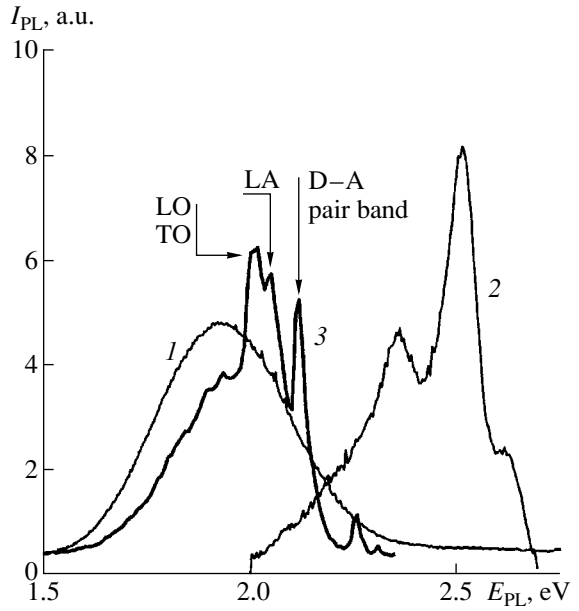

Fig. 1. The PL spectra of (*1*) initial por-Si, (*2*) por-Si carbonized for 2 min at $T = 1270$ K, and (*3*) bulk 3C-SiC (data from [9].

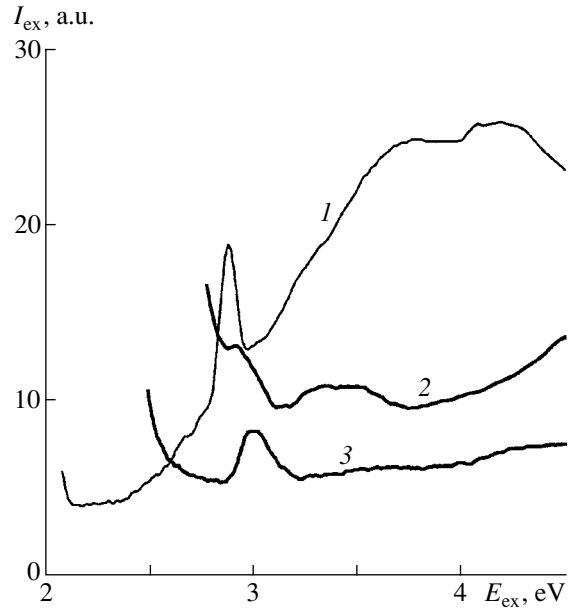

Fig. 2. The PL excitation spectra of (*1*) initial por-Si and (*2*, *3*) carbonized por-Si with detection at $E_{PL} = 2.53$ (*2*) and 2 eV (*3*).

red emission band characteristic of the PL from silicon nanograins (Fig. 1, cf. curves *1* and *2*).

The PL spectrum of carbonized por-Si doped with gallium exhibits an inhomogeneous structure with two distinct emission bands peaked at 2.34 and 2.53 eV (Fig. 1). In our opinion, the most interesting experimental finding is that the shape of this spectrum repeats that of a bulk 3C-SiC doped with aluminum [10] (Fig. 1, cf. curves *2* and *3*). The only difference is the absence of a fine structure, which is explained by the fact that our PL measurements were performed at room temperature, while the spectrum of bulk 3C-SiC:Al reported in [10] was measured at 4.2 K. In addition, there is a difference in relative intensities of the PL peaks I_{Ph} and I_{DA}, corresponding to radiative annihilation involving phonons (LO, TO, and LA phonons) and donor–acceptor (D–A) pairs, respectively. However, $I_{DA} > I_{Ph}$ both in the PL spectra of our carbonized por-Si samples and in those reported in [11].

The experimental data (Fig. 1, curves *2* and *3*) indicate that the PL spectrum of silicon carbide nanograins is shifted by 0.35 eV relative to the spectrum of bulk 3C-SiC. Since the average size of silicon nanograins in our samples was 5 nm, as estimated from the Raman scattering data [6], the shift can be attributed to the quantum confinement effects. Evidently, the scatter of the grain size must result in inhomogeneous broadening of the forbidden band in various silicon carbide nanoparticles and in the vanishing of special features of the PL spectrum. Therefore, the shift of the band precisely by 0.35 eV is also indicative that the radiative annihilation of charge carriers takes place in the interfacial layer of the heterojunction between 3C-SiC and Si nanoparticles. This assumption is also evidenced by the fact that positions of the PL peaks depend neither on the temperature nor on the duration of carbonization process in the intervals of 1270–1470 K and 2–4 min, respectively. The existence of a heterojunction in the samples of carbonized por-Si was also confirmed by the results of our previous experiments [6, 8]. Thus, irrespective of the particular dimensions of 3C-SiC and Si nanoparticles and, hence, of the forbidden band broadening, the energy gap in the heterojunction remains constant (under otherwise equal conditions).

Another interesting property of carbonized por-Si is the effective PL observed (in contrast to the bulk material) at room temperature. Analogous experimental data were reported for the samples of porous 6H-SiC, which was also (like por-Si) suggested to contain nanodimensional particles formed in the course of porous structure development [12, 13]. It was found that, on heating the samples from 80 to 300 K, the PL intensity of a bulk silicon carbide decreases by more than one order of magnitude in comparison to that of porous 6H-SiC [12], while the difference in room-temperature PL intensities may reach more than two orders of magnitude [13].

The PL excitation spectra (Fig. 2) show evidence of a different nature of the emission centers in the initial and carbonized porous silicon. According to [14, 15], the photoexcitation band with a maximum at 2.85 eV for a freshly prepared por-Si corresponds to the emission involving hydrogen complexes. In the spectrum of silicon carbide nanograins (Fig. 2, cf. curves *2* and *3*), this band is absent and the mechanism of PL excitation changes depending on the photon energy (E_{PL}) measured by the photodetector. As can be seen, the PL exci-

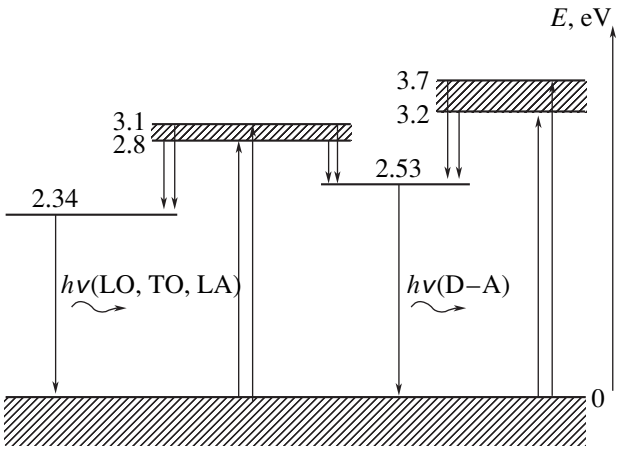

Fig. 3. Energy band diagram illustrating the mechanism of radiative annihilation of charge carriers in carbonized por-Si doped with gallium in the course of high-temperature annealing.

tation spectrum for E_{PL} = 2.53 eV exhibits two characteristic features: a band at E_1 = 2.8–3.1 eV and a broader band at E_2 = 3.2–3.7 eV. The radiative annihilation of charge carriers at 2.34 eV proceeds predominantly at the center excited in the band with a maximum in the region of 3 eV (Fig. 2).

According to the obtained experimental data, the mechanism of radiative annihilation of charge carriers in carbonized por-Si doped gallium in the course of carbonization can be described by the energy diagram depicted in Fig. 3. The excitation of carriers proceeds predominantly at energies of E_1 = 2.8–3.1 eV and E_2 = 3.2–3.7 eV. Then the excited carriers exhibit nonradiative transitions to energetically more favorable states, followed by the radiative annihilation at E_{PL1} = 2.34 eV and E_{PL2} = 2.53 eV. The PL region representing the emission events involving donor–acceptor (D–A) pairs displays two excitation energies which correspond to the excitation centers of two types. At the same time, the radiative annihilation of carriers involving phonons takes place upon excitation in a single band with a maximum at E = 3.0 eV.

Thus, we presented the results of investigation of the spectral characteristics of PL of carbonized por-Si doped with gallium in the course of high-temperature annealing. The experimental data are explained by quantum-dimensional effects and show evidence of the formation of a heterojunction between 3C-SiC nanograins and silicon quantum wires. The radiative annihilation in silicon carbide grains at E_{PL1} = 2.34 eV involves phonons, while that at E_{PL2} = 2.53 eV involves the donor–acceptor (N–Ga) pairs. The PL Excitation spectra of carbonized por-Si display two resonance bands with energies of E_1= 2.8–3.1 eV and E_2 = 3.2–3.7 eV, which participate in the excitation of charge carries at the heterojunction between 3C-SiC nanograins and silicon quantum wires.

REFERENCES

1. A. G. Cullis, L. T. Canham, and P. D. J. Calcott, J. Appl. Phys. **82** (3), 909 (1997).
2. H. D. Fuchs, M. Stutzmann, M. S. Brandt, *et al.*, Phys. Rev. B **48** (11), 8172 (1993).
3. Y. Kanemitsu, T. Ogawa, K. Shiraishi, and K. Takeda, Phys. Rev. B **48** (7), 4883 (1993).
4. D. G. Qin, H. Z. Song, B. R. Zhang, *et al.*, Phys. Rev. B **54** (4), 2548 (1996).
5. B. M. Kostishko, Sh. R. Atazhanov, S. N. Mikov, *et al.*, Phys. Low-Dimens. Struct., Nos. 7/8, 155 (1999).
6. B. M. Kostishko, Sh. R. Atazhanov, P. V. Shibaev, and Yu. S. Nagornov, Phys. Low-Dimens. Struct., Nos. 7/8, 47 (2000).
7. B. M. Kostishko, S. N. Mikov, Yu. S. Nagornov, and Sh. R. Atazhanov, Izv. Vyssh. Uchebn. Zaved., Élektron., No. 6, 5 (1999).
8. B. M. Kostishko, Sh. R. Atazhanov, I. P. Puzov, *et al.*, Phys. Low-Dimens. Struct., No. 11/12, 1 (1999).
9. A. A. Lebedev, Fiz. Tekh. Poluprovodn. (St. Petersburg) **33** (2), 129 (1999) [Semiconductors **33**, 107 (1999)].
10. J. A. Freitas, Jr., S. G. Bishop, J. A. Edmond, *et al.*, J. Appl. Phys. **61** (5), 2011 (1987).
11. W. J. Choyke and L. Patrick, Phys. Rev. B **2** (12), 4959 (1970).
12. V. F. Agekyan, Yu. A. Stepanov, A. A. Lebedev, *et al.*, Fiz. Tekh. Poluprovodn. (St. Petersburg) **31** (2), 251 (1997) [Semiconductors **31**, 202 (1997)].
13. T. Matsumoto, J. Takahashi, T. Tamaki, *et al.*, Appl. Phys. Lett. **64** (2), 226 (1994).
14. B. R. Dzhumaev, Fiz. Tekh. Poluprovodn. (St. Petersburg) **33** (11), 1379 (1999) [Semiconductors **33**, 1247 (1999)].
15. N. E. Korsunskaya, T. V. Torchinskaya, B. R. Dzhumaev, *et al.*, Fiz. Tekh. Poluprovodn. (St. Petersburg) **31** (8), 908 (1997) [Semiconductors **31**, 773 (1997)].

Translated by P. Pozdeev

Technical Physics Letters, Vol. 28, No. 9, 2002, pp. 746–749. Translated from Pis'ma v Zhurnal Tekhnicheskoĭ Fiziki, Vol. 28, No. 17, 2002, pp. 82–89.

The Avalanche Ionization Rate and Energy Exchange Mechanisms in Argon Plasma behind the Shock Wave Front

B. V. Postnikov and V. I. Yakovlev

Institute of Theoretical and Applied Mechanics, Siberian Division, Russian Academy of Sciences, Novosibirsk, Russia

e-mail: yakovlvi@itam.nsc.ru

Received February 19, 2002

Abstract—The ionization rate of argon in a relaxation zone behind the shock wave front was measured in stable flow regimes with Mach numbers above 11. Based on an analysis of the electron energy balance equation, it is suggested that high (as compared to the results of calculations) values of the avalanche ionization rate are related to the existence of an additional channel of the energy transfer during the associative ionization of argon atoms. © *2002 MAIK "Nauka/Interperiodica".*

Previously [1], we directly compared the results of measurements and calculations of the avalanche ionization rate behind the shock-wave front in monoatomic gases (argon, krypton) and revealed a significant discrepancy, whereby the experimental values were more than twofold greater than theoretical predictions. This parameter significantly depends on electron temperature T_e, and hence, the rate of ionization in the avalanche region is determined by the kinetics of the electron gas heating, in which a decisive part belongs to the electron–ion energy exchange [2–5].

The values of T_e were calculated, based on the results of measurements of the densities of electrons (n_e) and atoms (n_a), using the electron energy balance equation within the framework of a commonly accepted model of the electron heating kinetics behind the shock-wave front in monoatomic gases. The ionization rate S_e was calculated by the formula $S_e = \beta n_e n_a[1 - n_e^2/n_a K(T_e)]$, where $\beta(T_e)$ and $K(T_e)$ are the ionization rate constant and the equilibrium ionization coefficient, respectively, which depend on the electron temperature T_e and the structure of atomic energy terms. The second term in this formula takes into account the recombination process. Investigations of the ionization kinetics of argon (and other inert gases) widely employ the approximation of instantaneous ionization (single-level atom model), according to which $\beta(T_e) = C_e(2 + \Delta E/T_e)T_e^{3/2}\exp(-\Delta E/T_e)$, where ΔE is the difference between the ionization energy (E_i) and the energy of the first excited atomic level (E_1, counted from the continuum), and C_e is a constant related to the electron impact excitation cross section of the given atom. The range of variation of this quantity is $(4.7–7.0) \times 10^{-18}$ cm^2/eV (see, e.g., [2, 4]). The calculation of β taking into account a multilevel structure of terms (using the modified diffusion approximation [6]) showed that, in the region of parameters studied (electron density, $n_e \sim 10^{16}$ cm^{-3}; electron temperature, $T_e \sim 1$ eV; degree of ionization, $\sim 10^{-2}$), the effective constant is 1.3 times higher, reaching $C_e \approx 9 \times 10^{-18}$ cm^2/eV. However, even limiting values of this parameter do not eliminate the aforementioned discrepancy between measured and calculated ionization rates. Nor can the discrepancy be removed by taking into account the other factors [1], including uncertainty of the Coulomb logarithm and the influence of boundary layers. The role of radiation is also rather insignificant under the experimental conditions studied.

Thus, taking into account the dominating role of the electron–atom ionization mechanism, the high (compared to theoretical) values of the ionization rate indicate that the electron temperature is higher than that calculated using the commonly accepted model of the electron gas heating kinetics in the region of avalanche ionization. It should be noted that similar conclusions were made by some other researchers [7–10]. In particular, Tumakaev [7] introduced a concept and gave the definition for the energy deficit, which measured a mismatch in the energy balance of electrons behind the shock-wave front in monoatomic gases. This mismatch was observed both in argon and in mercury vapor (reaching up to 200%). As a result, it was concluded [7] that an additional mechanism is required, responsible for the energy transfer from heated atoms to electrons. It was also pointed out [5, 7] that the initial stage of relaxation may feature a mechanism of the associative ionization of excited atoms in collisions with unexcited particles. In this case, a liberated electron receives an energy equal to the average kinetic energy of atoms

1063-7850/02/2809-0746$22.00

($1.5kT_a$). In the reverse process of dissociative recombination, the electron is bound, losing an energy of $1.5kT_e$.

The aim of this study is to formulate an equation of the electron energy balance in the region of avalanche ionization with allowance for the aforementioned additional mechanisms of energy exchange and a multilevel atomic structure. Another purpose is to refine, based on the results of experiments with argon, the model of electron heating kinetics behind the shock-wave front in inert gases.

In the experiments [1], the results of measurements of the electron density variation $n_e(t)$ are used to determine the parameters of flow behind the shock wave front, including the degree of ionization α, the density of medium ρ or atoms n_a, the combined temperature parameter $T_0 = T_n + \alpha T_e$, and the ionization rate (electron source) S_e. The temperatures of electrons and atoms are determined using an additional energy balance equation. Taking into account the condition of quasi-stationary process, the temperature parameter is determined by the local energy balance $1.5kT_eS_e = Q_{el} - Q_{in}$ [5], where Q_{el} is the rate of heating via elastic collisions with atoms and ions (indicated below by subscript "a") and/or ions (subscript "i") and Q_{in} is the rate of electron energy loss via inelastic collisions. For a weakly ionized plasma, $Q_{el} = (T_a - T_e)(An_e^2 \ln\Lambda + Bn_en_a\sigma_a(T_e)T_e^2)/T_e^{3/2}$, where A and B are constants depending on the gas type, $\ln\Lambda$ is the Coulomb logarithm, and $\sigma_a(T_e)$ is the cross section of elastic electron–atom collisions. In the avalanche region, the rate of electron energy loss is $Q_{in} = E_iS_e$. In this model, involving a single (electron impact) ionization mechanism, the structure of energy levels is not taken into account because the flux of electrons j_e^k to continuum in any kth energy cross section (with energy E_k) is constant ($\Delta j_e^k = 0$) and equal to the ionization rate S_e.

However, in the presence of other ionization (recombination) mechanisms involving excited atoms, additional electron fluxes may appear, for example, induced by the associative ionization and dissociative recombination processes (j_{ai}^k and j_{dr}^k, respectively) for each kth level. This leads to a redistribution of fluxes j_e^k (produced by the electron impact) with the condition $\Delta j_e^k = j_{ai}^k - j_{dr}^k \neq 0$ (in contrast to the above condition $\Delta j_e^k = 0$). As a result, the energy fluxes between atoms and electrons will be redistributed as well. The new electron energy balance equation can be written as follows:

$$1.5kT_eS_e = Q_{el} - \sum j_e^k \Delta E_k + 1.5kT_a\sum j_{ai}^k - 1.5kT_e\sum j_{dr}^k, \quad (1)$$

where ΔE_k is the energy difference between adjacent $(k-1)$th and kth levels and the sum is taken over all levels. Expressing j_e^k through the electron flux j_e^l from the ground level and using the condition $\Delta j_e^k = j_{ai}^k - j_{dr}^k$ and the relation $\sum \Delta E_k = E_i$, we obtain

$$1.5kT_eS_e = Q_{el} - E_ij_e^l + \sum (1.5kT_e + E_k)j_{ai}^k - \sum (1.5kT_e + E_k)j_{dr}^k. \quad (2)$$

Since inert gases obey with a high accuracy the relation $j_e^l = S_e$, the ionization rate is determined by the above expression $S_e = \beta n_e n_a[1 - n_e^2/n_aK(T_e)]$ with the known coefficient $\beta(T_e)$. This is explained by a relatively high density of electrons and by features of the structure of atomic energy terms (proximity of the excited levels to continuum), whereby it is not important which processes account for the electron transfer from excited levels to continuum. The so-called bottleneck, determining the electron flux to continuum and, accordingly, the ionization rate, corresponds to the transition from the ground level to the first excited level and, hence the approximation of instantaneous ionization (by electron impact) is still valid. In order to confirm this, we have estimated relative changes in S_e (or j_e^l in the modified diffusion approximation) and in the populations of some excited states ($d4$, $6s$) of argon for which the data on the associative recombination rate are available [6]. The results showed that, under the experimental conditions studied, the relative change in β related to the additional fluxes is insignificant (below 1%) and the relative change in the level populations does not exceed a few percent.

Using relation (2) in combination with the energy integral $T_0 = T_a + \alpha T_e$, we obtain an equation for calculating the electron temperature:

$$T_0 - (1+\alpha)T_e = [(1.5T_e + E_i)S_e - E_S]T_e^{3/2}/(An_e^2\ln\Lambda + Bn_en_\alpha\sigma_a(T_e)T_e^2 + CT_e^{3/2}S_a). \quad (3)$$

In view of a strong (exponential) dependence $\beta(T_e)$, this parameter is determined with an accuracy sufficient for the subsequent analysis (on the order of T_e/E_i relative to the accuracy of parameters determined in experiment). The value of $E_S = \Sigma(1.5T_e + E_k)(j_{ai}^k - j_{dr}^k)$ determines the additional rate of electron energy gain and loss due to the associative ionization and dissociative recombination processes, relative to the main loss rate $(1.5T_e + E_k)S_e$ due to the electron impact mechanism. The sum is taken over all excited states involved in these reactions. Here, $j_{ai}^k = \beta_a^k n_1 n_k$, $j_{dr}^k = \beta_r^k n_m n_e$, n_1 and n_k are the densities of atoms in the ground and excited states, n_m is the density of molecular ions, and β_a^k and β_r^k are the coef-

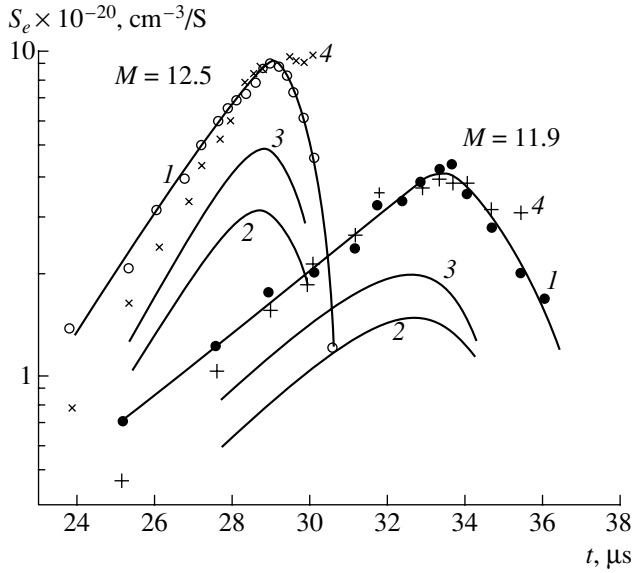

The argon ionization rate behind the shock wave front: (*1*) experiment; (*2–4*) calculations without (*2, 3*) and with (*4*) an allowance for the associative ionization mechanism.

ficients of associative ionization and dissociative recombination for the *k*th level, respectively. The denominator in Eq. (3) contains, in addition to the terms reflecting the elastic collisions of electrons with ions and atoms, a term for the associative ionization $CT_e^{3/2} S_a$, where $S_a = \beta_a^k n_1 n_k$ and C is a constant.

Exact values of E_S (as well as S_a) cannot be calculated because of restricted data on the coefficients β_a^k and β_r^k, populations on the atomic energy levels involved in the reactions under consideration, and densities of molecular ions. However, we can estimate this parameter using a method proposed [11] for the evaluation of β_a^k, according to which $\beta_a^k \approx \pi R^2 V \exp(-W_k/kT_e)$, where R is the effective radius of collision, $V = (8kT_a/\pi m)^{1/2}$ is the atomic velocity, $W_k = E_k - D$ (D is the energy of dissociation of a molecular ion), and $W_k = 0$ for $E_k < D$. Ignoring the recombination process and assuming that the energy levels are distributed in quasi-equilibrium with the electron temperature, $n_k \sim n_e^2 g_k T_e^{-3/2} \exp(E_k/kT_e)$, we arrive at an expression

$$E_S = cn_1 n_e^2 \sum (1.5T_e + E_k)\pi R^2 V \times \exp(-W_k/kT_e) g_k T_e^{-3/2} \exp(E_k/kT_e), \quad (4)$$

where c is a constant and g_k is a statistical weight of the *k*th level. Taking into account the relation $E_S \sim n_1 n_e^2$, it would be expedient to use the integral temperature parameter $P_S = E_S/n_1 n_e^2$. In the region of T_e = 11000–12000 K, this parameter can be estimated (taking into account that $T_a \approx T_e$, since their difference is below 1000 K) as $P_S \approx (41–48) \times 10^{-26}$ cm^6 s^{-1} K.

This integral parameter can be also determined on the basis of experimental results. Using the data for n_e (with allowance for $n_1 \approx n_a$) and the electron temperature T_e determined for the initial avalanche stage (before reaching the S_e maximum) from the measured ionization rate $S_e = \beta n_e n_a [1 - n_e^2/n_a K(T_e)]$, we obtain from Eq. (3) that $P_S = (130 \pm 30) \times 10^{-26}$ cm^6 s^{-1} K, which is about three times the above estimate. Taking into account the large uncertainty of this parameter, the subsequent analysis was performed with the experimental value. In the final stage of analysis, we compared the experimental and calculated (under various conditions) distributions of the ionization rate S_e behind the shock-wave front in argon at P_1 = 3 Torr and M = 12.5 and 11.9. The experimental data are presented by points *1* in the figure. The results of S_e calculations without additional energy exchange ($P_S = 0$) are presented by curves *2* and *3*, indicating the range of uncertainty in the coefficient $\beta(T_e)$: curve *2* corresponds to a smaller ($C_e = 4.7 \times 10^{-18}$ cm^2/eV [4]), and curve *3*, to greater ($C_e = 9.0 \times 10^{-18}$ cm^2/eV), value of this coefficient.

Introduction of the integral parameter accounting for the additional heating rate in the electron energy balance equation (4) eliminates the discrepancy. The results of calculations (with the maximum C_e value) of the ionization rate taking into account the associative ionization of atoms (as the source of additional energy) are depicted by crosses *4* in the figure. In the region where the ionization process predominates (in the vicinity of maximum S_e), the calculated and measured values are close because the average integral parameter takes into account these experimental data as well. In the recombination region (past the S_e maximum), where the process of dissociative recombination was ignored, the calculated S_e values vary only slightly.

Thus, we have demonstrated that the atom–atom collisions with the associative ionization of excited atoms may play a significant role in the kinetics of electron gas heating in the region of avalanche ionization of monoatomic gases behind the shock-wave front. A redistribution of the electron fluxes from bound states to continuum leads to a decrease in the energy spent for the electron impact ionization. An additional energy flux to electrons is provided by the associative ionization of highly excited atoms the temperature of which is above the electron temperature. As a result, the electron temperature increases as compared to the value determined by the electron–ion energy exchange. Despite a relatively small change in the temperature (below 1000 K, or 10%), this effect is manifested by an increase in the rate of electron–atom (avalanche) ion-

ization, which significantly depends on the electron temperature.

Acknowledgments. The authors are grateful to G.K. Tumakaev for fruitful discussions and useful remarks.

This study was supported by the Russian Foundation for Basic Research, project no. 00-01-00829.

REFERENCES

1. P. V. Grigor'ev, Yu. P. Makarov, and V. I. Yakovlev, Pis'ma Zh. Tekh. Fiz. **26** (17), 105 (2000) [Tech. Phys. Lett. **26**, 803 (2000)].
2. H. Petschek and S. Byron, Ann. Phys. **1** (3), 270 (1957).
3. P. E. Oettinger and D. Bershader, AIAA J. **5** (9), 1625 (1967).
4. I. I. Glass and W. S. Liu, J. Fluid Mech. **84** (1), 55 (1978).
5. L. M. Biberman, A. Kh. Mnatsakanyan, and I. T. Yakubov, Usp. Fiz. Nauk **102** (2), 431 (1970) [Sov. Phys. Usp. **13**, 728 (1970)].
6. L. M. Biberman, V. S. Vorob'ev, and I. T. Yakubov, *Kinetics of Nonequilibrium Low-Temperature Plasmas* (Nauka, Moscow, 1982; Consultants Bureau, New York, 1987).
7. G. K. Tumakaev, Candidate's Dissertation in Physics and Mathematics (Leningrad, 1971).
8. R. I. Soloukhin, Yu. A. Yacobi, and V. I. Yakovlev, Arch. Mech. **26**, 637 (1974).
9. K.-P. Shneider and C. Park, Phys. Fluids **18** (8), 969 (1975).
10. C. O. Weiss and B. Kotzan, Appl. Phys. **7** (3), 203 (1975).
11. *Physicochemical Processes in Gas Dynamics*, Ed. by G. G. Chernyĭ and S. A. Losev (Mosk. Gos. Univ., Moscow, 1995), Vol. 1.

Translated by P. Pozdeev

Technical Physics Letters, Vol. 28, No. 9, 2002, pp. 750–751. Translated from Pis'ma v Zhurnal Tekhnicheskoĭ Fiziki, Vol. 28, No. 17, 2002, pp. 90–94.

On the Mechanism of Collective Action of a Flux of Solid Particles upon an Obstacle

É. É. Lin, V. Yu. Mel'tsas, A. L. Stadnik, and Yu. V. Yanilkin

Institute of Experimental Physics, Russian Federal Nuclear Center, Sarov, Russia

e-mail: root@gdd.vniief.ru

Received March 25, 2002

Abstract—The results of two- and three-dimensional numerical calculations are presented for a steel ball penetrating (i) into a continuous aluminum plate and (ii) into a plate with a longitudinal channel modeling the state of a material resulting from interference of the unloading waves. The data confirm efficiency of the interference mechanism of the action of a flux of solid particles upon an obstacle. *© 2002 MAIK "Nauka/Interperiodica".*

Introduction. Investigation of the single and collective action of relatively light (~1 g) low-velocity (~1–2 km/s) solid particles impinging on an obstacle is of interest for modeling the collisions of space vehicles with fluxes of technogenic wastes and for elucidating "macroscopic" mechanisms of the penetration of small ($\leq 10^{-4}$ m) solid particles into solid targets (see, e.g., [1–8]).

Based on an analysis of inequalities relating the initial velocity and size of the particles to the critical strain rate above which a material exhibits shear hardening and brittleness, it was suggested [1] that penetrability of the target material may increase for particles of sufficiently large dimensions. A mechanism responsible for a decrease in the drag for a body moving in a medium with counterpressure was considered in [2]. The appearance of longitudinal channels, in which the continuity of a material is violated as a result of interference (or focusing) of the unloading waves (originating from the side faces of a particle and from the rear part of the neighboring particles), was described in [4, 5]. Tensile stresses arising due to the interference of the unloading waves lead to resonance excitation of a local fracture wave [5] related to the material defectness on a mesoscopic level.

An automodel character of solution [5] obtained for a solitary fracture wave gives grounds for an attempt at expanding these notions to the case of relatively large particles (bodies) with dimensions above 1 mm penetrating into solid targets. In contrast to the case considered in [6], the impact velocity must be lower than that necessary for breakdown of the obstacle by a single projectile. Only provided that this "velocity condition" is obeyed, we can reveal a collective character of the interaction of solid particles with an obstacle.

To a first approximation, the effect of interference of the unloading waves on the state of loaded material can be studied by calculations using a model whereby an effective hollow channel (hole) is set on the impact axis with a cross section significantly smaller than the midsection of the penetrant body. Then, a specific momentum transferred to the material will be approximately the same as that in a continuous obstacle. In this approximation, the role of the hollow channel reduces to modeling a discontinuity of the loaded material. A comparative analysis of the results of calculations for the impact on a continuous obstacle and a target with the model channel can reveal the influence of discontinuity on the material's penetrability.

It was experimentally established [9] that a steel ball with a diameter of 6.35 mm impinging at a velocity below 500 m/s onto a 4.84-mm-thick aluminum plate does not "feel" the presence of a hole with a diameter below one-third of the ball's diameter. This effect is due to the surface (rather than the volume) character of the energy absorption during the obstacle penetration under these conditions. In order to reveal the other possible mechanisms of penetration, it is necessary to increase the impact velocity and use a ball with a diameter smaller than the plate obstacle thickness.

Formulation and solution of the problem. We studied the case when a steel ball with a radius of r = 2.5 mm strikes at a right angle a 15-mm-thick aluminum plate, either continuous or with a longitudinal channel on the axis of impact. The impact velocity was selected equal to U = 1300 m/s. This value was estimated by a two-dimensional (2D) numerical calculation of the acceleration of steel balls in a vacuum explosion shock tube [8]. The collision was modeled by numerical methods developed previously [10, 11]. These methods, based on the finite-difference representation of a continuous medium described in terms of the Wilkins model [12], were originally intended for modeling flows with large deformations of the contact boundaries. The calculations were performed using the approximation of an ideal elastic-plastic medium described by the equation of state in the Mie–Grüneisen form.

We studied the effect of a transverse channel size L on the character of deformation of the obstacle in the

1063-7850/02/2809-0750$22.00

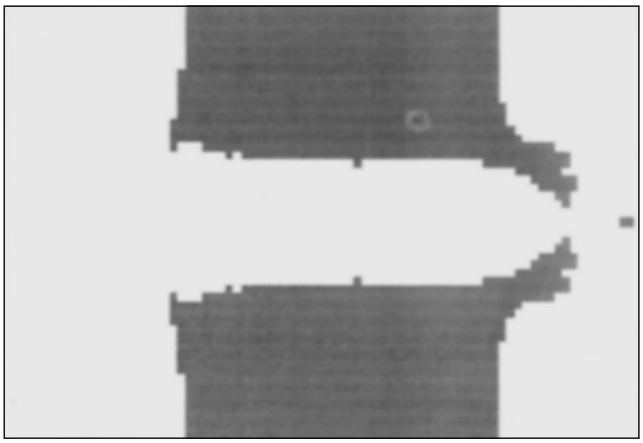

Fig. 1. A 2D pattern of the ball perforating a plate with a hollow channel (slit) width $L = 0.75$ mm; $t = 32$ μs.

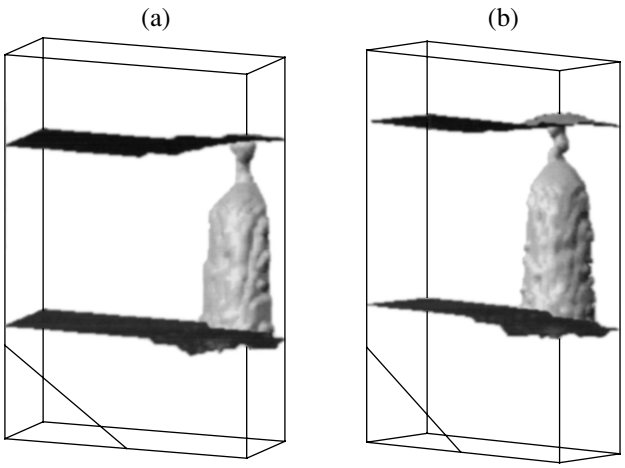

Fig. 2. A 3D pattern of the ball penetrating into a plate with a hollow channel transverse size of $L = 0.75$ mm; $t = 32$ (a) and 80 μs (b).

2D (slit) and 3D (channel) cases. The calculation was conducted on a uniform lattice with a minimum cell size of $h = 0.375$ mm. The obstacle parameters were as follows: density, $\rho_0 = 2.7$ d/cm^3; effective sound velocity, $c = 5.5$ km/s; exponent in the Mie–Grüneisen equation of state, $n = 3.2$; and Grüneisen coefficient, $\gamma = 1.666$. The material strength was characterized by the yield stress $Y = 0.25$ GPa and the Poisson coefficient $\mu = 0.33$. The ball was described by the following parameters: $\rho_0 = 7.8$ d/cm^3; $c = 4.6$ km/s; $n = 4$; $\gamma = 1.666$; $Y = 2.45$ GPa; and $\mu = 0.33$. The calculations were performed for a transverse channel size of $L = 0$ (continuous obstacle), 0.375 mm (one lattice cell), or 0.75 mm (two lattice cells).

Results. The results of calculations for a continuous plate showed that the ball is stopped at a time instant of 32 μs upon impact, at a depth of 12 mm. This calculated range corresponds to a generalized relation [7] between the ratio of the penetration depth to the projectile diameter and the impact velocity for the Fe–Al couple and $U = 1300$ m/s. The agreement confirms validity of the process model used in this study.

In the presence of a hollow channel, the results of our calculations are indicative of a deeper penetration of the ball, which practically passes through the plate. For example, a 2D calculation for $L = 0.75$ mm shows that the plate is perforated by a time instant of $t = 32$ μs (Fig. 1). In a 3D case of $L = 0.75$ mm, the states at $t = 32$ and 80 μs also correspond to an almost perforated plate (Fig. 2). A characteristic feature of the flow in the deformed medium is the material being extruded into the channel by the moving ball. The extruded material meets no drag, which accounts for a deeper penetration of the ball in this case.

Thus, we have established that, provided the impact velocity is sufficiently large, a ball with a diameter smaller than the plate thickness "feels" the presence of a hollow channel with a small cross section. This is evidence in favor of the interference mechanisms [4, 5] of the action of a flux of solid particles upon an obstacle.

Acknowledgments. The authors are grateful to A.L. Mikhaĭlov, S.A. Novikov, G.V. Belov, and V.A. Ogorodnikov for valuable remarks and support.

REFERENCES

1. S. S. Grigoryan, Dokl. Akad. Nauk SSSR **292** (6), 1319 (1987) [Sov. Phys. Dokl. **32**, 124 (1987)].
2. S. M. Bakhrakh, V. F. Spiridonov, and Yu. G. Fedorova, Pis'ma Zh. Tekh. Fiz. **17** (1), 8 (1991) [Sov. Tech. Phys. Lett. **17**, 2 (1991)].
3. S. K. Andilevko, S. M. Usherenko, and V. A. Shilkin, Pis'ma Zh. Tekh. Fiz. **24** (17), 81 (1998) [Tech. Phys. Lett. **24**, 700 (1998)].
4. S. N. Buravova, Pis'ma Zh. Tekh. Fiz. **15** (17), 63 (1989) [Sov. Tech. Phys. Lett. **15**, 689 (1989)].
5. O. Naimark, F. Collombet, and J.-L. Lataillade, J. Phys. IV **7**, 773 (1997).
6. I. E. Khorev, S. A. Zelepugin, A. A. Konyaev, *et al.*, Dokl. Akad. Nauk **369** (4), 481 (1999) [Dokl. Phys. **44**, 818 (1999)].
7. J. A. Zukas *et al.*, *Impact Dynamics* (Wiley, New York, 1982; Mir, Moscow, 1985).
8. É. É. Lin, V. Yu. Mel'tsas, S. A. Novikov, *et al.*, Khim. Fiz. **17** (1), 97 (1998).
9. S. T. Mileĭko, S. F. Kondakov, and E. G. Golofest, Probl. Prochn., No. 12, 69 (1979).
10. T. A. Toropova and Yu. V. Yanilkin, Vopr. At. Nauki Tekh., Ser.: Mat. Model. Fiz. Protsessov, No. 4, 58 (1994).
11. A. L. Stadnik, V. I. Tarasov, and Yu. V. Yanilkin, Vopr. At. Nauki Tekh., Ser.: Mat. Model. Fiz. Protsessov, No. 3, 52 (1995).
12. M. L. Wilkins, in *Fundamental Methods in Hydrodynamics*, Ed. by B. Alder, S. Fernbach, *et al.* (New York, 1964; Mir, Moscow, 1967).

Translated by P. Pozdeev

Technical Physics Letters, Vol. 28, No. 9, 2002, pp. 752–756. Translated from Pis'ma v Zhurnal Tekhnicheskoĭ Fiziki, Vol. 28, No. 18, 2002, pp. 1–12.

Variation of the Reflection Coefficient of Semiconductors in a Wavelength Range from 0.2 to 20 μm under the Action of Ultrasonic Waves

B. N. Zaveryukhin, N. N. Zaveryukhina, and O. M. Tursunkulov

Physical Engineering Institute, "Solar Physics" Research and Production Corporation, Academy of Sciences of the Republic of Uzbekistan, Tashkent, Uzbekistan

e-mail: oybtm@physic.uzsci.net

Received March 15, 2002

Abstract—The effect of ultrasonic waves on the spectral coefficient of radiation reflection from the surface of semiconductors used in solar energy converters is considered. A change in the reflectance of semiconductors before and after ultrasonic treatment is determined. It is shown that acoustic stimulation of the semiconductor surface and subsurface layers determines the radiation reflection conditions. © *2002 MAIK "Nauka/Interperiodica".*

Previously [1–3] we experimentally demonstrated for the first time that ultrasonic waves in the megahertz range may change the transport properties and the structure of semiconductors. The results of investigations devoted to the effect of ultrasound on the volume and surface properties of classical semiconductors (Si) and piezosemiconductors (GaAs), including the transport of nonequilibrium charge carriers, were summarized in [4]. Our subsequent studies, as well as the investigations of other researchers, confirmed the proposed concept of acoustically stimulated phenomena in semiconductors, according to which structural changes in semiconductors are related to the diffusion of impurity atoms, decay and formation of complexes, accumulation of impurities, etc., in ultrasonic fields. Further elucidation of the detailed mechanisms of interaction between elastic oscillations and other processes in semiconductors requires investigations in various directions.

One such direction for research is related to the effects of ultrasonic waves on the optical properties of semiconductors. These effects are important since semiconductors are widely employed in photoelectronics and solar power technology, where the optical properties of semiconducting materials determine the main performance characteristics of devices. This investigation is devoted to variation of the optical reflection coefficient R of a semiconductor surface under the action of ultrasonic waves.

We have experimentally studied the effect of ultrasound on the spectral coefficients of reflection $R(\lambda)$ of samples of silicon and gallium arsenide employed in solar energy converters. The experiments were performed at $T = 293$ K with ultrasonic waves in the frequency range $f = 0.8$–25 MHz at a power density varied within $P = 0$–15 W/cm^2. Waveguides from the ultrasound generator to semiconductor samples represented liquids, viscous media, and solids. The reflectance spectra of the surfaces of samples before and after ultrasonic treatment (UST) for a certain time were measured in a broad wavelength range including ultraviolet (UV), visible (VIS), and infrared (IR) spectral regions.

Silicon. The experiments were performed on silicon plates for solar cells with an area of $S = 2 \times 2$ cm^2 and a thickness of $d = 250$–300 μm. The base p-Si layers possessed a resistivity ρ from 1.8 to 3 Ω cm. An n^+-Si layer with a thickness of 0.5–15 μm was created by diffusion doping with phosphorus. The dopant concentrations were different in the three series of silicon samples studied: $N_1 = 1.75 \times 10^{20}$ cm^{-3}; $N_2 = 4.5 \times 10^{19}$ cm^{-3}; and $N_3 = 7.8 \times 10^{18}$ cm^{-3}. The samples carried neither electric contacts nor antireflection coatings. The ultrasonic wave was incident onto the surface of the n^+-Si layer. The coefficients $R(\lambda)$ were measured before and after UST of the samples.

Upon UST, the n^+-Si layers of certain thickness were removed step by step from the sample surface by chemical etching. At each step, the dopant concentration was determined by four-point-probe resistance measurements and then the $R(\lambda)$ spectrum was measured, after which the procedure was repeated. The reflectance measurements in the IR spectral range were performed on an IKS-14 spectrophotometer; in the UV–VIS range, the measurements were performed with SF-4 and SF-20 instruments.

1. IR reflectance of silicon: low-power UST ($P_m \leq 1$ W/cm^2). Figure 1 shows the $R(\lambda)$ spectra of silicon samples before (curves *1*, *3*, and *5*) and after (curves *2*, *4*, and *6*) UST at a frequency of $f = 15$ MHz and a power

of $P = P_m \le 1$ W/cm^2. Here, by low-power (subthreshold) UST we imply treatment at an ultrasonic wave power introducing no changes in the semiconductor defect structure (point defects, formation and decay of complexes, etc.). As can be seen from Fig. 1, all the initial $R(\lambda)$ spectra measured for the samples with various dopant concentrations N exhibit minima. The shapes of the curves are explained by dependence of the absorption index (k) and polarizability (α) of the semiconductor on the radiation wavelength λ [5, 6] (Fig. 1, curves *1*, *3*, and *5*).

The reflectance spectra measured after UST for a time of $t > 1$ h clearly reveal a shift of the $R(\lambda)$ minima toward longer wavelengths and a general decrease in the reflectance of each sample (Fig. 1, curves *2*, *4*, and *6*). We believe that the shift of $R(\lambda)$ is unambiguous evidence of the acoustically stimulated diffusion [3, 4, 7, 8] of impurity (phosphorus) inward the *p*-Si base layer, which results in a decrease of the dopant concentration N in a subsurface layer of the semiconductor.

In order to confirm this statement, we performed layer-by-layer etching of the silicon samples. The dopant concentration N and the reflectance $R(\lambda)$ were measured after the removal of each layer with a thickness of $d = 0.1$ μm. It was found that all silicon samples after UST exhibited a decrease in N at the surface and an increase in the dopant concentration in depth of the *p*-Si base layer. For example, Figs. 2a and 2b show the $N(d)$ and $R(d)$ depth profiles obtained in the course of sequential removal of layers down to a depth of $d_1 = 0.5$ μm, $d_2 = 1.5$ μm, and $d_3 = 2.5$ μm. As noted above, features of the $R(\lambda, N)$ functions were considered in detail elsewhere [5, 6].

2. UV–VIS–IR reflectance of silicon: UST at threshold powers (1.0 W < P_L < 5.0 W/cm^2). As was demonstrated above, the reflectance of silicon $R(\lambda)$ in the IR spectral range can be changed by UST at a low power of $P_m \le 1.0$ W/cm^2 for a relatively long time $t >$ 60 min. UST at a threshold (medium) power in an interval of 1.0 W < P_L < 5.0 W/cm^2 leads to the production of various defects in the bulk and subsurface layers of the semiconductor, an acoustically stimulated diffusion of impurities [3, 7–11], and the emergence of some defects at the semiconductor surface [12]. It should be noted that changes in the $R(\lambda)$ curves measured in the IR range upon UST at $P = P_L$ were generally analogous to those observed after the treatment at low powers of $P = P_m$. However, UST at threshold powers leads to the appearance of additional maxima and minima in the $R(\lambda)$ curves (Fig. 3a). These $R(\lambda)$ features in the IR range are probably related to the production of defects of the type described in [12] in the subsurface region at $P = P_L$ (Fig. 3a). Such defects can be decorated by diffusing impurity atoms, which leads to the formation of impurity "atmospheres" influencing the shape of the $R(\lambda)$ curve.

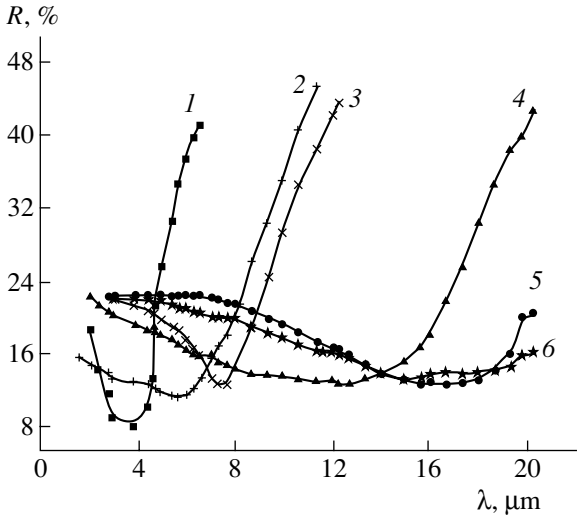

Fig. 1. Spectral dependences of the reflection coefficient R of silicon measured (*1–3*) before and (*4–6*) after UST ($P_m \le$ 1 W/cm^2; $f = 15$ MHz; $t > 60$ min) for three samples with different degrees of doping of the n^+-Si layer: (*1*, *4*) sample 1, $N_1 = 1.75 \times 10^{20}$ cm^{-3}; (*2*, *5*) sample 2, $N_2 = 4.5 \times 10^{19}$ cm^{-3}; (*3*, *6*) sample 3, $N_3 = 7.8 \times 10^{18}$ cm^{-3}.

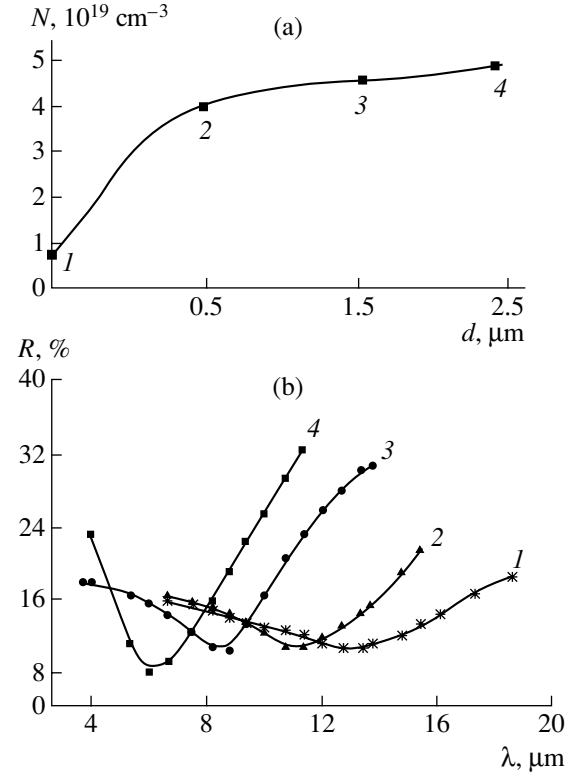

Fig. 2. The results of depth profiling of silicon (sample 4) after UST ($P_m \le 1$ W/cm^2; $f = 15$ MHz; $t = 8$ h): (a) phosphorus concentration N profile in an n^+-Si layer etched to a depth of $d = 0$ (*1*), 0.5 (*2*), 1.5 (*3*), and 2.5 μm; (b) variation of the reflection coefficient spectrum in the course of profiling; curves *1–4* correspond to points *1–4* of the dopant depth–concentration profile, where $N \approx 8.8 \times 10^{18}$ (*1*), 3.2×10^{19} (*2*), 4.3×10^{19} (*3*), and 4.8×10^{19} cm^{-3}.

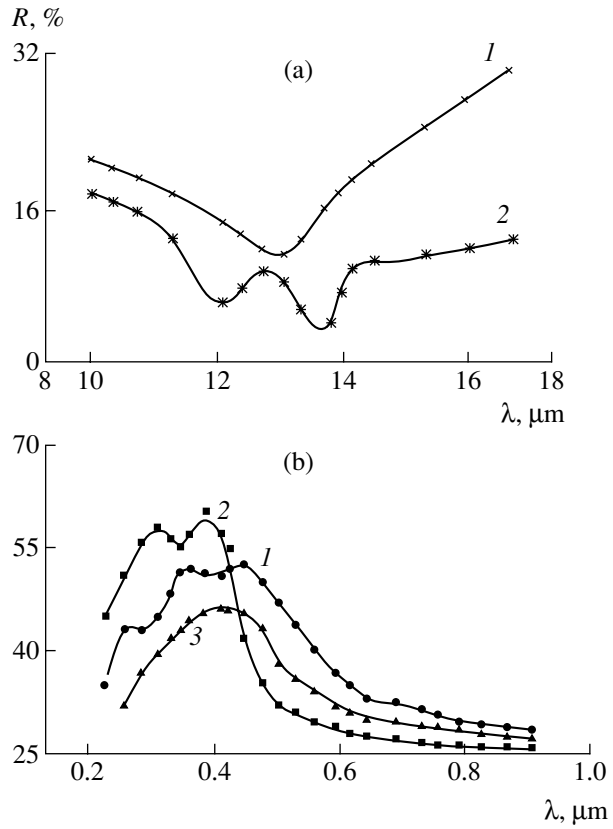

Fig. 3. Spectral dependences of the reflection coefficient R of silicon: (a) sample 03 with the initial dopant concentration in the n^+-Si layer $N = 2 \times 10^{19}$ cm^{-3}, measured (*1*) before and (*2*) after UST at $P = 5$ W/cm^2, $f = 15$ MHz, $t = 30$ min; (b) sample 05 ($N \approx 8 \times 10^{18}$ cm^{-3}) measured (*1*) before and (*2, 3*) after UST at $P_c \geq 15$ W/cm^2, $f = 15$ MHz, $t = 15$ (*2*) and 30 min (*3*).

Investigation of the behavior of $R(\lambda)$ in the UV–VIS range showed that UST at $P = P_L$ for $t < 30$ min does not lead to significant changes in shape of the $R(\lambda)$ curves due to variation of the dopant concentration or the appearance of new defects in the subsurface region of the semiconductor, because optical reflectance in this spectral range is determined predominantly by the interband transitions of charge carriers [13, 14].

The results of experiments devoted to the study of changes in $R(\lambda)$ upon UST at $P = P_m$ or $P = P_L$ did not depend on the type of waveguide material (liquids, viscous media, solids).

3. UV–VIS–IR reflectance of silicon: UST at critical powers ($P = P_c > 5$ W/cm^2). UST at a power $P = P_c$ in this range leads to the production of various structural defects in the bulk and subsurface layers of the semiconductor and to the acoustically stimulated diffusion of impurities, these phenomena taking place irrespective of the waveguide material.[1]

In the experiments with viscous and solid waveguides, we did not observe any significant changes in $R(\lambda)$ in the UV–VIS spectral range for $P = P_c$ (similar to the case of $P = P_L$ considered above): the shapes of the curves measured before and after UST were generally similar (Fig. 3b, curve *1*). Physical mechanisms responsible for this behavior of $R(\lambda)$ are considered in [13, 14].

However, the pattern dramatically changed in the experiments with liquid waveguides: for $t < 30$ min, the $R(\lambda)$ significantly increased in the wavelength region of $0.2\ \mu\text{m} < \lambda < 0.42\ \mu\text{m}$ and sharply dropped at $\lambda > 0.42\ \mu\text{m}$ (Fig. 3b, curve *2*). A comparison of the $R(\lambda)$ curves measured after UST for $t = 30$ min to that observed for $t = 15$ min (Fig. 3b, curves *3* and *2*, respectively) reveals a decrease in the region of $0.2\ \mu\text{m} < \lambda < 0.45\ \mu\text{m}$ and an increase at $\lambda > 0.45\ \mu\text{m}$. It was of interest to determine the reasons of these effects observed for the liquid waveguide. An analysis of the experimental conditions and results showed that the liquid medium exhibited cavitation [15], which resulted in the formation of depressions of various shapes on the surface of silicon. The parameters of these depressions (shape, depth) varied depending on the UST regime (power and time). As a result, the semiconductor surface acquired a kind of roughness (or texture), which is known to determine the reflectance of a semiconductor. Previously [10], we reported on the destruction of oxides on a semiconductor surface under the action of ultrasonic waves.[2]

The UST effects upon the silicon reflectance observed in different spectral intervals can be explained taking into account the presence of cavitation-induced depressions, their mean dimensions (L_m), and their surface density (N_s).

(a) $0.2\ \mu\text{m} < \lambda < 0.45\ \mu\text{m}$; $t < 15$ min. As soon as the cavitation leads to the formation of depressions on the sample surfaces with a mean size of $L_m \approx 0.15$–$0.45\ \mu\text{m}$ (comparable to the UV radiation wavelength $\lambda = 0.2$–$0.4\ \mu\text{m}$), the reflection coefficient $R(\lambda)$ in this spectral region increases (Fig. 3b, curve *2*). This is explained by increased absorption of radiation with $\lambda = 0.2$–$0.4\ \mu\text{m}$ on these surface defects; as is known, an increase in the absorption leads to a corresponding increase in reflectance [14].

(b) $0.2\ \mu\text{m} < \lambda < 0.75\ \mu\text{m}$; $t > 15$ min. As the duration of UST grows, the number of depressions on the semiconductor surface increases and their dimensions exceed the radiation wavelength: $L_m \approx 1.5$–$2.5\ \mu\text{m} > \lambda$. The sample surface in the cavitation zone becomes rougher and the reflection coefficient $R(\lambda)$ for $0.2\ \mu\text{m} < \lambda < 0.45\ \mu\text{m}$ decreases in comparison to the preceding case (Fig. 3b, curve *3*). A comparison of curves *2* and *3* in Fig. 3 shows that additional 15-min treatment (to a

[1] Identification of defects produced by UST at $P = P_L$ and P_c falls outside the framework of this study.

[2] Presenting detailed description of the behavior of $R(\lambda)$ depending on the depth, size, and density of depressions on the sample surface is beyond the scope of this paper.

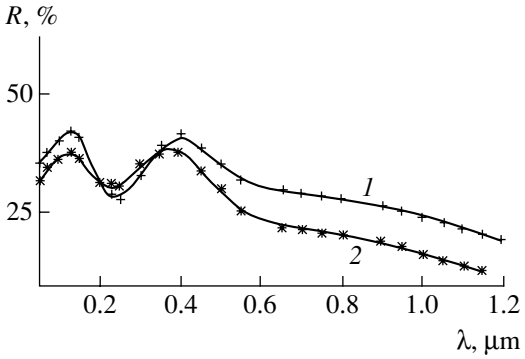

Fig. 4. Spectral dependences of the reflection coefficient R of gallium arsenide (sample 3) measured (*1*) before and (*2*) after UST.

total of $t = 30$ min) leads to an increase in $R(\lambda)$ in the range of $\lambda > 0.45$ μm.

Further increase in the UST duration t leads to the growth of $R(\lambda)$ in the entire region 0.2 μm < λ < 0.75 μm as a result of increasing cavitation damage of the semiconductor surface. Destruction of the surface is accompanied by increasing absorption and, hence, reflection of radiation in the UV–VIS range [14].

We believe that the above features in the UST-induced changes of $R(\lambda)$ in the UV–VIS and IR ranges are related not only to the cavitation erosion of the semiconductor surface. Since the behavior of $R(\lambda)$ in the UV range is determined by the energy band structure of semiconductors [13, 14], it can be suggested that a prolonged exposure to high-power ultrasound ($P = P_c$) not only generates the aforementioned surface defects, but produces irreversible deformation of the crystal as well. The effects of straining on semiconductors are considered in detail in [16].

The conclusion about semiconductor crystals being strained by ultrasound at $P = P_c$ is confirmed by the results of mechanical tests determining the effect of cavitation of the strength of metals [17]. It was found that cavitation significantly changed the mechanical properties of samples as a result of modification of the metal structure. Similar cavitation effects leading to changes in the crystal structure probably take place in semiconductors and determine the behavior of $R(\lambda)$ in the UV spectral range.

Gallium arsenide. The experiments with this semiconductor were performed using model solar cell elements representing GaAs single crystal photodetectors prepared as described in [18]. The samples were made of semi-insulating GaAs crystals ($\rho \approx 10^7$–10^8 Ω cm) with a thickness of 100–500 μm and a working area S of up to 3 cm^2. The GaAs samples treated with ultrasound exhibited changes in $R(\lambda)$ analogous to those observed for silicon. It should be emphasized that behavior of the $R(\lambda)$ spectra in both GaAs and Si samples is determined by the same mechanisms (Fig. 4).

Conclusions. Based on the above results, we can draw the following conclusions:

(i) Irradiation of a semiconductor with low-power ($P = P_m$) ultrasonic waves in the megahertz frequency range leads to a decrease in the reflection coefficient $R(\lambda)$ in the IR spectral range. This drop is caused by a decrease in the concentration N of a doping impurity in the subsurface layer of the semiconductor as a result of acoustically stimulated diffusion of the dopant inward the sample bulk.

(ii) UST at a medium (threshold) power $P = P_L$ leads to the appearance of additional maxima and minima in the $R(\lambda)$ curves in the IR range, which is related to the production of defects of various types in the bulk and subsurface layers of a semiconductor. The trapping of diffusing impurity atoms on these defects leads to the formation of impurity "atmospheres" contributing to the changes in $R(\lambda)$ in the IR range.

(iii) The acoustically stimulated effects observed in $R(\lambda)$ of semiconductors upon UST at $P = P_m$ and $P = P_L$ are independent of the type of a waveguide material.

(iv) UST in a liquid waveguide at a critical power of $P = P_c$ is accompanied by cavitation in the liquid medium, which leads to straining of the semiconductor bulk and degradation of the surface. These effects account for changes in $R(\lambda)$ in the spectral region of 0.2 μm < λ < 1.0 μm. The degree of variation of the $R(\lambda)$ spectrum depends on the ultrasonic wave power, frequency, and duration of action.

In concluding, it should be noted that the question as to which types of defects influencing the optical properties are formed in semiconductors under the action of ultrasound requires additional investigations.

Acknowledgments. The authors are grateful to V.V. Volodarskiĭ (Obninsk) for kindly providing the samples and for his help in measurements.

REFERENCES

1. B. N. Zaveryukhin, V. D. Krevchik, R. A. Muminov, *et al.*, in *Proceedings of the XXXIII Conference on Nuclear Spectroscopy and Structure of Atomic Nucleus, 1983*, p. 530.
2. A. G. Gaibov, B. N. Zaveryukhin, V. D. Krevchik, *et al.*, in *Proceedings of the XXXIII Conference on Nuclear Spectroscopy and Structure of Atomic Nucleus, 1983*, p. 531.
3. A. G. Gaibov, B. N. Zaveryukhin, V. D. Krevchik, *et al.*, Pis'ma Zh. Tekh. Fiz. **10** (10), 616 (1984) [Sov. Tech. Phys. Lett. **10**, 260 (1984)].
4. B. N. Zaveryukhin, Candidate's Dissertation (Kiev, 1990).
5. L. E. Howards and I. J. Gilbert, J. Appl. Phys. **134** (1), 236 (1963).
6. M. B. Kagan, M. M. Koltun, and A. P. Landsman, Zh. Prikl. Spektrosk. **5** (6), 770 (1966).
7. B. N. Zaveryukhin, V. D. Krevchik, R. A. Muminov, and A. Sh. Shamagdiev, Fiz. Tekh. Poluprovodn. (Lenin-

grad) **20** (3), 525 (1986) [Sov. Phys. Semicond. **20**, 330 (1986)].

8. B. N. Zaveryukhin, Kh. Kh. Ismailov, R. A. Muminov, and Sh. V. Égamov, in *Proceedings of the VI All-Union Conference on Physicochemical Principles of Semiconductor Doping, Moscow, 1988* (Nauka, Moscow, 1988), p. 133.
9. A. P. Zdebskiĭ, V. L. Korchnaya, T. V. Torchinskaya, and M. K. Sheĭnkman, Pis'ma Zh. Tekh. Fiz. **12** (1), 76 (1986) [Sov. Tech. Phys. Lett. **12**, 31 (1986)].
10. B. N. Zaveryukhin, Kh. Kh. Ismailov, R. A. Muminov, and O. Tursunkulov, Pis'ma Zh. Tekh. Fiz. **22** (15), 25 (1996) [Tech. Phys. Lett. **22**, 609 (1996)].
11. V. D. Krevchik, R. A. Muminov, and A. Ya. Yafasov, Phys. Status Solidi A **63**, K159 (1981).
12. I. V. Ostrovskiĭ, L. P. Steblenko, and A. B. Nadtochiĭ, Fiz. Tekh. Poluprovodn. (St. Petersburg) **34** (3), 257 (2000) [Semiconductors **34**, 251 (2000)].
13. T. S. Moss, *Optical Properties of Semi-Conductors* (Butterworths, London, 1959; Inostrannaya Literatura, Moscow, 1961).
14. P. S. Kireev, *Physics of Semiconductors* (Vysshaya Shkola, Moscow, 1975).
15. *Ultrasound. Small Encyclopedia*, Ed. by I. P. Golyamina (Sov. Éntsiklopediya, Moscow, 1979).
16. A. L. Polyakova, *Deformation of Semiconductors and Semiconductors Devices* (Énergiya, Moscow, 1979).
17. K. K. Shal'nev, R. D. Stepanov, and I. L. Logov, Dokl. Akad. Nauk SSSR **169** (1), 85 (1966) [Sov. Phys. Dokl. **11**, 616 (1967)].
18. S. A. Azimov, S. M. Bukki, R. A. Muminov, and U. V. Shchebiot, At. Énerg. **40** (4), 346 (1976).

Translated by P. Pozdeev

Technical Physics Letters, Vol. 28, No. 9, 2002, pp. 757–758. Translated from Pis'ma v Zhurnal Tekhnicheskoĭ Fiziki, Vol. 28, No. 18, 2002, pp. 13–17.

The Effect of Gamma-Irradiation on the Bandgap Width of ZnSe

V. T. Mak, V. S. Manzhara, V. I. Beizym, and V. I. Khivrich

Odessa National University, Odessa, Ukraine

Institute of Physics, National Academy of Sciences of Ukraine, Kiev, Ukraine

Institute of Nuclear Investigations, National Scientific Center, National Academy of Sciences of Ukraine, Kiev, Ukraine

e-mail: vmak@te.net.ua

Received April 2, 2002

Abstract—Exposure to gamma-radiation from a ^{60}Co source affects the exciton photoluminescence (PL) spectra of single crystal zinc selenide measured at 4.2 K. As the radiation dose increases, the exciton PL maximum first shifts toward higher energies, but then returns to the initial position (in the range of sufficiently high doses). It is concluded that this behavior is due to variations of the semiconductor bandgap width related to the radiation-stimulated solid-state recrystallization and the accumulation of radiation-induced point defects during exposure. © *2002 MAIK "Nauka/Interperiodica".*

Among numerous investigations of the radiation effects in semiconductor materials and structures, only a small part are devoted to the study of radiation-induced changes in the bandgap width. In all reported cases, the bandgap width of semiconductors irradiated with nuclear particles was found to decrease. This effect was attributed either to a high concentration of the radiation-induced point defects or to a degradation of the crystal lattice at high doses of heavy nuclear particles (fast neutrons, protons, and ions) or high-energy electrons. At the same time, we have demonstrated [1, 2] that the radiation-stimulated processes related to a high level of ionization during irradiation may also significantly influence the final radiation effects. The role of the ionization factor increases in semiconductors with a higher fraction of ionic bonds [3]. In this context, it is natural to expect that a covalent semiconductor with a certain fraction of ionic bonds (such as zinc selenide) would exhibit a response to exposure even at small doses of gamma-radiation from a ^{60}Co source.

We studied the effect of exposure to various doses of gamma-radiation on the photoluminescence (PL) and the structure of ZnSe single crystals grown from melt under pressure. The PL spectra were measured on freshly cleaved samples at 4.2 K in the region of the fundamental absorption edge. The structure of single crystals was studied by X-ray topography and X-ray diffraction techniques.

The PL spectrum of the initial (unirradiated) ZnSe crystals (Fig. 1. curve *1*) displays emission peaks due to excitons bound on a neutral acceptor (I_1), together with the corresponding phonon satellites, and the peaks due to excitons bound on a neutral donor (I_2) [4]. After exposure, the peaks of the exciton emission shift toward higher energies (Fig. 1, curve *2*), while intensities of both the phononless bands and their phonon satellites vary rather insignificantly. The shift δ exhibits a nonmonotonic dependence on the gamma-radiation dose, reaching a maximum (~12 meV) at a dose of about 10^4 rad.

Figure 2 shows the dose dependence of the shift of emission peaks in the PL spectra of gamma-irradiated ZnSe crystals. A special feature of this dose dependence is that the shift δ first increases in the region of small doses ($D \le 10^4$ rad) and then decreases when the doses D exceed 10^5 rad. The experimental nonmono-

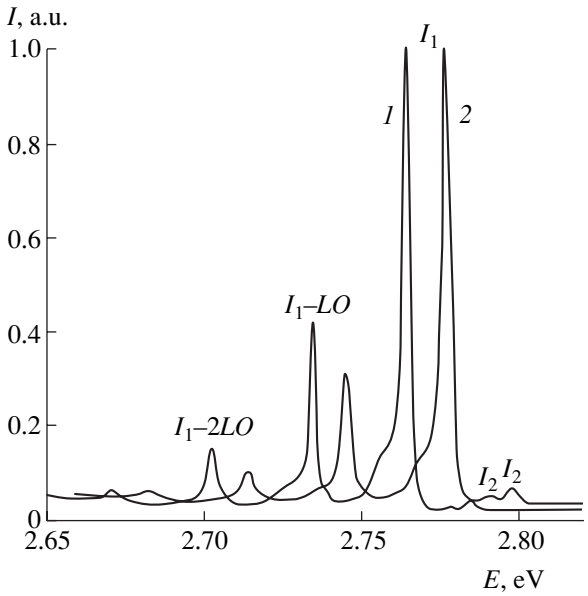

Fig. 1. PL spectra of a ZnSe single crystal measured at 4.2 K (*1*) before and (*2*) after gamma-irradiation to a dose of 10^4 rad.

1063-7850/02/2809-0757$22.00 © 2002 MAIK "Nauka/Interperiodica"

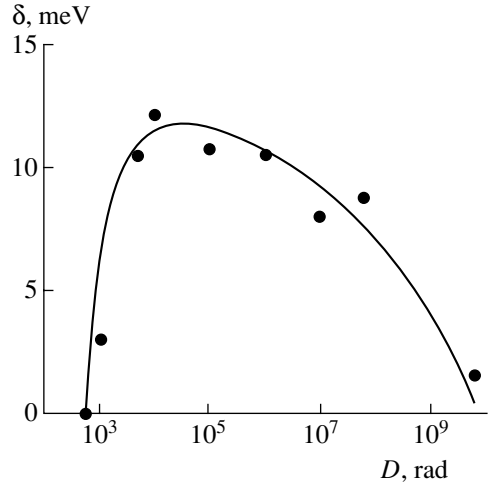

Fig. 2. Dose dependence of the PL peak shift δ (or a change in the bandgap width E_g) in gamma-irradiated ZnSe crystals.

tonic dose dependence of the positions of exciton PL bands of ZnSe single crystals can be explained assuming the presence of two competitive processes in the samples. One of these processes, dominating at small doses, increases the δ value, while the other process, prevailing at higher doses, shifts the bands back toward the longwave spectral region.

As is known [5], the energy of a photon emitted due to bound excitons is determined by the expression

$$h\nu = E_g - E_i - E_i^c,$$

where E_g is the semiconductor bandgap width, $E_i = \frac{2\pi^2\mu e^4}{h^2\varepsilon}$ is the intrinsic exciton energy for the quantum number $n = 1$, and E_i^c is the energy of exciton binding to a neutral donor or acceptor (notation as in [5]). The intrinsic exciton energy is 25 meV and is not affected by irradiation. Since the energies of exciton binding to the neutral donor and acceptor are different, the positions of emission maxima corresponding to such excitons differ as well. If irradiation could influence the intrinsic exciton energy, the shifts of the bands of excitons bound to the neutral donors and acceptors would be different. In our experiments, the shifts coincided to within the experimental error. From this we may conclude that gamma-irradiation affects the bandgap width of zinc selenide. This change in the bandgap width is equal to the shift of the exciton PL band maximum.

As for the reasons of this variation of the semiconductor bandgap width under the action of radiation, we may suggest the following. According to [2, 3, 6], semiconductor compounds may feature the process of solid-state recrystallization under the action of small gamma-radiation doses. These processes lead to the formation of a new crystalline phase, accompanied by a change in the size of grains, shift of the grain boundaries, growth of crystal blocks, etc. Since the energy band structure of a semiconductor depends on the crystal structure, the radiation-stimulated recrystallization process unavoidably changes the bandgap width of the irradiated material.

Radiation-stimulated low-temperature recrystallization in zinc selenide was confirmed by X-ray diffraction and topography investigations. The X-ray topographs reveal a clearly pronounced block structure of ZnSe crystals before irradiation, which almost completely disappears after exposure. Moreover, while the X-ray diffraction patterns of the initial samples display only reflections corresponding to a sphalerite phase, the diffractograms of gamma-irradiated ZnSe crystals exhibit reflections which can be assigned to a wurtzite phase.

Apparently, the aforementioned solid-state recrystallization process dominates at small doses of gamma-radiation. This very process is responsible for an increase in the bandgap width observed in irradiated zinc selenide. At high radiation doses, the samples accumulated radiation-induced point defects, leading to the appearance of "tails" in the density of states in the bandgap. This is probably manifested by a decrease in the bandgap width. This hypothesis is confirmed by a longwave shift of the fundamental absorption edge observed for the samples exposed to large radiation doses. Interplay of the two radiation-stimulated processes leads to the observed nonmonotonic variation of the δ value (Fig. 2).

Thus, we have observed for the first time a nonmonotonic variation of the positions of exciton emission bands in the PL spectra of zinc selenide crystals exposed to various doses of gamma-radiation. This behavior can be explained by the presence of two competitive processes: (i) radiation-stimulated solid-state recrystallization increasing the bandgap width at small radiation doses and (ii) accumulation of the radiation-induced point defects leading to a decrease in the bandgap width at large exposures.

Acknowledgments. The authors are grateful to V.P. Tsvirgun for his help in conducting gamma-irradiation of the samples.

REFERENCES

1. V. T. Mak, Fiz. Tekh. Poluprovodn. (St. Petersburg) **30** (2), 292 (1996) [Semiconductors **30**, 162 (1996)].
2. V. T. Mak, Pis'ma Zh. Tekh. Fiz. **15** (12), 17 (1989) [Sov. Tech. Phys. Lett. **15**, 461 (1989)].
3. V. T. Mak, Author's Abstract of Doctoral Dissertation in Physics and Mathematics (Chernivets'kiĭ Derzh. Univ., Chernovtsy, 1997).
4. P. J. Dean and J. L. Merz, Phys. Rev. **178** (3), 1310 (1969).
5. V. V. Serdyuk and Yu. F. Vaksman, *Luminescence of Semiconductors* (Vyshcha Shkola, Kiev, 1988).
6. V. T. Mak, V. E. Bukovskiĭ, and M. Ya. Rakhlin, Fiz. Tverd. Tela (Leningrad) **31** (9), 251 (1989) [Sov. Phys. Solid State **31**, 1619 (1989)].

Translated by P. Pozdeev

Technical Physics Letters, Vol. 28, No. 9, 2002, pp. 759–761. Translated from Pis'ma v Zhurnal Tekhnicheskoĭ Fiziki, Vol. 28, No. 18, 2002, pp. 18–23.

The Effect of Copper Atoms on the Graphite Structure

V. D. Andreeva and T. R. Stepanova

St. Petersburg State Technical University, St. Petersburg, Russia

e-mail: szss@ctinet.ru

Received April 15, 2002

Abstract—It is experimentally demonstrated that incorporated copper atoms change the electron density and, hence, modify the structure of graphite crystal planes. Using the proposed method, it is possible to calculate the function describing structural distortions and to determine the displacements of atoms in the distorted crystal planes. *© 2002 MAIK "Nauka/Interperiodica".*

Interest in carbon-based materials is related to the large possibilities of modifying their structure. The lability of structures consisting of carbon atoms allows their physical properties to be controlled within broad limits. We have studied the structure of graphite containing incorporated copper atoms. The thermodynamic stability of graphite is explained by delocalization of the p_z electrons (the orbitals of which are perpendicular to the planes of molecular grids and form a common electron system as a result of the σ–π conjugation), rather than by the presence of $sp^2(s, p_z, p_y)$ hybridized orbitals at the carbon atoms. Otherwise, diamond would be the main thermodynamically stable form of graphite in nature.

Among isoelectronic analogs of carbon, only boron nitride possesses a stabler hexagonal layered structure. The other compounds (such as BeO, AlN, AlP, BP, and BAs) exist in the form of compact structures featuring sp^3 hybridized orbitals. Transition metal atoms (possessing incomplete *d* electron shells) may induce a decrease in localization of the p_z electrons in the molecular layers of graphite. The *d* orbitals of such metal atoms, incorporated into a space between the graphite grids, overlap with the π orbitals of graphite, thus reducing the delocalization of electrons in the direction of molecular grids. Interaction between the incorporated metal and graphite carbon atoms may take the form of both sufficiently strong contacts involving *d* electrons of the metal and weak van der Waals bonds. The ratio of different contacts determines the degree of breakage of the delocalized electron system in modified graphite.

Thus, even small additives of the transition metals change the transport properties of graphite and decrease the values of the thermodynamic parameters (temperature and pressure) for the phase transition from graphite to diamond [1]. Therefore, it is of considerable interest to study the influence of incorporated transition metal atoms on the graphite structure. The choice of copper is explained by the fact that this metal does not form carbides.

Experimental. The structure of samples was studied on a DRON-2.0 diffractometer using monochromatized FeK_α radiation. The samples represented highly oriented pyrolytic graphite (HOPG) containing intercalated copper atoms. The intercalation of copper was achieved by a 20-min exposure of graphite in a melt of high-purity copper (99.99% Cu) at 1473 K under vacuum.

As can be seen from experimental data presented in the table, the X-ray diffraction pattern of the initial graphite (sample 1) corresponds to a single crystal of hexagonal graphite with a lattice parameter of c_0 = 0.672 nm. Intensities of the (002), (004), and (006) reflections correspond to standard values. A diffractogram of copper-containing graphite (sample 2) exhibits splitting of the lines corresponding to the initial graphite structure and displays two additional smeared (diffuse) reflections.

Analysis of results. Let us consider the effect of distortions in the hexagonal structure, considered as a set of atomic planes (layers) [2], on the observed X-ray diffraction pattern. We assume that the positions of layers in the distorted structure correspond to an ideal lattice, except for atoms in some planes being displaced along vector **c**. Each plane, occurring at a distance of $R_u = uc_0$ from the origin, contributes to the total amplitude as

$$A_u(\mathbf{h}) = E_e F_u(\mathbf{h}) \exp\left(-i\frac{2\pi}{\lambda}\mathbf{h}\cdot\mathbf{R}_u\right).$$

The structural amplitude factor $F_u(\mathbf{h})$ changes from one layer to another, depending on the particular arrangement of atoms in the layer with the coordinate *u*. Then,

Characteristics of the X-ray diffraction patterns of HOPG (sample 1) and copper-modified graphite (sample 2)

Sample 1		Sample 2		*d*, nm	*hkl*
θ_{max}	*I*, a.u.	θ_{max}	*I*, a.u.		
–		≈7°42′	0.3	0.7	001
16°48′	100	16°48′ 16°0′	97	0.336	002
–		≈26°12′	0.2	0.2	003
35°12′	6	35°12′ 35°24′	100	0.168	004
59°54′	1	59°54′ 60°6′	73	0.112	006

the expression for the total intensity scattered from a crystal containing *N* layers is

$$I(\mathbf{h}) = \sum_{\{u\}}\sum_{u'} A_u(\mathbf{h})A_{u'}^*(\mathbf{h}) = I_e\sum_{n=-\infty}^{\infty}(N-|n|)\langle F_{n+n'}F_{u'}^*\rangle\exp\left(-i\frac{2\pi}{\lambda}\mathbf{h}\cdot{}_n\mathbf{R}\right). \quad (1)$$

The current value of the structural amplitude F_u can be presented as a sum of the average value $\langle F\rangle$ and the fluctuation ΔF_u:

$$F_u = \langle F\rangle + \Delta F_u.$$

Taking into account that $\langle\Delta F\rangle = 0$, we obtain the relation

$$\langle F_{n+u'}F_{u'}^*\rangle = |\langle F\rangle|^2 + \Phi^{\Delta}(n,\mathbf{h}),$$

where $\Phi^{\Delta}(n,\mathbf{h}) = \langle\Delta F_{n+u'}\Delta F_{u'}^*\rangle$ is the average value of the autocorrelation function of the structural amplitude fluctuations.

Now, expression (1) can be rewritten as

$$I(\mathbf{h}) = I_e|\langle F\rangle|^2\sum_{n=-\infty}^{\infty}(N-|n|)\exp\left(-i\frac{2\pi}{\lambda}\mathbf{h}\cdot{}_n\mathbf{R}\right) + I_e\sum_{n=-\infty}^{\infty}(N-|n|)\Phi^{\Delta}(n,\mathbf{h})\exp\left(-i\frac{2\pi}{\lambda}\mathbf{h}\cdot{}_n\mathbf{R}\right).$$

Here, the first term,

$$I_1(\mathbf{h}) = I_e|\langle F\rangle|^2\sum_{n=-\infty}^{\infty}(N-|n|)\exp\left(-i\frac{2\pi}{\lambda}\mathbf{h}\cdot{}_n\mathbf{R}\right),$$

corresponds to the usual Bragg diffraction pattern, while the second term,

$$I_2(\mathbf{h}) = I_e\sum_{n=-\infty}^{\infty}(N-|n|)\Phi^{\Delta}(n,\mathbf{h})\exp\left(-i\frac{2\pi}{\lambda}\mathbf{h}\cdot{}_n\mathbf{R}\right),$$

describes the influence of fluctuations in the positions of atoms in the given layer. The form of the I_2 function is entirely determined by the Fourier transform of the function $\Phi^{\Delta}(n)$ (whereas the Fourier transform of the function $\hat{F}[N-|n|]$ yields the usual form factor).

When defective layers *A*' replace part of the ideal layers *A*' in the sequence of layers *ABAB* characteristic of the hexagonal graphite structure, the resulting fluctuation ΔF depends on the coordinate *u* of the plane. Since the *AA*' spacing is constant, the function $\Phi^{\Delta}(n)$ acquires a phase factor,

$$\Phi^{\Delta}(n) = \Phi_0^{\Delta}\exp\left(-i\frac{2\pi}{\lambda}{}_{\Delta}\mathbf{h}\cdot\mathbf{R}_n\right),$$

and the Fourier transform changes to

$$\hat{F}\left[\Phi_0^{\Delta}\exp\left(-i\frac{2\pi}{\lambda}{}_{\Delta}\mathbf{h}\cdot\mathbf{R}_n\right)\right] = \Phi_0^{\Delta}\delta(\mathbf{h}+{}_{\Delta}\mathbf{h}).$$

This change corresponds to the appearance of a second maximum near the Bragg reflection, in agreement with the experimental pattern (see the table). In this case, the lattice parameter remains unchanged (c_0 = 0.672 nm) and the planes stay in the ideal positions, while some changes take place inside the layers.

The phase factor is also responsible for another feature—diffuse reflections with odd *l*, (001) and (003)—appearing in the X-ray diffraction pattern. As is well known, the symmetry of the hexagonal graphite lattice, possessing a sixth-order screw axis, results in that reflections from the adjacent atomic planes are characterized by a phase difference of πl. For this reason, only the reflections with even indexes *l* are retained among all (00*l*) diffraction reflections. A change in the phase difference leads to the appearance of weak reflections not typical of the ideal hexagonal graphite structure.

An analysis of the X-ray diffraction pattern of graphite containing intercalated copper atoms showed evidence of the appearance of planes in which atoms are displaced from the initial positions as indicated in the figure. These are two possible variants of such dis-

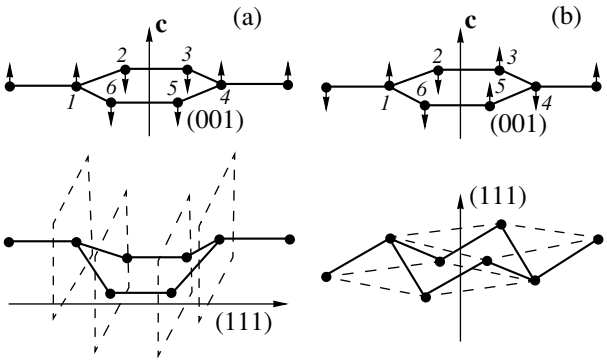

Schematic diagrams showing the pattern of atomic displacements in two variants of the corrugated planes of copper-intercalated graphite. The top row presents the initial layers and indicates the directions of displacements for shear deformation; the bottom row shows the distorted configurations and the positions of close-packed planes in the tetrahedral structures.

placements [3]. At present, we cannot differentiate between these variants and we use the term "corrugated planes," which refers to both defective configurations. Since it is energetically unfavorable for metal atoms to occupy positions on both sides of the same grid, the corrugated planes in the modified graphite structure alternate with normal ones. The relative number of corrugated plates estimated from the experimental data amounts to about 5%.

Thus, copper atoms intercalated into the graphite structure form intermediate complexes. The two-dimensional graphite grids, albeit retained, are characterized by a less stable delocalized electron system as compared to that of pure graphite. A metal atom can migrate from one pair of graphite carbon rings to another. As a result of such transitions, the liberated p_z electrons of carbon atoms form sp^3 orbitals (rather than π bonds) with s, p_x, and p_y electrons. That is, as soon as a metal atom leaves a given pair of graphite carbon rings in the grid plane, "diamond" bonds are immediately formed and a corrugated molecular grid appears at the site from which the metal atom escaped.

Conclusion. We have presented X-ray diffraction data indicative of a change in graphite structure upon the incorporation of copper atoms. Although the hexagonal graphite structure is "on average" retained, there appear corrugated planes with displaced atoms. The relative shift of atoms in the distorted planes along the c axis amounts to 15 ± 5 pm. Such corrugated planes appear because intercalated copper atoms induce a change in the electron density distribution in the molecular grids, whereby the liberated p_z electrons of carbon atoms form sp^3 orbitals (rather than π bonds) with s, p_x, and p_y electrons.

REFERENCES

1. V. I. Farafontov and Ya. A. Kalashnikov, Zh. Fiz. Khim., No. 4, 830 (1976).
2. D. M. Vasil'ev, *Diffraction Methods for Studying Structures* (S.-Peterb. Gos. Tekh. Univ., St. Petersburg, 1998).
3. A. V. Kurdyumov and A. N. Pilyankevich, *Polymorphous Modifications of Carbon and Boron Nitride* (Metallurgiya, Moscow, 1994).

Translated by P. Pozdeev

Technical Physics Letters, Vol. 28, No. 9, 2002, pp. 762–764. Translated from Pis'ma v Zhurnal Tekhnicheskoĭ Fiziki, Vol. 28, No. 18, 2002, pp. 24–28.

Edge Dislocations with Large Burgers Vector in Sphalerite Crystals

A. N. Buĭlov and L. N. Danil'chuk

Novgorod State University, Novgorod, Russia

e-mail: depoef@novsu.ac.ru

Received April 15, 2002

Abstract—The X-ray diffraction topography technique based on the Borrmann effect was used to study the dislocated structure of Czochralski-grown indium-doped GaAs(001) crystals. Among the growth dislocations aligned in the [001] ingot growth direction, there are dislocations with large Burgers vectors ($\mathbf{b} = a\langle 100\rangle$) and {100} slip planes. © *2002 MAIK "Nauka/Interperiodica".*

Using modern technologies developed for growing $A^{III}B^{V}$ semiconductor compounds, it is possible to obtain single crystals of gallium arsenide possessing semi-insulating properties and characterized by low densities of dislocations. One of such GaAs ingots, grown at the State Institute of Rare Metals (Moscow), was studied by X-ray topography.

The initial Czochralski-grown GaAs(In) single crystal possessed a resistivity of $2.1 \times 10^8\ \Omega$ cm, an electron mobility of 4970 cm^2/(V s), and an average dislocation density of $N_D = 1 \times 10^3$ cm^{-2}. The samples represented plane-parallel plates with a thickness of 300 μm, cut from the ingot perpendicularly to the [001] growth direction. X-ray topographs were obtained in the Laue scheme using CuK_α radiation and {220}, {400}, and {440} reflections from the systems of planes perpendicular to the (001) plate surface. For the plate thickness indicated above, the μt criterion (where μ [cm^{-1}] is the linear X-ray absorption coefficient and t [cm] is the crystal thickness) amounts to about 12, which corresponds to a "thick" crystal approximation in the dynamic theory of X-ray scattering. In this case, defects in the crystal bulk can be observed by X-ray topography using only the Borrmann effect [1].

As is known [2–4], the Borrmann effect for an X-ray wave field propagating along the axis of an edge dislocation results in that a photographic plate exposed behind the crystal will develop a multilobe black-and-white pattern (rosette) of intensity variation, which reflects the strain field around the dislocation [5]. Using this pattern, it is possible to obtain all information about the dislocation, including the dislocation axis direction relative to the crystal axes, dislocation type, positions of the extra half-plane and slip plane (for edge dislocations), and the Burgers vector sign and magnitude.

Figure 1 shows fragment of a typical X-ray topograph displaying a group of edge dislocations (*1–3*) of the same sign measured in the diffracted beam of rays for the $(\bar{4}00)$ reflection. Rosettes with similar intensity profiles were previously observed by the method of anomalous X-ray transmission in single crystals of silicon [2], germanium [3], and silicon carbide [6].

If an X-ray topograph of edge dislocations in a crystal obeys the contrast condition $(\mathbf{g} \cdot \mathbf{b}) = 2$ or 4 (where $\mathbf{g}$ is the diffraction vector and $\mathbf{b}$ is the Burgers vector) and the Poynting vector of the crystal coincides with the dislocation axis, the topograph displays a symmetrical 10-lobe black-and-white rosette with a zero-contrast line in the slip plane. The four central lobes are due to the intrinsic field of the dislocation (strain field in the bulk of the crystal), while the other lobes are due to the relaxation field at the ray exit plane [4]. A compression zone near the extra half-plane on the X-ray topograph exhibits a positive contrast (two black central lobes), while the decompression zone below the extra half-plane shows a negative contrast (two bright central lobes).

The dislocation rosettes in Fig. 1 display six lobes. The four central lobes are due to the intrinsic disloca-

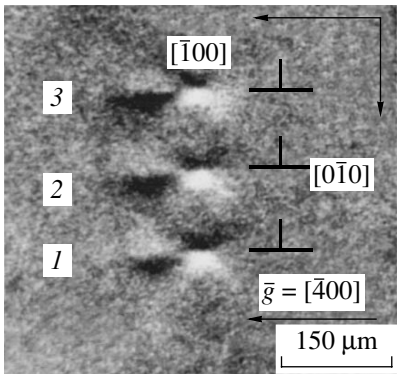

Fig. 1. Experimental X-ray topograph showing edge dislocations in GaAs(In) with large Burgers vectors in the diffracted beam of rays (positive).

tion field, while two lobes on the left are due to the relaxation field. This asymmetry reflects anisotropy of the elastic properties of the crystal at the free surface. As can be seen from Fig. 1, all three dislocations possess $(0\bar{1}0)$ slip planes. The zones of compression at the extra half-planes exhibit a positive contrast ($J_D = J_T > J_0$). Therefore, dislocations *1–3* are characterized by Burgers vectors of the same sign and direction. Since the rosettes have the same diameters, the magnitudes of the Burgers vectors for the tree dislocations are also equal to each other ($\mathbf{b}_1 = \mathbf{b}_2 = \mathbf{b}_3 = na[\bar{1}00]$).

Based on the principle of minimum dislocation energy, we may suggest that dislocations *1–3* possess Burgers vectors $\mathbf{b} = a[\bar{1}00]$. In order to verify this hypothesis, we performed computer modeling of the intensity contrast and constructed the image of an edge dislocation with the [001] axis, (010) slip plane, and Burgers vector $|\mathbf{b}| = a[\bar{1}00] = 5.65 \times 10^{-4}$ μm.

The calculation was performed using the refined Indenbom–Chamrov equations for the electron-microscopic contrast, modified in application to anomalous X-ray transmission [7, 4]:

$$\left.\begin{aligned} \delta_D &= \frac{J_D - J_D^0}{J_D^0} = -\frac{W_{2a} + W_{2b}}{\gamma_2} \\ \delta_T &= \frac{J_T - J_T^0}{J_T^0} = -\frac{W_{2a} - W_{2b}}{\gamma_2} \end{aligned}\right\}. \qquad (1)$$

Here, J_D and J_T are the intensities of diffracted and transmitted waves at a given point of the image; $J_D^0 = J_T^0 = J_0$ is the background intensity (for the undistorted crystal); and W_{2a}, W_{2b}, and γ_2 are the parameters characterizing deformation of the reflecting planes at the ray exit plane:

$$W_{2a} = \Lambda|\mathbf{g}|\frac{dU_g}{dx_g}\tan\theta; \quad W_{2b} = \Lambda\mathbf{g}\frac{d\mathbf{U}}{dz};$$

$$\gamma_2 = \sqrt{1 + W_2^2}; \quad W_2 = W_{2a} + W_{2b}.$$

In these formulas, Λ is the extinction length, **U** is the displacement vector, and θ is the Bragg angle. Once the field of displacements $\mathbf{U}(\mathbf{r})$ around a dislocation is known [8], the intensity distribution can be readily calculated by Eqs. (1) and a theoretical image or a topograph of the dislocation can be reconstructed.

Figure 2 shows a theoretical topograph of a single edge dislocation with the [001] axis, Burgers vector $\mathbf{b} = [\bar{1}00]$, and (010) slip plane. The computer modeling was performed using a program written by A.O. Okunev at the Physical Research Center of Novgorod State University. The results of calculations were plotted using a 64-level intensity scale, with an average level corresponding to J_0. A minimum contrast was adopted at $\delta_{min} \pm 5\%$. In order to simplify the theoretical topograph in Fig. 2, the calculation took into account only the intrinsic strain field around the dislocation.

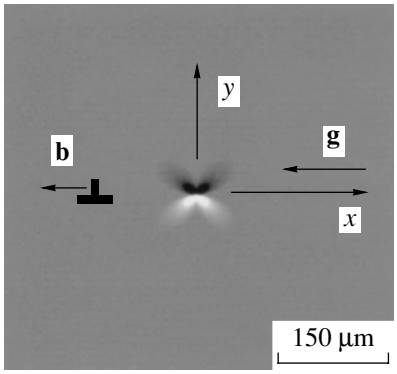

Fig. 2. A theoretical topograph of the edge dislocation with a large Burgers vector, constructed in application to the Borrmann effect with an allowance for only the main strain field component in the bulk of a GaAs crystal.

A comparison of Figs. 1 and 2 shows coincidence of the profiles, contrast signs, and dimensions of the rosettes formed by the intrinsic strain fields. Therefore, the calculation confirmed that dislocations *1–3* possess equal Burgers vectors $\mathbf{b}_1 = \mathbf{b}_2 = \mathbf{b}_3 = a[\bar{1}00]$ and the same $(0\bar{1}0)$ slip plane.

Considered as energetically unfavorable and unstable, such dislocations were never studied in the sphalerite structure [9]. However, these dislocations were observed in silicon [10] and proved to be stable with respect to splitting. Thus, we demonstrated that sphalerite crystals may feature dislocations with both small ($\mathbf{b}_1 = a/2\langle 110\rangle$ [11]) and large ($\mathbf{b}_2 = a\langle 100\rangle$) Burgers vectors.

Acknowledgments. This study was performed according to the Project "Development of Methods for Identification of Structural Defects on Single Crystal Semiconductors Based on Anomalous X-ray Transmission (State Registration no. 01200106001) and supported within the framework of the Federal Program "Higher School: Scientific Research in Special Directions of Science and Technology" (Subprogram 202 "Novel Materials;" Section 202.01 "Materials for Micro- and Nanoelectronics").

REFERENCES

1. G. Borrmann, Phys. Z. **42** (9/10), 157 (1941).
2. L. N. Danil'chuk and T. A. Smorodina, Fiz. Tverd. Tela (Leningrad) **7** (4), 1245 (1965) [Sov. Phys. Solid State **7**, 1003 (1965)].

3. L. N. Danil'chuk, Fiz. Tverd. Tela (Leningrad) **11**, 3085 (1969) [Sov. Phys. Solid State **11**, 2506 (1969)].
4. L. N. Danil'chuk, Author's Abstract of Doctoral Dissertation in Physics and Mathematics (IMF Akad. Nauk Ukrainy, Kiev, 1992).
5. É. V. Suvorov and I. L. Shul'pina, Poverkhnost, No. 7, 3 (2001).
6. A. O. Okunev, Author's Abstract of Candidate's Dissertation in Physics and Mathematics (Novgor. Gos. Univ., Novgorod, 1999).
7. V. L. Indenbom and V. A. Chamrov, Metallofizika **2** (3), 3 (1980).
8. J. P. Hirth and J. Lothe, *Theory of Dislocations* (McGraw-Hill, New York, 1967; Atomizdat, Moscow, 1972).
9. D. B. Holt, in *Defects in Crystals of Semiconductors* (Mir, Moscow, 1969), pp. 100–118.
10. L. S. Milevskiĭ and V. D. Khvostikov, *Growth and Imperfections of Metallic Crystals* (Naukova Dumka, Kiev, 1966), pp. 261–265.
11. L. S. Milevskiĭ, in *Proceedings of the All-Union Conference on Structural Defects in Semiconductors* (Sib. Otd. Akad. Nauk SSSR, Novosibirsk, 1969), Part 1, pp. 253–269.

Translated by P. Pozdeev

Technical Physics Letters, Vol. 28, No. 9, 2002, pp. 765–766. Translated from Pis'ma v Zhurnal Tekhnicheskoĭ Fiziki, Vol. 28, No. 18, 2002, pp. 29–33.

On the Coherence of X-ray Beams Focused by Bent Crystals

T. Tchen

Moscow State Academy of Fine Chemical Technology, Moscow, Russia
e-mail: docent65@mtu-net.ru; ttchen@e-mail.ru

Received May 6, 2002

Abstract—The spatial and temporal coherence of X-ray beams focused by bent crystals is considered for some practical schemes (backscattering and Johann schemes) widely employed in X-ray optics. It is shown that a high beam intensity achieved with crystal optics employing the Johann and backscattering schemes leads to incoherent focusing. *© 2002 MAIK "Nauka/Interperiodica".*

In recent years, development of the third generation of synchrotron radiation sources inspired a new wave of interest in problems pertaining to the focusing and control of X-ray beams by means of crystal optics employing bent crystals. The well-known Johann scheme [1–6] and backscattering scheme [7–19] are the most attractive solutions. A considerable advantage of these schemes over many others is the possibility of obtaining X-ray beams of high intensity.

This communication is devoted to the problem of coherent focusing in the Johann and backscattering schemes. First, let us consider the role of spatial coherence in the focusing of X-ray beams by bent crystals. Below, we denote by $2a_{s,\xi}$ and $2a_{s,y}$ the dimensions of the X-ray source in the plane of diffraction and in the perpendicular plane, respectively (see figure). The maximum source size for which the coherence of the incident beam can be retained can be estimated from the condition

$$2a_{s,\xi} \le \lambda/(2\Delta\theta). \quad (1)$$

Here, λ is the incident radiation wavelength and $\Delta\theta$ is the angle between rays emitted from the source ends and striking the crystal center.

Taking the angle $\Delta\theta$ in (1) equal to the angular divergence $\Delta\theta_{Johann}$ of the beam incident onto the crystal in the Johann scheme, we obtain an estimate for the "coherent" source size $2a_{s,\xi}$ in this scheme:

$$2a_{s,\xi,Johann} \le \lambda\sin 2\theta_B/(4|\chi_{hr}|^{1/2}). \quad (2)$$

Here, χ_{hr} is the Fourier component of the X-ray polarizability of the crystal employed and θ_B is the Bragg diffraction angle. Relation (2) was derived taking into account that $\Delta\theta_{Johann} \approx x_{eff,Johann}/(R_x\sin\theta_B)$, where R_x is the radius of crystal bending in the plane of diffraction and $x_{eff,Johann}$ is an effective parameter given by the formula [20]:

$$x_{eff,Johann} = R_x(2\Delta\theta_{TRR}\tan\theta_B)^{1/2}; \quad (3)$$

$\Delta\theta_{TRR} = |\chi_{hr}|/\sin 2\theta_B$ is the angular halfwidth of the total reflection region.

Considering the backscattering scheme, where $\theta_B \cong \pi/2$ and $L_0 = R_x\sin\theta_B$, and using results obtained previously [21], we obtain for the coherent source size

$$2a_{s,\xi\theta\approx\pi/2} \le \lambda/(2|\chi_{hr}|^{1/2}). \quad (4)$$

A comparison of expressions (2) and (4) shows that the backscattering scheme allows using somewhat larger sources (as compared to the Johann scheme) without violation of the coherent focusing condition.

In the plane perpendicular to the diffraction plane, estimates of the coherent source size $2a_{s,y}$ coincide in order of magnitude with the values provided by condition (4).

A numerical estimate for a (20) reflection of the CuK_α radiation from a silicon single crystal yields $2a_{s,\xi,Johann} \le 10^{-8}$ m. Thus, using radiation sources with dimensions from 1 to 10 μm, we obtain incoherent focusing in the Johann scheme. Therefore, using the

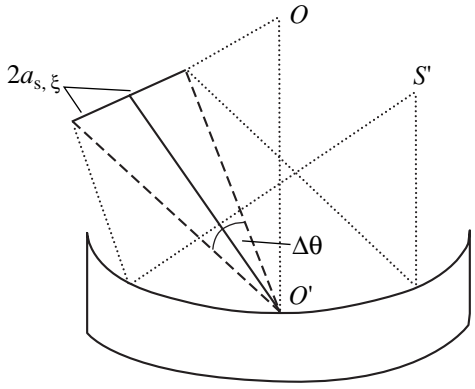

A schematic diagram illustrating the effect of the source size on the coherent focusing (*S'* is the source image, $|OO'| = R_x$).

1063-7850/02/2809-0765$22.00 © 2002 MAIK "Nauka/Interperiodica"

Huygens–Fresnel principle [22] in X-ray optics with such sources is not quite correct.

It should be noted that, as can be seen from (1), flat crystals allow using greater radiation sources as compared to those permitted by the bent crystals. However, a flat crystal not subjected to any external factor (mechanical bending, temperature gradient, acoustic action, linear variation of the lattice period, etc.) cannot provide focusing of a diffracted Bragg's wave into a point. With such a crystal, it is only possible to decrease the diffracted beam cross section upon sharply asymmetric diffraction, which provides for a gain in the beam intensity.

Putting $\Delta\theta \approx 2a_{s,\xi}/L_0$ (L_0 is the distance from source to crystal) in condition (1), we can describe the dependence of the coherent source size on the parameter L_0:

$$a_{s,\xi} \leq (\lambda L_0)^{1/2}(8)^{1/2}. \quad (5)$$

As can be seen from this condition, for a plane incident wave (synchrotron radiation source, $L_0 \gg R_x \sin\theta$) with $\Delta\theta_{pl} \ll \Delta\theta_{TRR}$, the focusing remains coherent for somewhat larger sources. For example, in a system with $L_0 \approx$ 20 m, $2a_{s,\xi,pl} \leq 90$ μm.

Let us consider the effect of nonmonochromaticity of the incident radiation on the possibility of coherent focusing. In order to retain coherence, we pose the requirement

$$L_{coh} = \lambda^2/\Delta\lambda > x_{eff,\,Johann}. \quad (6)$$

Using formula (3), we obtain from (6) the following conditions for the aforementioned radiation and diffraction schemes: $\Delta\lambda < \lambda^2\cos\theta_B/(R_x|\chi_{hr}|^{1/2}) \sim 0.7 \times 10^{-17}$ m (for $R_x \sim 1$ m), which corresponds to the degree of monochromaticity $\delta\lambda/\lambda \sim 5 \times 10^{-8}$. Theoretically, this level of monochromaticity can be achieved with a monochromator employing multiple Bragg reflections. Using more realistic values in the interval $\Delta\lambda/\lambda \sim 10^{-4} - 10^{-6}$ implies violation of the temporal coherence. The coherence time can be estimated as $\tau_{coh} \sim L_{coh}/c \sim 2.5 \times 10^{-3}$ s for $\Delta\lambda \sim 10^{-17}$ m (c is the velocity of light in vacuum).

Thus, it was demonstrated that X-ray radiation focusing in the Johann scheme is incoherent for radiation sources with dimensions greater than 1–10 μm, typically employed in experiments. An increase in the output beam intensity, which can be provided by bent crystals, is achieved at the expense of a decrease in the length of spatial coherence. With synchrotron radiation sources, the focusing of X-ray beams by bent crystals remains coherent. Another advantage of synchrotron radiation sources over the usual X-ray tubes is a high power of the former. Optimum focusing of a usual X-ray beam can be achieved only by compromising between the acceptable coherency and required intensity of the radiation.

REFERENCES

1. H. H. Jahann, Z. Phys. **69**, 185 (1931).
2. K. T. Gabrielyan, F. N. Chukhovskiĭ, and Z. G. Pinsker, Zh. Tekh. Fiz. **50**, 3 (1980) [Sov. Phys. Tech. Phys. **25**, 1 (1980)].
3. F. N. Chukhovskiĭ, Metallofizika **3**, 3 (1981).
4. D. B. Wittry and S. Sun, J. Appl. Phys. **67** (4), 1633 (1990).
5. W. Z. Chang and D. B. Wittry, J. Appl. Phys. **74** (5), 2999 (1993).
6. F. N. Chukhovskii, W. Z. Chang, and E. Förster, J. Appl. Phys. **77** (5), 1843 (1995).
7. K. Kohra and T. Matsushita, Z. Naturforsch. A **27**, 484 (1972).
8. O. Brümmer, H. R. Höche, and J. Hieber, Phys. Status Solidi A **53**, 565 (1979).
9. A. Caticha and S. Caticha-Ellis, Phys. Rev. B **25**, 971 (1982).
10. A. Caticha and S. Caticha-Ellis, Phys. Status Solidi A **119**, 47 (1990).
11. W. Graeff and G. Materlik, Nucl. Instrum. Methods **195**, 97 (1982).
12. V. I. Kushnir and É. V. Suvorov, Pis'ma Zh. Éksp. Teor. Fiz. **44**, 205 (1986) [JETP Lett. **44**, 262 (1986)].
13. V. I. Kushnir and É. V. Suvorov, Phys. Status Solidi A **122**, 391 (1990).
14. S. Kikuta, Y. Imai, T. Iizuka, *et al.*, J. Synchrotron Radiat. **5**, 670 (1998).
15. Yu. Svyd'ko, E. Gerdau, J. Jäschke, *et al.*, Phys. Rev. B **57**, 4968 (1998).
16. Yu. V. Shvyd'ko and E. Gerdau, Hyperfine Interact. **123**/**124**, 741 (1999).
17. Yu. V. Shvyd'ko, M. Lucht, E. Gerdau, *et al.*, J. Synchrotron Radiat. **9**, 17 (2002).
18. V. G. Kohn, Yu. V. Shvyd'ko, and E. Gerdau, Phys. Status Solidi B **221**, 597 (2000).
19. A. Yu. Nikulin, J. R. Davis, N. T. Jones, *et al.*, Phys. Status Solidi A **179**, 103 (2000).
20. T. Tchen, Pis'ma Zh. Tekh. Fiz. **27** (21), 1 (2001) [Tech. Phys. Lett. **27**, 889 (2001)].
21. T. Tchen, Kristallografiya **47** (2), 208 (2002) [Crystallogr. Rep. **47**, 174 (2002)].
22. K. T. Gabrielyan, F. N. Chukhovskiĭ, and D. I. Piskunov, Zh. Éksp. Teor. Fiz. **96** (3), 834 (1989) [Sov. Phys. JETP **69**, 474 (1989)].

Translated by P. Pozdeev

Technical Physics Letters, Vol. 28, No. 9, 2002, pp. 767–770. Translated from Pis'ma v Zhurnal Tekhnicheskoĭ Fiziki, Vol. 28, No. 18, 2002, pp. 34–42.

Synchronized Autooscillations in a Distributed System of the "Helical Electron Beam–Opposite Electromagnetic Wave" Type

D. I. Trubetskov and A. E. Khramov

Saratov State University, Saratov, Russia
State Scientific Center "College", Saratov, Russia
e-mail: aeh@cas.ssu.runnet.ru

Received April 1, 2002

Abstract—The phenomenon of synchronization of self-oscillations is studied for the first time in an active distributed system of a helical electron beam interacting with an opposite wave in a waveguide (representing a cyclotron-resonance opposed-wave maser). The parameters of oscillations in the distributed self-oscillatory system are considered in the regime of synchronized self-oscillations and upon escape from this regime. © *2002 MAIK "Nauka/Interperiodica".*

As is known [1–4], the interaction of a helical electron beam with TE waveguide modes under conditions of synchronism between electromagnetic and electron waves,

$$\omega \approx \hat{\omega}, \quad \hat{\omega} + \beta_0(\hat{\omega})v_\parallel - \omega_c = 0, \tag{1}$$

is accompanied by the generation of high-frequency radiation. Here, ω_c is the cyclotron frequency, $v_\parallel$ is the longitudinal electron velocity, and $\hat{\omega}$ is the synchronization frequency. Such a system, representing a cyclotron-resonance opposed-wave maser (CROWM) features the inertial bunching of electrons related to a relativistic nonisochronism of electrons oscillating in the helical (polyhelical) beam.

A characteristic feature of the CROWM system is the possibility of effectively tuning the generation frequency by changing the longitudinal velocity of erections ($v_\parallel$) or the applied static magnetic field (B_0). It would be of interest to study the effect of various external signals on such a system. The importance of such investigations is related both to practical aspects (development of gyroscopic devices with controlled characteristics) and to basic problems pertaining to the synchronization of self-oscillations in distributed systems of arbitrary nature.

We used methods of numerical modeling to study the synchronization of self-oscillations by an external harmonic signal in a system of the "helical electron beam–opposite electromagnetic wave" type.

Previously [5, 6], the dynamics of a simple model was studied and it was demonstrated that this system features various oscillation regimes, including stationary generation, periodic automodulation, and chaotic automodulation. Below we present the results of investigation of the effect of an external harmonic signal on the CROWM oscillations in a stationary generation regime.

A system of equations describing the interaction of a helical electron beam with an opposite wave consists of the equation of motion for electrons of a weakly relativistic helical beam [2] and the equation describing excitation of the opposite wave by the electron beam [7]. Written in dimensionless variables, these equations are as follows:

$$\frac{d\beta}{d\xi} - j\mu(1 - |\beta|^2)\beta = F, \tag{2}$$

$$\frac{\partial F}{\partial \tau} - \frac{\partial F}{\partial \xi} = -\frac{1}{2\pi}\int_0^{2\pi} \beta d\theta_0, \tag{3}$$

where $\beta = r\exp(j\theta)$ is the complex radius of the trajectory of an ensemble of electrons (with initial uniform phase distribution relative to the microwave field); F is a slowly varying complex dimensionless field amplitude in the beam cross section; ξ and τ are the dimensionless longitudinal coordinate and time, respectively; and $\mu = (v_\parallel/c)/2\varepsilon$ is the parameter of nonisochronism characterizing the degree of inertia of the system studied. Equations (2) and (3) have to be solved with the following initial and boundary conditions:

$$F(\tau = 0) = f^0(\xi), \quad \beta(\xi = 0) = \exp(j\theta_0), \quad \theta_0 \in [0, 2\pi]. \tag{4}$$

The external harmonic control signal applied at the collector has the following form:

$$F(\xi = A) = F_0\exp(j\Omega\tau), \tag{5}$$

1063-7850/02/2809-0767$22.00

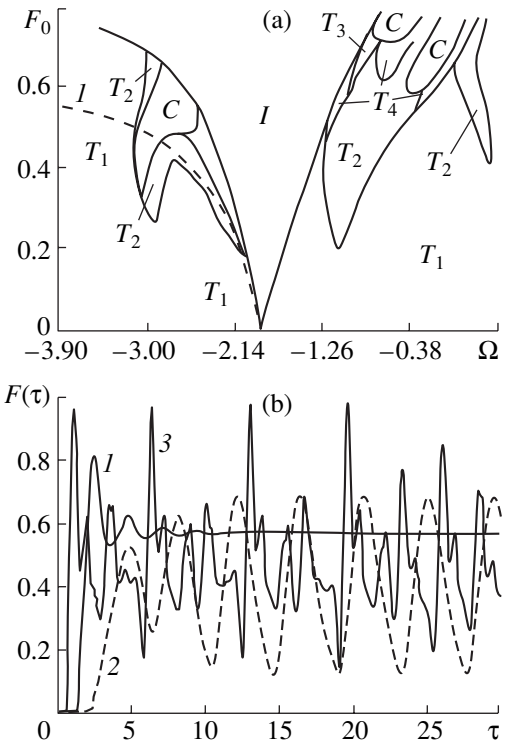

Fig. 1. (a) A map of regimes on the frequency–amplitude plane of control parameters (region *I* correspond to the synchronization domain); (b) characteristic time patterns of the output signal $F(\xi = 0, \tau)$ including transient processes observed in various regimes: (*1*) synchronization (stationary generation); (*2*) periodic automodulation; (*3*) chaotic automodulation.

where A is the dimensionless length of the system, F_0 is the control signal amplitude, Ω is the detuning of the external signal from the synchronization frequency $\hat{\omega}$ satisfying condition (1). Simplifying assumptions underlying the proposed model and the expressions for dimensionless variables are considered in detail elsewhere [5, 8].

We have studied a CROWM model with a length of $A = 3.0$ and a nonisochronism of $\mu = 2.0$, which corresponds to a regime of stationary generation with a frequency of $\omega_0 = -0.58\pi$ and an output field amplitude of $F = 0.42$. The coefficient of conversion of the transverse kinetic energy into the field energy in this regime is $\eta_\perp = 1 - (1/2\pi)\int_0^{2\pi} |\beta|^2 d\theta_0 = 0.18$, which is close to optimum [5].

Figure 1a shows subdivision of the plane of control parameters (external field amplitude F_0 versus control signal frequency Ω) into the regions corresponding to characteristic spatiotemporal regimes of oscillations in CROWM.

When the frequency Ω of the external action is close to the intrinsic frequency ω_0 of the stationary generation of the autonomous system, the generator features a synchronization regime (indicated by *I* in Fig. 1a) in which the output signal frequency ω is determined by the external control signal frequency and the output signal amplitude $F(\xi = 0, \tau)$ after termination of a transient process is established at a constant level $F = \text{const}$ (stationary generation regime). The characteristic behavior of the output signal amplitude slowly varying with time is depicted in Fig. 1b (curve *1*).

Figure 2a shows the amplitude–frequency characteristics of the CROWM, representing dependences of the output signal amplitude $|F(\xi = 0)|$ on the control signal frequency Ω within the synchronization domain, constructed for various amplitudes F_0 of the external control signal. As can be seen, the amplitude–frequency characteristic of the generator exhibits flattening with an increase in amplitude of the external signal, while the maximum value of the output signal as a function of the control frequency Ω shifts toward higher frequencies. On approaching the left synchronization wedge boundary, the amplitude of stationary synchronous oscillations decreases at a slower rate.

When the control parameters correspond to boundaries of the synchronization domain, the system exhibits a transition to the automodulation regime, in which the output signal amplitude $|F(\xi = 0, \tau)|$ becomes time-dependent (see Fig. 1b, curves *2* and *3*). This leads, depending on the particular frequency and amplitude (the latter parameter is more significant), to either periodic (Fig. 1b, curve *2*) or chaotic (Fig. 1b, curve *3*) automodulation. In the latter case, the output signal amplitude varies irregularly, performing oscillations with a broad continuous spectrum. In the plane of parameters, the regions of periodic automodulation are denoted by T_i, where subscript i indicates the period of automodulation. A characteristic time variation of the output signal amplitude in such a regime is presented in Fig. 1b (curve *2*). The regions of chaotic automodulation are denoted by *C*.

An analysis of the map of regimes in the plane of parameters shows that the regimes of periodic automodulation with a single base frequency $f_A = 1/T_A$ (T_A is the automodulation period) appear at small amplitudes F_0 of the external action. As the F_0 value increases at certain frequencies Ω, the system exhibits period doubling (T_2, whereby the spectrum of the output signal $|F(\tau)|$ contains a subharmonic of the automodulation frequency $f_A/2$), and subsequently, the automodulation regime with period 4 (T_4, whereby the output signal contains the spectral components f_A, $f_A/2$, and $f_A/4$). Additional investigation showed that the system under consideration features no automodulation regimes with periods $i > 4$.

Let us consider variation of the characteristics of the automodulation regime depending on the external signal frequency Ω and amplitude F_0. Figure 2 shows frequency dependences of the automodulation amplitude F_A and period T_A in a periodic regime for various F_0 val-

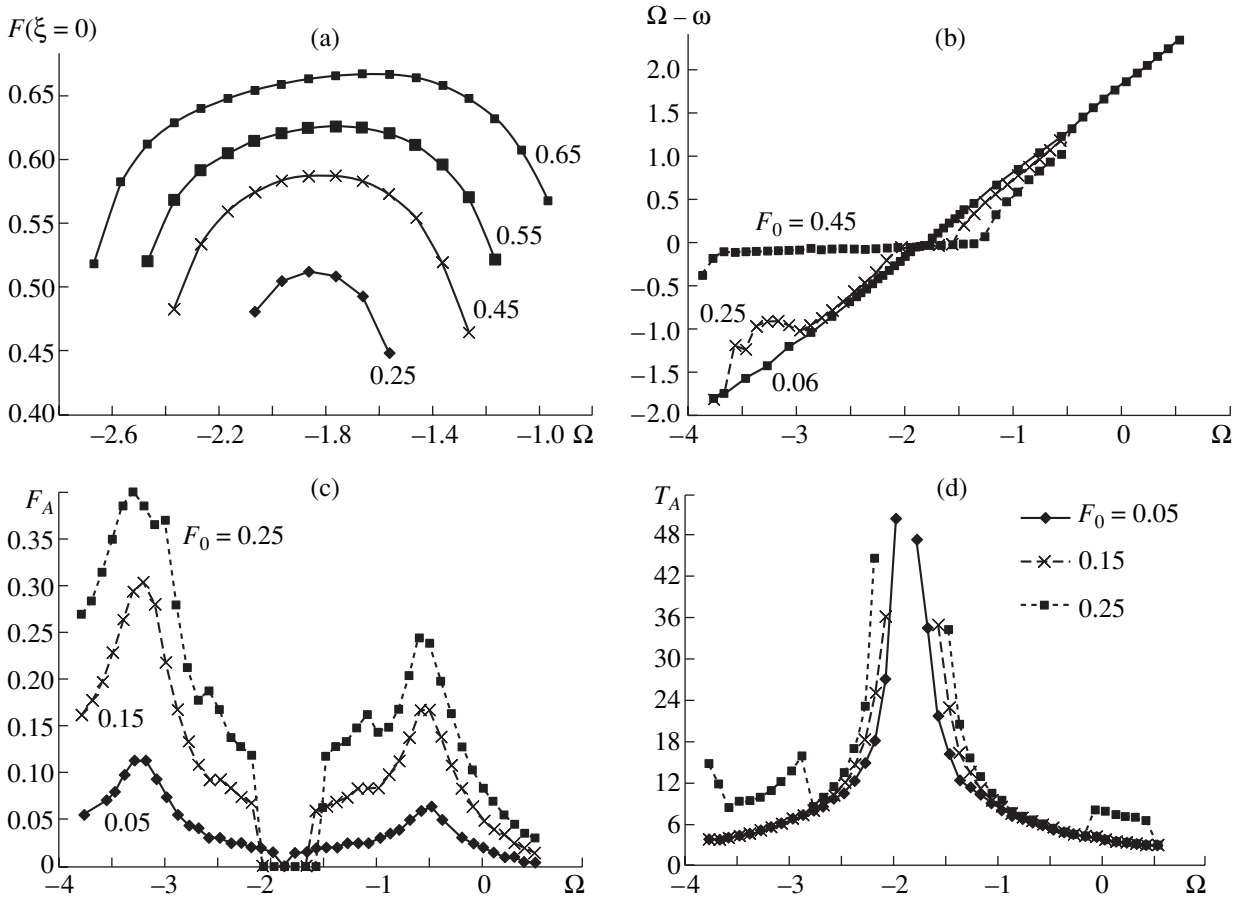

Fig. 2. Frequency dependences of (a) output signal amplitude F of an opposite-wave generator, (b) frequency difference ($\Omega - \omega$) between the control and output signal for various amplitudes F_0 of the control signal, (c) automodulation amplitude F_A, and (d) automodulation period at the boundary of the synchronization domain.

ues. Irrespective of F_0, the automodulation appears in a "hard" (threshold) manner with respect to the amplitude (Fig. 2c), as manifested by a sharp jump in F_A upon leaving the synchronization domain. The automodulation amplitude increases with detuning from the synchronization regime, reaches a maximum, and decreases again. Passage through a maximum of $F_A(\Omega)$ is accompanied by a change in the character of automodulation. At frequencies between the value corresponding to the maximum automodulation amplitude and the value corresponding to the boundary of the synchronization wedge, that is, approximately at $\Omega \in (-3.25, -2)$ and $\Omega \in (-1.6, -0.5)$, the periodic automodulation exhibits a complicated anharmonic character. On approaching the frequency corresponding to the maximum amplitude from the side of greater (smaller) values, the amplitude $F(\xi = 0, \tau)$ as a function of time acquires the form of a sequence of generation "pulses" with a large amplitude. When the external signal frequency passes a value corresponding to the maximum of the automodulation amplitude, the character of the generation exhibits a change, whereby the automodulation shape becomes close to harmonic (Fig. 1b, curve *3*).

Note also that an increase in amplitude of the external action is accompanied by a growth of the automodulation amplitude. The automodulation period (Fig. 2d) tends to infinity at the boundaries of the synchronization domain and gradually decreases with increasing detuning (this implies "soft" excitation of the regime of automodulation of the output signal).

Note that the automodulation appearing upon escape from the synchronization region of the distributed self-oscillatory system studied is not an analog of beats observed in the case of escape from synchronization regimes of the classical self-oscillatory system of finite dimensions (see, e.g., [9]). Indeed, first, the automodulation frequency ω_A is rather far from the combination frequencies ($\Omega \pm \omega$). Second, investigations of the effect of frequency (ω) locking for the high-frequency component of the output signal $F(\tau)\exp(j\omega t)$ by an external signal with the frequency Ω revealed the following phenomenon: the region of the high-frequency signal locking was significantly greater than the region of stationary generation (corresponding to the synchronization domain on the map of regimes). This is illustrated in Fig. 2b, showing plots of the frequency

difference $\Omega - \omega$ of the high-frequency oscillations at the system output versus the control signal frequency Ω for various amplitudes F_0. A comparison of Figs. 1a and 2b shows that the region of frequency locking from the side of greater frequencies (on the right in Fig. 1a) coincides with the boundary of the automodulation region (and, hence, of the synchronization domain). From the side of smaller frequencies (on the left in Fig. 1a), the control signal frequency at which the frequency locking takes place is significantly shifted relative to the boundary of the stationary generation region. In Fig. 1a, the boundary of the region of frequency locking from the side of smaller frequencies is depicted by dashed curve *1*. Note that curve *1* and the boundary of the synchronization region never cross, however small be the external signal amplitude F_0.

In the map of regimes of the nonautonomous system (Fig. 1a), the regime of oscillations occurring between curve *1* and the left boundary of the synchronization wedge can be referred to as a quasi-synchronization regime. In this region, the microwave generation takes place at the frequency of the control signal, while the output signal amplitude slowly varies at a characteristic time of $\sim T_A$.

For large amplitudes of the external action, the map of regimes exhibits several regions corresponding to chaotic automodulation. In this communication, we dwell on the chaotic generation regimes in the CROWM under the action of external harmonic signals. In concluding, we only note that regions of complicated dynamics occur in the vicinity of the boundaries of the synchronization domain.

Acknowledgments. This study was supported by the Russian Foundation for Basic Research, project nos. 01-02-17392 and 00-15-96673.

REFERENCES

1. A. V. Gaponov, Izv. Vyssh. Uchebn. Zaved., Radiofiz. **2** (3), 443 (1959).
2. V. K. Yulpatov, Vopr. Radioélektron., Ser. 1: Élektron., No. 12, 15 (1965).
3. V. K. Yulpatov, Vopr. Radioélektron., Ser. 1: Élektron., No. 12, 24 (1965).
4. *Gyrotron: Collection of Scientific Works* (Inst. Prikl. Fiz. Akad. Nauk SSSR, Gorki, 1981).
5. A. Yu. Dmitriev, D. I. Trubetskov, and A. P. Chetverikov, Izv. Vyssh. Uchebn. Zaved., Radiofiz. **34** (9), 595 (1991).
6. D. I. Trubetskov and A. P. Chetverikov, Izv. Vyssh. Uchebn. Zaved., Prikl. Nelineĭnaya Din. **2** (5), 3 (1994).
7. S. P. Kuznetsov and D. I. Trubetskov, *Electronics of Backward-Wave Tubes* (Saratovskiĭ Univ., Saratov, 1975), p. 135.
8. A. Yu. Dmitriev, A. E. Konevets, L. A. Pishchik, *et al.*, in *Lectures on Microwave Electronics and Radiophysics: Proceedings of 7th Winter School-Workshop of Engineers* (Saratovskiĭ Univ., Saratov, 1986), p. 61.
9. M. I. Rabinovich and D. I. Trubetskov, *An Introduction to the Theory of Oscillations and Waves* (Nauka, Moscow, 1988).

Translated by P. Pozdeev

Technical Physics Letters, Vol. 28, No. 9, 2002, pp. 771–772. Translated from Pis'ma v Zhurnal Tekhnicheskoĭ Fiziki, Vol. 28, No. 18, 2002, pp. 43–47.

Features of the Electrical Properties of TMA–$CuBr_4$ Crystals in the Polar Phase Region

S. N. Kallaev, I. K. Kamilov, and A. A. Amirova

Institute of Physics, Dagestan Scientific Center, Russian Academy of Sciences, Makhachkala, Dagestan, Russia

e-mail: analit@dinet.ru

Received May 20, 2002

Abstract—Anomalously large variations in the electrical properties of $[N(CH_3)_4]_2CuBr_4$ crystals manifested by the disappearance of the spontaneous polarization (ferroelectricity) under the action of small uniaxial mechanical stresses. The observed effect is reversible and nonlinear. © *2002 MAIK "Nauka/Interperiodica".*

As is known, mechanical stresses may strongly influence the state and physical properties of ferroelectric crystals by means of the piezoelectric effect. For example, by selecting the stress tensor component linearly related to the polarization, it is possible to convert a crystal from a poly- to monodomain state, which is accompanied by very significant changes in the dielectric properties [1]. Previously [2], we discovered the phenomenon of a giant change in the dielectric properties of $[N(CH_3)_4]_2ZnCl_4$ (TMA–$ZnCl_4$) crystals under the action of a small uniaxial pressure. The applied stress did not change the crystal symmetry and, in contrast to the usual piezoelectric effect, led to the reversible disappearance of ferroelectricity in the samples.

Below we report on the discovery and study of the phenomenon of disappearance of the polar (ferroelectric) structure in $[N(CH_3)_4]_2CuBr_4$ (TMA–$CuBr_4$) crystals under the action of small uniaxial stresses. At atmospheric pressure, tetramethylammonium bromide crystals exhibit phase transitions at 271, 241, and 237 K. These points separate the regions of four phases. The high-temperature phase possesses an orthorhombic structure with *Pmcn* symmetry, the phase existing within the interval 271 K > T > 241 K exhibits an incommensurate superstructure, the polar (ferroelectric) phase existing within the interval 241 K > T > 237 K has a cell with $P2_1cn$ symmetry, and the nonpolar low-temperature phase in the region of T < 237 K is incommensurate [3]. The only ferroelectric phase with $P2_1cn$ (C_{2v}^9) crystal symmetry is characterized by a spontaneous polarization oriented in the *a* direction (*X* axis) [4].

The study was conducted on single crystals grown from solution. The samples had the form of rectangular bars with dimensions $3 \times 2.5 \times 5$ mm, the edges of which were oriented along the crystallographic axes (*X, Y, Z* coordinates) of the orthorhombic cell of the high-temperature phase. Silver paste electrodes were applied onto the sample faces perpendicular to the polar axis *a* (*X* axis). The dielectric permittivity ε was measured at a frequency of 1.6 kHz with the aid of a standard capacitive bridge, while the spontaneous polarization P_s was determined from the dielectric hysteresis loops (polarization P_a versus field strength E_a) measured at 50 Hz. In addition, the P_a value was monitored using the dielectric hysteresis loops measured by the electrometric technique in a strong quasistatic field; the measurements of ε_{aa} were performed with an additional constant polarizing electric field exceeding the coercive strength E_k. According to the electrometry data, application of electric field with a strength of E_k renders the sample crystal completely monodomain.

Observation of the aforementioned precautions during the experimental determination of ε_{aa} and P_a values (close to the true characteristics of monodomain crystals) is highly important for making correct conclusions about the reasons for giant changes in ε_{aa} and P_a. Indeed, these values could change both due to disappearance of the ferroelectric properties and as a result of an anomalous decrease in the mobility of domain walls in the applied field E_a (electric rigidity buildup) in the presence of uniaxial stresses.

Figure 1 shows the temperature variation of ε_{aa} and P_a observed in the region of existence of a ferroelectric phase for various compressive stresses σ_{zz}. As can be seen, an increase in the applied compressive stress σ_{zz} leads to a sharp drop in both ε_{aa} and P_a and is accompanied by narrowing of the temperature interval of existence of the polar phase.

Figure 2 shows variation of the P_a value as a function of the electric field for various applied stresses σ_{zz} in a polar phase of the crystal studied. As the σ_{zz} value grows, the dielectric hysteresis loop exhibits significant transformations, whereby the amplitude and width of the loop gradually decrease (Fig. 2a). At σ_{zz} > 10 kgf/cm^2, the loop degenerates into a straight line and the spontaneous polarization P_s virtually disappears (Fig. 2b).

It must be emphasized that the anomalously large changes in ε_{aa} and P_s are only observed for the uniaxial

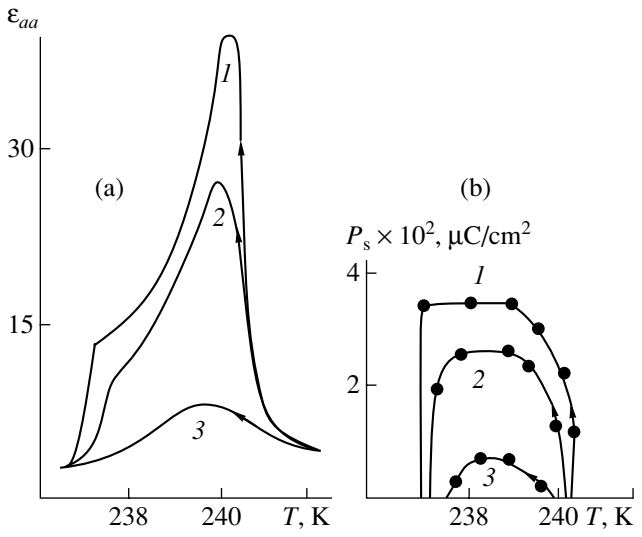

Fig. 1. Temperature dependences of the permittivity ε_{aa} and spontaneous polarization P_s of a TMA–$CuBr_4$ crystal uniaxially stressed to σ_{zz} = 0 (*1*), 4 (*2*), and 9 kgf/cm^2 (*3*).

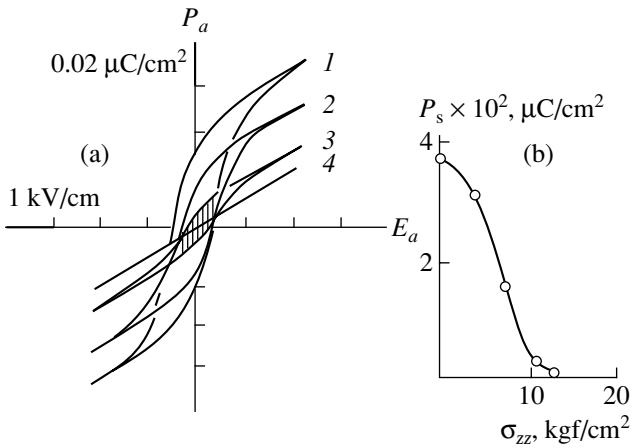

Fig. 2. The effect of uniaxial stress on the dielectric properties of a TMA–$CuBr_4$ crystal: (a) transformation of the dielectric hysteresis loop $P_a(E_a)$ under the action of uniaxial compressive stress σ_{zz} = 0 (*1*), 4 (*2*), 9 (*3*), and 12 kgf/cm^2 (*4*); (b) the plot of spontaneous polarization P_s versus applied stress σ_{zz} at T = 239 K.

σ_{zz} stresses. Application of σ_{xx} stresses ($X \parallel P_s$) leads only to small decrease in ε_{aa} and P_a, which is probably related to the usual piezoelectric effect (with a piezoelectric coefficient of $d_{111} = \Delta P_s/\sigma_{xx} = 2.5 \times 10^{-8}$ esu).

The observed changes in the dielectric properties are reversible: upon release of the σ_{zz} stress, all the dielectric characteristics are almost completely (to within 10%) restored on the initial level. The time of recovery of the equilibrium vales does not exceed 1 s.

The applied σ_{zz} stress (as well as a uniform pressure p) does not change the crystal symmetry either in the initial (high-temperature) *Pmcn* phase or in the polar $P2_1cn$ phase. According to group theory analysis, coefficients at invariant combinations of various quantities in the thermodynamic potential describing the sequence of phase transitions may depend on σ_{zz} (σ_{xx}, σ_{yy}). The fact that the polar phase is unstable with respect to small σ_{zz} stresses indicates that the crystal occurs in a state close to a triple critical point on the σ_{zz}–T diagram, at which the lines of three phases intersect [2].

It is especially important to note extremely large variations in the dielectric characteristics of the crystal in the whole range of existence of the polar phase in response to relatively small uniaxial compressive stresses. For example, upon application of a stress $\sigma_{zz} \geq$ 10 kgf/cm^2, the value of ε_{aa} decreases by a factor of 6–7 (Fig. 1a), while P_s drops from 0.04 μC/cm^2 to almost zero (Fig. 2). The coefficients characterizing the (average) sensitivity of these quantities with respect to the applied stress are $K_\varepsilon = (\Delta\varepsilon/\varepsilon)/\sigma_{zz} \approx 0.8$ cm^2/kgf and $D = \Delta P_s/\sigma_{zz} = 4 \times 10^{-3}$ μC/kgf = 4×10^{-10} C/N = 2×10^{-5} esu, respectively. The value of D is close to the maximum piezoelectric coefficients known in ferroelectric crystals. For example, the piezoelectric coefficient is 0.5×10^{-10} C/N for barium titanate, 0.02×10^{-10} C/N for quartz, 0.2×10^{-10} C/N for lithium niobate, 8×10^{-10} C/N for SbSJ, and 5×10^{-10} C/N for PZT ceramics [5]. Another interesting fact is that a small uniaxial stress produced by slightly pressing the crystal with a finger can change the crystal capacitance within almost one order of magnitude.

Thus, the results of our investigation demonstrate the possibility of controlling the structure and properties of crystals by applying small uniaxial pressures.

Acknowledgments. The authors are grateful to V. Pakhomov for kindly providing the crystals for investigation.

The experiments were performed using equipment of the Analytical Center of Collective Use at the Dagestan Scientific Center of the Russian Academy of Sciences. The study was supported by the Russian Foundation for Basic Research (project no. 00-05-72031) and by the Federal Targeted Program "Integration" (project no. 4.15-Ch0009(2002)).

REFERENCES

1. F. Jona and G. Shirane, *Ferroelectric Crystals* (Pergamon, Oxford, 1962; Mir, Moscow, 1965).
2. S. N. Kallaev, V. V. Gladkiĭ, V. A. Kirikov, *et al.*, Zh. Éksp. Teor. Fiz. **98** (5), 1804 (1990) [Sov. Phys. JETP **71**, 1013 (1990)].
3. K. Hasebe, H. Mashiyama, S. Tanisaki, and K. Gesi, J. Phys. Soc. Jpn. **51**, 1045 (1982).
4. K. Gesi, Ferroelectrics **66**, 269 (1986).
5. I. S. Rez and Yu. M. Poplavko, *Dielectrics* (Radio i Svyaz', Moscow, 1989), p. 287.

Translated by P. Pozdeev

Technical Physics Letters, Vol. 28, No. 9, 2002, pp. 773–775. Translated from Pis'ma v Zhurnal Tekhnicheskoĭ Fiziki, Vol. 28, No. 18, 2002, pp. 48–53.

Linear Relationship between Resistivity and Isobaric Thermal Strain of Nickel Above and Below the Curie Temperature

Zh. Kh. Murlieva, D. K. Palchaev, and E. D. Borzov

Dagestan State University, Makhachkala, Dagestan, Russia

e-mail: dairphalchaev@dgu.mail.ru

Received May 22, 2002

Abstract—Experimental results indicate a linear relationship between the resistivity and the isobaric thermal strain of nickel in a broad temperature range above and below the Curie temperature. It is demonstrated that the phonon and magnon contributions to the total resistivity of nickel can be effectively separated. Simple expressions are derived for estimation of the resistivity of metals of the iron group in the ferro- and paramagnetic state from data on the thermal expansion coefficient. © *2002 MAIK "Nauka/Interperiodica".*

As is known [1, 2], the total resistivity of ferromagnetic materials such as Fe, Co, and Ni represents a sum of contributions due to the scattering of electrons on phonons (ρ_{ph}), magnons (ρ_m), and static defects (ρ_s):

$$\rho = \rho_{ph} + \rho_m + \rho_s. \quad (1)$$

The value of ρ_s is virtually independent of temperature and can be determined by extrapolating ρ to 0 K. Below the Curie temperature (T_c), ρ_m (as well as ρ_{ph}) is a complicated function of temperature, while above T_c, ρ_m remains constant. The problem of separation of the phonon and magnon components of the total resistivity is usually solved [2] by estimating ρ_{ph} using the Bloch–Grüneisen interpolation formula. The accuracy of separation of these contributions is determined by the error of evaluation of the strain potential of the electron scattering on phonons [1].

According to [3], the strain potential of scattering can be presented in the general case as

$$P = P^{ij}u_{ij}, \quad (2)$$

where P^{ij} is the strain potential constant tensor and u_{ij} is the strain tensor. The values of P^{ij} are uniquely determined in the limit of $u_{ij} \cong 1$. For a crystal of cubic symmetry, this tensor reduces to a single constant P (the value of which is on the order of the atomic energy e^2/a_0), while the characteristic relaxation time in metals represents a value inverse to the Debye frequency: $\tau_t^* \cong \omega_D^{-1}$.

However, the theoretical interpretation of ρ_{ph} based on the concept of strain potential encounters two problems. The first problem is related to the impossibility of theoretically determining constant P and, hence, the need for using data of indirect experiments [3]. The second problem is related to the difficulty of making allowance for the inelastic character of the electron–phonon interaction [1–3].

In this paper, the experimental data are interpreted based on modern theoretical notions about electron scattering [1–3] and on an approach [4] employing a small set of experimentally determined parameters sufficient to formulate the required statement. Previously [5, 6], we empirically found a linear relationship between the phonon resistivity component and the isobaric thermal strain $(dV/dT)_p(T/V) = \beta T$ for a series of 25 nontransition metals:

$$\rho_{ph} = \rho^*\beta T, \quad (3)$$

where ρ^* is a constant quantity for a given metal and $\beta = (\alpha_1 + \alpha_2 + \alpha_3)$ is the volume thermal expansion coefficient. Based on this relation, it was demonstrated that the representation of u_{ij} in Eq. (2) through the tensor of thermal expansion coefficients α_{ij} may significantly simplify solving the above problems. Indeed, both u_{ij} and α_{ij} are symmetric tensors of the same nature, but data on the values of $\alpha = f(T)$ are more available in the literature. In addition, the α_{ij} tensor (in contrast to u_{ij}) is a differential characteristic of the thermal strain.

The empirical analog of Eq. (2) for an arbitrary equilibrium state can be written as [6]

$$P = P^*\beta T. \quad (4)$$

Here, the quantity P^* is uniquely determined [6] and represents, like P^{ij}, a constant on the order of the atomic energy. However, in contrast to P^{ij}, this quantity is independent of the lattice parameter. According to (4), the value of the relaxation time τ_{ex}^* for electrons in a metal in the limit $\beta T \cong 1$ is equal to the inverse frequency,

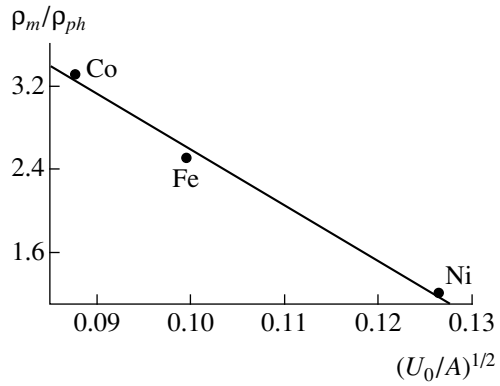

Correlation between the ratio of the magnon and phonon resistivity components ρ_m/ρ_{ph} and the ratio U_0/A of the interaction energies for metals of the iron group.

which agrees with the theory. The coincidence of P^* with P^{ij} and of τ^*_{ex} with τ^*_t is probably explained by the fact that the condition of locality of the potential is valid both in the limit of $u_{ij} \longrightarrow 1$ and for $\beta T \longrightarrow 1$.

The possibility of obtaining quantitative estimates of the phonon resistivity at any temperature using relation (3) from data on the isobaric thermal straining allows us, first, to estimate with greater precision the ρ_m component of the total resistivity and, second, to establish the effect of anharmonicity of atomic oscillations on the scattering of electrons on magnons.

For this purpose, we have measured the resistivity and the thermal expansion of pure nickel (99.99% Ni) in one experiment in the temperature interval from 300 to 1000 K. The resistivity ρ was measured by the four-point-probe technique for a sample placed into a quartz dilatometer. The temperature difference across the sample length ($l \sim 58$ mm, $d \sim 4.5$ mm) did not exceed 2 K. Our data on ρ and α values agree well with the published data [8–10] for the temperature interval studied. Variation of the total resistivity of the nickel sample below and above T_c is approximated by the formulas

$$\rho = -2.7 \times 10^{-8} + 8.92 \times 10^{-6}\beta T \quad (300\text{–}633\ \text{K})\ T < T_c, \tag{5}$$

$$\rho = 21.875 \times 10^{-8} + 3.47 \times 10^{-6}\beta T \quad (633\text{–}1000\ \text{K})\ T > T_c \tag{6}$$

with a correlation coefficient of 0.999. The negative value of the free term in formula (5) has no physical meaning; this parameter was obtained by extrapolating ρ from the temperature interval of 633 $\longrightarrow$ 300 K, in which the resistivity exhibits a sharp drop due to magnetostriction. Apparently, the free term in formula (5) includes a constant magnon contribution to the scattering [2].

The slopes of expressions (5) and (6) indicate theoretical limits of the resistivity characteristic of the scattering on phonons (ρ^*_{ph}) [6] above T_c and on phonons + magnons (ρ^*_{mph}) below T_c. According to the theory [3], these values are determined by the constants of the strain potential of scattering for the para- and ferromagnetic states. The characteristic resistivities are inversely proportional to the corresponding relaxation times:

$$\rho^*_{ph} \sim \frac{1}{\tau^*_{ph}} \sim \nu_D \sim \sqrt{U_0},$$

$$\rho^*_{mph} \sim \frac{1}{\tau^*_{ph}} + \frac{1}{\tau^*_m} \sim \nu_D + \nu_m \sim \sqrt{U_0} + \sqrt{A}, \tag{7}$$

where ν_D is the Debye frequency and $\nu_m = k_B T_c/h$ [2] is the characteristic frequency of the exchange interaction. These frequencies are proportional to the energy of interatomic interaction in the paramagnetic state (U_0) and the exchange interaction energy (A), respectively. This is indirectly confirmed by a correlation between the ratio ρ_m/ρ_{ph} (by data from [9]) at T_c and the ratios $(U_0/A)^{1/2}$ observed for metals of the iron group (see figure).

Based on the above considerations, ρ^*_{mph} can be calculated by the formula

$$\rho^*_{mph} = k(\nu_D + \nu_m), \tag{8}$$

where k is a constant (the same for para- and ferromagnetic states), which can be estimated by comparing the slope of expression (6) to the value obtained from the relation $\rho_{ph} = k\nu_D$. The calculation of ρ^*_{mph} by formula (8) yields $8.8 \times 10^{-6}\ \Omega$ m, which agrees well with the value $8.92 \times 10^{-6}\ \Omega$ m obtained by formula (5). The fact that this coincidence is not accidental is confirmed by the results of analogous calculations for iron and cobalt. According to (8), ρ^*_{mph} for Fe and Co are 1.33×10^{-5} and $1.53 \times 10^{-5}\ \Omega$ m, respectively, in agreement with the estimates obtained from the experimental data on ρ and α [8–11] in the ferromagnetic state: $1.5 \times 10^{-5}\ \Omega$ m (for Fe) and $1.63 \times 10^{-5}\ \Omega$ m (for Co). In these calculations, we employed the same value of constant k as above (for Ni), since these metals possess the same valence and exhibit close values of the atomic densities.

Using the expression

$$\rho_{ph} + \rho_m = 3.95 \times 10^{-19}(\nu_D + \nu_m)\beta T, \tag{9}$$

we can calculate the temperature dependence of the resistivity components due to electron scattering on phonons and magnons for the three metals under consideration, proceeding from data on the thermal expansion coefficients at the corresponding temperatures. For temperatures above T_c, formula (9) transforms into

$$\rho(T) = 3.95 \times 10^{-19}\nu_m\beta_c T_c + 3.95 \times 10^{-19}\nu_D\beta T, \tag{10}$$

which is fully consistent with the aforementioned notion about constant magnon contribution to the resistivity in the paramagnetic state.

The constancy of the ratio of the thermal expansion coefficient to the heat capacity (Grüneisen law) indicates that the term βT reflects both the thermal strain and the thermal contribution due to increasing temperature, which, according to [12], determines the temperature dependence of the resistivity in metals.

Thus, we may conclude that the isobaric thermal strain is a determining parameter characterizing the scattering of electrons on both phonons and magnons. There is a linear relationship between the total resistivity of nickel in a broad range of temperatures both above and below T_c and the isobaric thermal strain.

The role of anharmonicity in the formation of the magnon resistivity component is the same as that of the phonon component in the temperature interval from $T_D/2$ to T_c. For all metals of the iron group, the characteristic magnon resistivity is determined by the frequency of the exchange interaction. Additivity of the characteristic resistivity contributions in the ferromagnetic phase allows the phonon and magnon components of the electron scattering T to be effectively separated using data on the isobaric thermal strain.

REFERENCES

1. J. M. Ziman, *Electrons and Phonons* (Clarendon, Oxford, 1960; Inostrannaya Literatura, Moscow, 1962).
2. S. V. Vonsovskiĭ, *Magnetism* (Nauka, Moscow, 1971; Wiley, New York, 1974).
3. V. F. Gantmakher and Y. B. Levinson, *Carrier Scattering in Metals and Semiconductors* (Nauka, Moscow, 1984; North-Holland, New York, 1987).
4. V. M. Zverev and V. P. Silin, Pis'ma Zh. Éksp. Teor. Fiz. **64** (1), 33 (1996) [JETP Lett. **64**, 37 (1996)].
5. B. P. Pashaev and D. K. Palchaev, Inzh.-Fiz. Zh. **41** (4), 717 (1981).
6. D. K. Palchaev, Doctoral Dissertation in Physics and Mathematics (Makhachkala, 1999).
7. J. F. Nye, *Physical Properties of Crystals: Their Representation by Tensors and Matrices* (Clarendon, Oxford, 1964; Mir, Moscow, 1967).
8. S. I. Novikova, *Thermal Expansion of Solids* (Nauka, Moscow, 1974).
9. V. E. Zinov'ev, *Thermophysical Properties of Metals at High Temperatures* (Metallurgiya, Moscow, 1989).
10. L. N. Larikov and Yu. F. Yurchenko, *Structure and Properties of Metals and Alloys: A Handbook* (Naukova Dumka, Kiev, 1985).
11. O. A. Shmatko and Yu. V. Usov, *Electrical and Magnetic Properties of Metals and Alloys: A Handbook* (Naukova Dumka, Kiev, 1987).
12. R. A. Suris and V. Ya. Frenkel', Usp. Fiz. Nauk **164** (4), 379 (1994) [Phys. Usp. **37**, 357 (1994)].

Translated by P. Pozdeev

Technical Physics Letters, Vol. 28, No. 9, 2002, pp. 776–778. Translated from Pis'ma v Zhurnal Tekhnicheskoĭ Fiziki, Vol. 28, No. 18, 2002, pp. 54–60.

The Explosive Oxidation of Hydrocarbons in a Supercritical Water

A. A. Vostrikov and S. A. Psarov

Kutateladze Institute of Thermal Physics, Siberian Division, Russian Academy of Sciences, Novosibirsk, Russia

e-mail: vostrikov@itp.nsc.ru

Received April 9, 2002

Abstract—The kinetics of oxidation of naphthalene and a heavy oil residue (upon vacuum distillation) by oxygen dissolved in supercritical water is studied in a wide range of temperatures (663 K ≤ T ≤ 1075 K) and pressures (31 MPa ≤ P ≤ 67 MPa). It is established that the oxidation process exhibits an explosive (blow-up) character. The kinetic constants characterizing the thermal explosion are determined. For naphthalene, the heat evolution rate during the explosive oxidation obeys the law $W_N = 10^{13.10 \pm 0.30}\exp((170.4 \pm 1.0\ \text{kJ/mol})/RT) \times [C_{10}H_8]^{0.46 \pm 0.01}[O_2]^{0.63 \pm 0.01}[H_2O]^{1.66 \pm 0.03}$ kJ/(l s). © *2002 MAIK "Nauka/Interperiodica".*

The oxidation of organic matter (OM) in water at supercritical temperatures (T > 647 K) and pressures (P > 22.1 MPa) has been extensively studied in the past decade [1–6]. This interest is related to the fact that supercritical water (SCW) is capable of dissolving unlimited amounts of both OM and oxygen. For example, SCW at T = 693 K and P = 30 MPa possesses a static permittivity of 8 [7] and a density of ρ = 0.2 g/cm^3 [8]. Therefore, the oxidation processes in SCW are characterized by a high rate of collisions between reagents and proceed by a free-radical mechanism. The total or partial oxidation of OM is conducted, as a rule, at 775 K ≤ T ≤ 900 K and 25 MPa ≤ P ≤ 38 MPa [1–6]. Under these relatively low temperatures, no harmful oxides are formed, while heteroatoms such as chlorine, sulfur, and phosphorus are converted into inorganic compounds.

Previously [6], it was established that adding O_2 into a solution of HOR (a heavy oil residue fraction upon vacuum distillation) or naphthalene in SCW led to the ejection of substance from a reactor, which was caused by a sharp jump of the solution temperature and pressure in the reactor.

In this study, we measured for the first time the kinetics of the explosive (blow-up) oxidation of naphthalene and HOR in SCW with O_2 and determined the kinetic constants of this process. During the experiment, the pressure in the reactor was continuously monitored before and after injection of a fuel (naphthalene or HOR) into SCW with O_2. The reactor was preliminarily charged with the necessary amount of water and O_2, heated to a preset temperature, and maintained at this temperature. The fuel was injected via a piston valve at $T \approx 500$ K and P = 70 MPa in the form of a stream parallel to the reactor axis. The reactor, made of stainless steel, had a channel with a diameter of 10 mm and a volume of 10.3 cm^3. The pressure was measured by a pressure strain gauge.

Preliminary experiments showed that the temperature dependences of the partial pressure P_a of SCW containing the additives of fuel, O_2, and CO_2 in concentrations within the interval studied coincided with tabulated data for water [8]. Therefore, measuring the time variation of the total pressure, $P(t)$, and subtracting the partial pressures of reagents, we obtained the function $P_a(t)$. Then, using these $P_a(t)$ values and the tabulated data [8], we determined the time variation of the temperature $T(t)$ and the enthalpy increment $\Delta H(t)$. These curves are presented in Figs. 1 and 2, where vertical arrows indicate the moment of fuel injection. Initial compositions of the reaction mixtures are given in the table.

The behavior of pressure $P(t)$, temperature $T(t)$, and enthalpy $\Delta H(t)$ presented in Figs. 1 and 2 is determined by a thermal balance between the heat $H_c(t)$ evolved as a result of fuel oxidation and the heat lost through the reactor walls $H_r(t)$. To the right of the $\Delta H(t)$ peak, no heat is evolved (H_c = 0) and, hence, $H_r(t) = -\Delta H(t)$. Using this relation, we determined $H_c(t)$ and calculated the heat evolution rate $W(t) = dH_c/dt$ in each experiment. The $W(t)$ curves are also depicted in Figs. 1 and 2.

As can be seen from the kinetic curves in Figs. 1 and 2, the process of bulk fuel oxidation in SCW exhibits an explosive character. A more involved shape of the $W_{HOR}(t)$ profile is explained by the more complex composition of this fuel. Apparently, various HOR components are characterized by different oxidation rates. In addition, heavier components may dissolve slower in SCW. An analysis of the products of fuel pyrolysis in SCW [5, 6] showed that naphthalene does not decom-

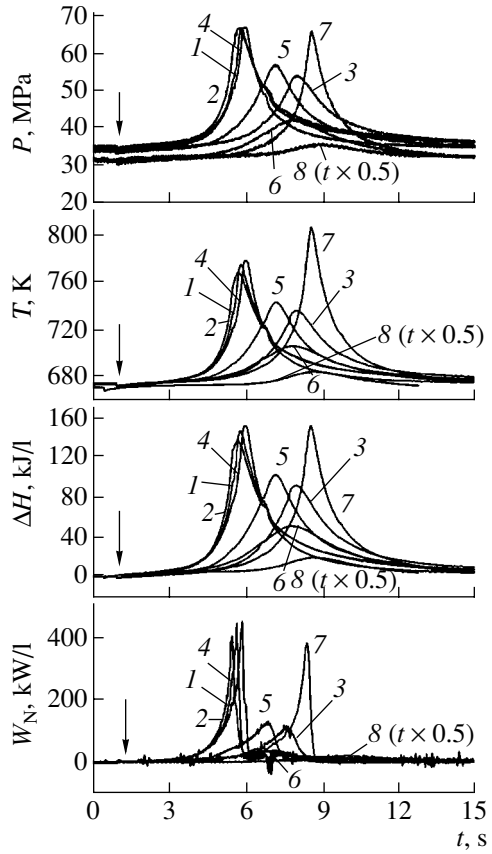

Fig. 1. Time variation of total pressure *P*, temperature *T*, enthalpy increment ΔH, and heat evolution rate W_N during the explosive oxidation of naphthalene by oxygen in supercritical water. For curve *8*, the time scale is compressed by a factor of 2. The initial concentrations of reagents for each curve are given in the table.

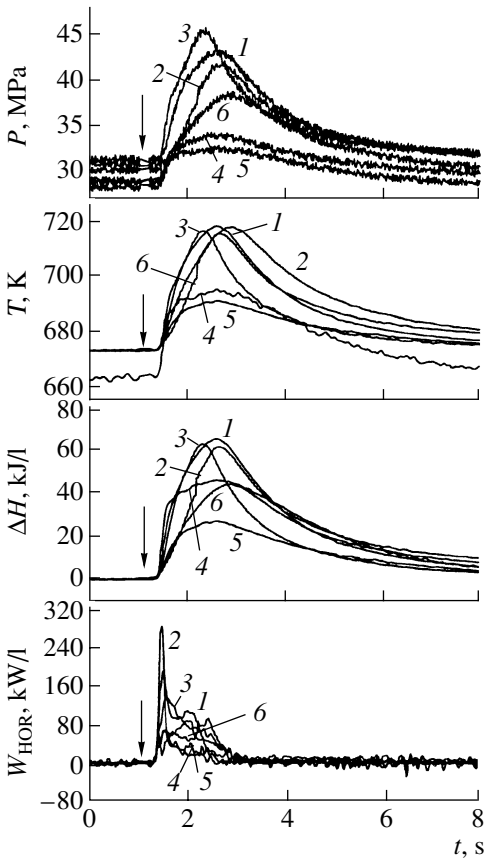

Fig. 2. Time variation of total pressure *P*, temperature *T*, enthalpy increment ΔH, and heat evolution rate W_{HOR} during the explosive oxidation of a heavy oil residue by oxygen in supercritical water. The initial concentrations of reagents for each curve are given in the table.

pose at $T < 875$ K, while HOR exhibits partial decomposition. Therefore, the explosive oxidation of HOR is probably accompanied by pyrolysis. Note also that, at $T > 875$ K, oxygen of water molecules can also participate in the oxidation process [4, 5].

Assuming validity of the Arrhenius relationship for the oxidation rate constant, the dependence of *W* on the temperature *T* and reagent concentrations can be presented in the following form [9]:

$$W = A\exp(-E/RT) f^{\alpha} o^{\beta} a^{\gamma}. \quad (1)$$

Here, *R* is the universal gas constant and *f*, *o*, and *a* are the concentrations of fuel, oxygen, and H_2O (expressed in [mol/l]). All parameters entering (1), including the preexponential (dimensional) factor *A*, the activation

Initial conditions for the explosive oxidation of hydrocarbons by oxygen in supercritical water

Reagent	Initial concentration, mol/l							
	1	2	3	4	5	6	7	8
$C_{10}H_8$	0.118	0.092	0.053	0.145	0.092	0.152	0.092	0.092
O_2	0.855	0.833	0.777	0.757	0.573	0.249	0.922	0.097
H_2O	19.95	19.95	19.95	19.95	19.95	19.95	16.18	16.18
HOR ($C_{100}H_{143}$)	0.0051	0.0032	0.0173	0.0051	0.0173	0.0051		
O_2	0.339	0.320	0.291	0.206	0.242	0.272		
H_2O	19.95	19.95	19.95	19.95	18.87	13.48		

Note: The number of experiment with naphthalene and HOR corresponds to the curve number in Figs. 1 and 2, respectively.

energy E, and the empirical constants α, β, and γ, were determined by least squares using the experimental values of W, T, f, o, and a measured as functions of time at a step of 1 ms. The current concentrations f, o, and a were determined by the formula

$$x(t) = x_0 - \nu q^{-1} H_c(t), \quad (2)$$

where $x(t)$ and x_0 are the current and initial reagent concentrations; ν is the stoichiometric coefficient of a given reagent in the reaction of total oxidation of a particular fuel; and q is the specific combustion heat of this fuel. For water, the sign at the second term in the right-hand part of Eq. (2) should be changed from minus to plus. For naphthalene, q_N = 5020 kJ/mol [10]. For HOR, the q_{HOR} value was determined by the Mendeleev formula, assuming that this fraction consists of $C_{100}H_{143}$ molecules (with the C/H atomic ratio corresponding to that in our HOR sample); this yielded q_{HOR} = 53200 kJ/mol. Note that the conditional representation of HOR as composed of $C_{100}H_{143}$ molecules does not influence the results and conclusions of our study, since the q values calculated for large molecules by the Mendeleev formula depend only on the C/H ratio. According to this model, the combustion of HOR corresponds to the reaction $C_{100}H_{143} + 135.25O_2 = 100CO_2 + 71.25H_2O$, from which it follows that ν_o = 135.25 and ν_a = 71.5. By the same token, the oxidation of naphthalene corresponds to $C_{10}H_8 + 12O_2 = 10CO_2 + 4H_2O$, from which it follows that ν_o = 12 and ν_a = 4. It is important to note that, in the case of a partial oxidation of naphthalene, no hydrocarbons other than $C_{10}H_8$ were present in the reaction products [5]. This implies that, after the first chemical contact of $C_{10}H_8$ and O_2, the subsequent oxidation of the molecular residue proceeds very rapidly. As can be seen from the reaction equations, the amount of reagents did not significantly vary in the course of oxidation. Therefore, the method of data processing based on calculations of the $P_a(t)$ kinetics does not lead to uncertainties exceeding the experimental error of pressure measurements (0.25%).

Calculations performed as described above led to the following empirical formula for the oxidation rate of naphthalene:

$$W_N = 10^{13.10 \pm 0.30} \exp((170.4 \pm 1.0 \text{ kJ/mol})/RT) \times f^{0.46 \pm 0.01} o^{0.63 \pm 0.01} a^{1.66 \pm 0.03} \text{ kJ/(l s)}.$$

For the oxidation of HOR, the $W_{HOR}(t)$ value in the region of a sharp buildup to the first maximum (see Fig. 2) is described by the formula

$$W_{HOR} = 10^{16.03 \pm 0.20} \exp((178.0 \pm 0.8 \text{ kJ/mol})/RT) \times f^{0.68 \pm 0.04} o^{0.12 \pm 0.02} a^{0.65 \pm 0.10} \text{ kJ/(l s)}.$$

A high rate of the bulk oxidation of HOR in SCW, which can be conducted without the formation of soot [11], opens wide possibilities for the practical use of SCW in the ecologically safe power production. The existing steam generators with furnaces can be replaced by reactors employing SCW. The combustion of fuel immediately in SCW eliminates the formation of harmful oxides and low-volatile, sulfur-containing compounds [11] because of a relatively low process temperature, decreases specific heat losses, and reduces specific metal consumption in boilers of the SCW reactor type.

It should be also pointed out that the conditions studied in our experiments can be realized in nature, in particular, in oil deposits. The presence of water layers below oil and supercritical pressures are usual factors for oil deposits [12]. The temperature in such water layers can increase to a supercritical level as a result of hot magma, SCW, and O_2 breakdown, as well as due to oxidation processes occurring at the water–oil interphase boundary. A potential source of O_2 is offered by water and some metal oxides. The resulting explosive oxidation of oil may lead to microscopic, local, or global consequences, depending on the amount of reagents. At present, our experiments modeling such processes are in progress.

Acknowledgments. The authors are grateful to L.I. Kurkina and D.Yu. Dubov for fruitful discussions.

This study was supported by the Russian Foundation for Basic Research (project no. 01-02-17372) and by the Ministry of Education of the Russian Federation (project no. ZN-119-01).

REFERENCES

1. T. D. Thornton and Ph. E. Savage, AIChE J. **38** (3), 321 (1992).
2. Ph. E. Savage, Chem. Rev. **99** (2), 603 (1999).
3. J. L. DiNaro, J. W. Tester, J. B. Howard, *et al.*, AIChE J. **46** (11), 2274 (2000).
4. A. A. Vostrikov, D. Yu. Dubov, and S. A. Psarov, Izv. Akad. Nauk, Ser. Khim. **8**, 1406 (2001).
5. A. A. Vostrikov, D. Yu. Dubov, and S. A. Psarov, Izv. Akad. Nauk, Ser. Khim. **8**, 1409 (2001).
6. A. A. Vostrikov, D. Yu. Dubov, and S. A. Psarov, Pis'ma Zh. Tekh. Fiz. **27** (20), 7 (2001) [Tech. Phys. Lett. **27**, 847 (2001)].
7. *Emering Thechnologies in Hazardous Waste Management III*, Ed. by D. W. Tedder and F. G. Pohland (American Chemical Society, Washington, 1993), ACS Symp. Ser., Vol. 518, pp. 35–76.
8. A. A. Aleksandrov and B. A. Grigor'ev, *Tables of Thermophysical Properties of Water and Water Vapor: a Handbook* (Mosk. Énerg. Inst., Moscow, 1999).
9. L. N. Khitrin, *Physics of Combustion and Explosion* (Mosk. Gos. Univ., Moscow, 1957).
10. *Physicochemical Properties of Individual Hydrocarbons*, Ed. by V. M. Tatevskiĭ (Gostoptekhizdat, Moscow, 1960).
11. A. A. Vostrikov, D. Yu. Dubov, and S. A. Psarov, in *Chemistry of Petroleum and Gas* ("STT," Tomsk, 2000), Vol. 2, pp. 492–496.
12. J. M. Hunt, *Petroleum Geochemistry and Geology* (W. H. Freeman, San Francisco, 1979; Mir, Moscow, 1982).

Translated by P. Pozdeev

Technical Physics Letters, Vol. 28, No. 9, 2002, pp. 779–781. Translated from Pis'ma v Zhurnal Tekhnicheskoĭ Fiziki, Vol. 28, No. 18, 2002, pp. 61–66.

The Effect of Percolation Conductivity on the Characteristics of Relaxation Polarization Processes

A. S. Bogatin, I. V. Lisitsa, and S. A. Bogatina

Rostov State University, Rostov-on-Don, Russia

e-mail: bogatin@phys.rsu.ru

Received April 11, 2002

Abstract—The use of ε" and $\tan\delta$ as characteristics of the relaxation processes under conditions of high conductivity is discussed. Conditions under which the maxima of $\tan\delta$ do not vanish are found. It is concluded that $\tan\delta$ is expediently used for description of the relaxation polarization processes. A method of quantitative evaluation of the intensity of relation processes is proposed. *© 2002 MAIK "Nauka/Interperiodica".*

The process of relaxation polarization can be described in terms of the Debye equation, which, being originally derived for the dipole orientation polarization, has proved to be applicable to some other relaxation processes as well. This equation describes the dependence of the real (ε') and imaginary (ε") parts of the complex permittivity $\varepsilon = \varepsilon' - i\varepsilon''$ of a medium on the frequency ω of an applied electric field and on the relaxation time τ:

$$\varepsilon' = \varepsilon_\infty + \frac{\Delta\varepsilon}{1+\omega^2\tau^2}; \quad \varepsilon'' = \frac{\Delta\varepsilon\omega\tau}{1+\omega^2\tau^2}. \qquad (1)$$

Here, $\Delta\varepsilon = \varepsilon_c - \varepsilon_\infty$, ε_c and ε_∞ are the values of ε' at low ($\omega \ll 1/\tau$) and high ($\omega \gg 1/\tau$) frequencies, respectively; ε_0 will denote the dielectric constant [1].

The Debye equation implies the absence of percolation conductivity in the medium under consideration. In the presence of such processes, this equation has to be transformed as follows:

$$\varepsilon' = \varepsilon_\infty + \frac{\Delta\varepsilon}{1+\omega^2\tau^2}; \quad \varepsilon'' = \frac{\sigma}{\varepsilon_0\omega} + \frac{\Delta\varepsilon\omega\tau}{1+\omega^2\tau^2}, \qquad (2)$$

where σ is the low-frequency conductivity. In this form, the Debye equation can be applied to description of the relaxation polarization processes, for example, of the Maxwell–Wagner (interlayer) type [2].

The relaxation time τ is the only microscopic parameter of the relaxation polarization process which can be directly determined in experiment, for example, from the ε"(ω) curve. Indeed, the frequency dependence of ε" exhibits a maximum. In the absence of percolation conductivity, $\tau\omega_{m1} = 1$ (where ω_{m1} is the frequency at which the maximum of ε" is observed). In the presence of percolation, the extrema of ε"(ω) are determined from the equation

$$\omega_{m1}^4\tau^3(\sigma\tau + \Delta\varepsilon\varepsilon_0) - \omega_{m1}^2\tau(\Delta\varepsilon\varepsilon_0 - 2\sigma\tau) + \sigma = 0. \qquad (3)$$

The greater positive root of this equation corresponds to a maximum in the frequency dependence of ε", while the smaller root corresponds to a minimum of this function. As the value of σ increases, the frequency of the minimum grows, while that of the maximum drops and the relative maximum height decreases. For

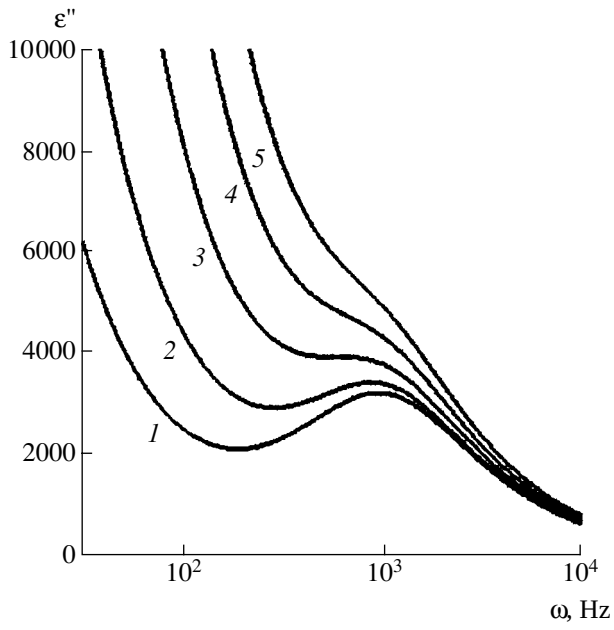

Fig. 1. Plots of the imaginary part of the complex permittivity versus frequency (logarithmic scale) of the applied electric field for $\tau = 10^{-3}$ s, $\varepsilon_\infty = 1000$, $\Delta\varepsilon = 6000$, and $\sigma = \sigma_1/4$ (*1*), $\sigma_1/2$ (*2*), σ_1 (*3*), $1.7\sigma_1$ (*4*), and $2.5\sigma_1$ (*5*).

1063-7850/02/2809-0779$22.00 © 2002 MAIK "Nauka/Interperiodica"

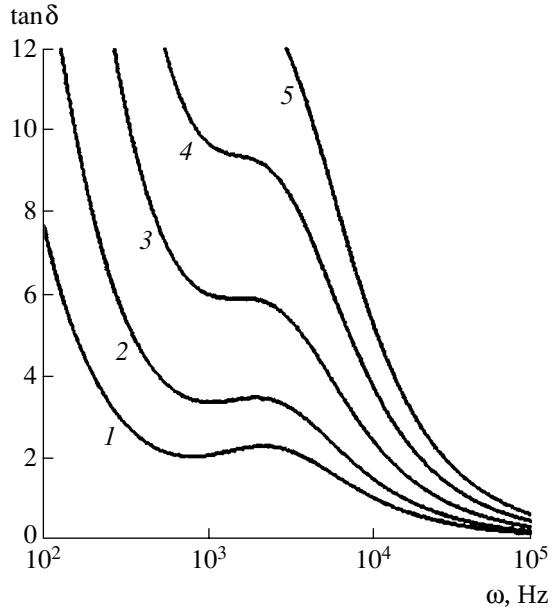

Fig. 2. Plots of the dielectric loss tangent versus frequency (logarithmic scale) of the applied electric field for $\tau = 10^{-3}$ s, $\varepsilon_\infty = 1000$, $\Delta\varepsilon = 6000$, and $\sigma = \sigma_2/4$ (*1*), $\sigma_2/2$ (*2*), σ_2 (*3*), $1.7\sigma_2$ (*4*), and $2.5\sigma_2$ (*5*).

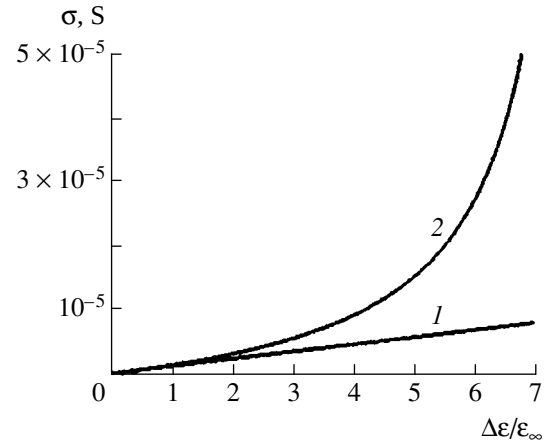

Fig. 3. Plots of the low-frequency conductivity versus $\Delta\varepsilon/\varepsilon_\infty$ ratio for $\tau = 10^{-3}$ s, $\varepsilon_\infty = 1000$, and $\sigma = \sigma_1$ (*1*) and σ_2 (*2*).

$\sigma = \sigma_1 = \varepsilon_0(\Delta\varepsilon)/(8\tau)$, the two roots coincide and the $\varepsilon''(\omega)$ curve exhibits an inflection point. When $\sigma > \sigma_1$, the function $\varepsilon''(\omega)$ exhibits no extrema (Fig. 1).

The relaxation time τ can be also estimated from the frequency dependence of $\tan\delta = \varepsilon''/\varepsilon'$. For $\sigma = 0$, the frequency corresponding to the maximum of $\tan(\omega)$ is

$$\omega_{m2} = \frac{1}{\tau}\sqrt{\frac{\varepsilon_\infty + \Delta\varepsilon}{\varepsilon_\infty}}. \quad (4)$$

In the absence of percolation conductivity, the ω_{m2} value is determined from the equation

$$\omega_{m2}^4\varepsilon_0\varepsilon_\infty\tau^3(\sigma\tau + \varepsilon_0(\Delta\varepsilon)) - \omega_{m2}^2\varepsilon_0\tau(\sigma\tau(\Delta\varepsilon) + \varepsilon_0\varepsilon_\infty(\Delta\varepsilon) + \varepsilon(\Delta\varepsilon)^2 - 2\sigma\varepsilon_\infty\tau) + \varepsilon_0\sigma((\Delta\varepsilon) + \varepsilon_\infty) = 0. \quad (5)$$

The shape of the frequency dependence of $\tan\delta$ resembles the shape of $\varepsilon(\omega)$ only for small $\Delta\varepsilon$. The above equation for ω_{m2} may possess either two positive roots (negative roots have no physical meaning) or no real roots at all. In the former case, the smaller root corresponds to a minimum in the frequency dependence of $\tan\delta(\omega)$, while the greater root corresponds to a maximum. The discriminant D of Eq. (5) for ω_{m2} can be written as

$$\frac{D}{\varepsilon_0^2\tau^2(\Delta\varepsilon)} = \sigma^2\tau^2((\Delta\varepsilon) - 8\varepsilon_\infty) - \sigma\tau(6(\Delta\varepsilon)\varepsilon_0\varepsilon_\infty - 2(\Delta\varepsilon)^2\varepsilon_0 + 8\varepsilon_\infty^2\varepsilon_0) + (\varepsilon_0^2\varepsilon_\infty^2(\Delta\varepsilon) + 2\varepsilon_0^2\varepsilon_\infty(\Delta\varepsilon)^2 + \varepsilon_0^2(\Delta\varepsilon)^3). \quad (6)$$

For $\Delta\varepsilon < 8\varepsilon_\infty$, the sign of this expression depends on the ratio $\sigma/\varepsilon_\infty$. Equating the discriminant D to zero, we obtain a square equation with respect to the product $\sigma\tau$. The roots of this equation are as follows:

$$(\sigma\tau)_1 = \frac{\varepsilon_0\varepsilon_\infty(\Delta\varepsilon) + (\Delta\varepsilon)^2\varepsilon_0}{8\varepsilon_\infty - (\Delta\varepsilon)}, \quad (7)$$

$$(\sigma\tau)_2 = \frac{\varepsilon_0(7\varepsilon_\infty(\Delta\varepsilon) + 8\varepsilon_\infty^2 - (\Delta\varepsilon)^2)}{(\Delta\varepsilon) - 8\varepsilon_\infty}. \quad (8)$$

The former root has a physical sense at $\Delta\varepsilon < 8\varepsilon_\infty$, this situation being conditionally referred to as the "weak relaxation process." In this case, the maxima of $\tan(\omega)$ vanish when $\sigma > \sigma_2 = (\varepsilon_0\varepsilon_\infty(\Delta\varepsilon) + (\Delta\varepsilon)^2\varepsilon_0)/((8\varepsilon_\infty - (\Delta\varepsilon))\tau)$ (Fig. 2). Comparing the values of σ_1 and σ_2, one can readily see that σ_2 is always greater than σ_1 (Fig. 3), which implies that the maximum of $\tan\delta(\omega)$ vanishes at greater σ than does the maximum of $\varepsilon''(\omega)$. The difference between σ_1 and σ_2 increases with the value of $\Delta\varepsilon$, that is, with the degree of manifestation of the relaxation polarization. This difference grows sharply when $\Delta\varepsilon$ approaches $8\varepsilon_\infty$.

For $\Delta\varepsilon > 8\varepsilon_\infty$, the discriminant D becomes a strictly positive quantity and never changes sign (irrespective of σ). In this case, referred to as the "strong relaxation process" ($\Delta\varepsilon > 8\varepsilon_\infty$), a maximum in $\tan(\omega)$ is present for any value of σ. This important circumstance was given no attention in [3]. At the same time, the maxima in the frequency dependence of ε'' vanish for $\sigma > \sigma_1$. Thus, taking into account the above considerations, we may ascertain that, for a medium with high conductiv-

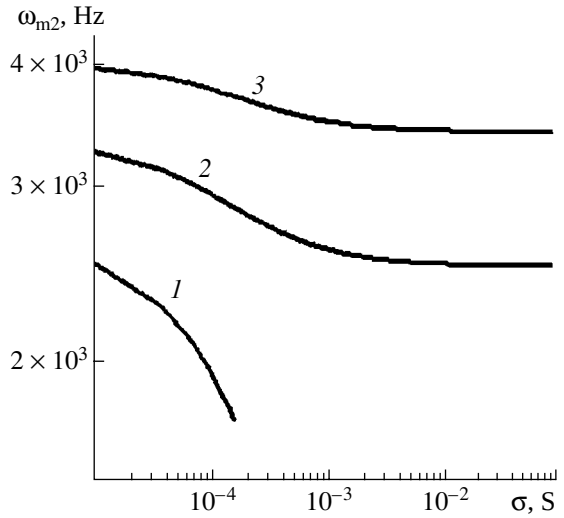

Fig. 4. Plots of the frequency corresponding to the maximum of $\tan\delta(\omega)$ versus low-frequency conductivity (logarithmic scale) for $\tau = 10^{-3}$ s, $\varepsilon_\infty = 1000$, $\Delta\varepsilon = 6000$, and $\Delta\varepsilon/\varepsilon_\infty = 6$ (*1*), 10 (*2*), and 15 (*3*).

ity, $\tan\delta$ is a more "sensitive" characteristic of the relaxation polarization process as compared to ε''.

It is interesting to consider variation of the frequency position of the maximum of $\tan\delta$ depending on σ. For $\Delta\varepsilon < 8\varepsilon_\infty$, this dependence is described in [1]. When σ increases, the frequency corresponding to the maximum of $\tan\delta$ drops. At $\sigma = \sigma_2$, the positions of maximum and minimum of $\tan\delta$ coincide and, as σ increases further, the maximum vanishes. A different behavior is observed in the case of $\Delta\varepsilon > 8\varepsilon_\infty$, where initially the maximum also shifts toward smaller frequencies with increasing σ. However, the shift gradually decreases and almost ceases, whereby the maximum does not change position irrespective of the further growth of σ (Fig. 4). In the region of σ, where the shift of the maximum in $\tan(\omega)$ takes place, it is more pronounced for greater $\Delta\varepsilon/\varepsilon_\infty$ ratios.

REFERENCES

1. H. Fröhlich, *Theory of Dielectrics: Dielectric Constant and Dielectric Loss* (Clarendon, Oxford, 1958; Inostrannaya Literatura, Moscow, 1960).
2. N. P. Bogoroditskiĭ, Yu. M. Volokovinskiĭ, and A. A. Vorob'ev, *Theory of Dielectrics* (Énergiya, Moscow, 1965).
3. G. I. Berdov, Izv. Vyssh. Uchebn. Zaved., Fiz., No. 3, 9 (1962).

Translated by P. Pozdeev

Technical Physics Letters, Vol. 28, No. 9, 2002, pp. 782–783. Translated from Pis'ma v Zhurnal Tekhnicheskoĭ Fiziki, Vol. 28, No. 18, 2002, pp. 67–71.

Differential Conductivity under Conditions of Transverse Runaway of Hot Electrons in Arbitrarily Oriented Electric and Magnetic Fields

Z. S. Kachlishvili, N. K. Metreveli, and F. G. Chumburidze

Tbilisi State University, Tbilisi, Georgia

e-mail: nanametreveli@yahoo.com; faculty@tsi.ge

Received February 11, 2002; in final form, May 15, 2002

Abstract—Behavior of the differential conductivity under conditions of the transverse runaway (TR) of hot electrons is studied in the quasielastic scattering approximation in the presence of a magnetic field oriented at an angle to the electric field. It is shown that the differential conductivity changes sign under the TR conditions in any classical magnetic field, while the current–voltage characteristic may acquire an S- or N-like shape, depending on whether the magnetic field is weak or strong. *© 2002 MAIK "Nauka/Interperiodica".*

The runaway of hot electrons always poses the question as to whether a given system remains in a stationary state [1]. In order to answer this question, it is necessary to study behavior of the differential conductivity. While there is no general relationship between the runaway of electrons and the differential conductivity, we demonstrated that the transverse runaway (TR) presents an exception and studied the differential conductivity in mutually perpendicular electric and magnetic fields [1]. However, according to our previous results [2, 3], TR also takes place when the magnetic field is oriented at an arbitrary angle to the electric field. This naturally poses a problem of studying the conditions for this state to remain stationary.

In the general case, the electron distribution function in the quasielastic scattering approximation depends on the resulting internal field strength (E^2) and on the angle β between **E** and **H**:

$$f_0 = \exp\left\{-\int \frac{dx}{1+\alpha\theta(x)}\right\}, \quad (1)$$

$$\theta(x) = x^{\frac{t+s}{2}} \frac{1+\eta x'\cos\beta}{1+\eta x'}, \quad (2)$$

where $x = \varepsilon/k_0T$, $\alpha = (E/E_0)^2$, $\eta = (H/H_0)^2$, $E_0 = \sqrt{3}\dfrac{k_0T}{e(l_0l_0)^{1/2}}$, $H_0 = \dfrac{(2mc^2k_0T)^{1/2}}{el_0}$, $l = l_0x^{\frac{t+1}{2}}$, $\tilde{l} = \tilde{l}_0x^{\frac{s+1}{2}}$, m is the effective electron mass, c is the speed of light, and t and s are the exponents in the dependences of the electron mean free path on the momentum and energy, respectively; the other notations are as commonly accepted.

Since it is obvious that all macroscopic characteristics of the system depend on the same parameters, it is necessary to express E^2 and β through the quantities determined in the experiment. Then it will be possible to study behavior of the differential conductivity under the TR conditions. However, solution of this problem depends on the boundary conditions, which must correspond to the experimental arrangement. There are only a few regimes which can be realized in experiment [4].

Here, we will consider one of the possible experimental regimes and study the question of this regime to be stationary under the TR conditions.

Let a potential difference be applied along the x axis, which creates a static electric field E_x and gives rise to an electric current $\mathbf{J}_x \neq 0$ in the same direction. Let a magnetic field $\mathbf{H}(H_x, 0, H_z)$ be applied in the plane xOz at an angle χ to the field E_x ($E_x \sim J_x$). Apparently, in the general case, all components of the total electric field $\mathbf{E}(E_x, E_y, E_z)$ and current density $\mathbf{J}(J_x, J_y, J_z)$ vectors are nonzero; let χ_0 be the angle between **H** and **J**.

Consider the boundary conditions corresponding to one possible experimental regime in which the TR can be observed (in a semiconductor sample having the shape of a rectangular parallelepiped with the generatrix directed along the x axis [4]):

$$\begin{aligned} &E_x \neq 0, \quad E_y \neq 0, \quad E_z \neq 0; \\ &J_x \neq 0, \quad J_y = 0, \quad J_z = 0, \end{aligned} \quad (3)$$

where E_y is the Hall field and E_z is the so-called field of the longitudinal-transverse galvanomagnetic effect.

1063-7850/02/2809-0782$22.00

Under boundary conditions (3), in the presence of a strong ($\eta \gg 1$) or weak ($\eta \ll 1$) classical magnetic fields, the following relations are valid [5]:

$$E_z/E_y \cong b_1\sqrt{\eta}\cos\chi \ll 1 \text{ (for } \eta \gg 1),$$

$$E_z/E_y \cong b_2\cos\chi/\sqrt{\eta} \ll 1 \text{ (for } \eta \gg 1),$$

where $b_1 \le 1$ and $b_2 < 1$ for all the known scattering mechanisms. With an allowance for the above relations and conditions, we obtain

$$\chi_0 = \chi; \quad \cos\beta = \cos\theta\cos\chi; \qquad E^2 = E_x^2(1+\tan^2\theta), \quad \tan^2\theta = E_y^2/E_x^2. \tag{4}$$

Consider a general expression for the current density:

$$\mathbf{J} = -en\left\{\mu_1\mathbf{E} + \mu_2\frac{[\mathbf{EH}]}{H} + \mu_3\frac{\mathbf{H}(\mathbf{EH})}{H^2}\right\}, \tag{5}$$

where the first term describes the current in the electric field direction, the second term represents the Hall current, and the third term corresponds to the current focused by the magnetic field; μ_1, μ_2, μ_3 are the coefficients of mobility for the corresponding currents.

With allowance for Eqs. (4) and boundary conditions (3), the conductivity is

$$\sigma = \sigma_0\frac{\mu_1}{\mu_0}\frac{\left(1+\dfrac{\mu_2^2}{\mu_1^2}\right)}{\left(1+\dfrac{\mu_2^2}{\mu_1^2}\cos^2\chi\right)}, \tag{6}$$

where σ_0 and μ_0 are the conductivity and mobility in a weak electric field, respectively.

Under TR conditions (i.e., for $x \longrightarrow \infty$), the Hall angle θ tends to $\pi/2$ [6] and, hence, the nonequilibrium electron distribution function becomes the same as that in the crossed fields, which can be written in a compact form as

$$f_0(x) = N\exp\left(-\frac{\eta^\zeta x^\xi}{\alpha\xi}\right), \quad \xi \ne 0, \tag{7}$$

where N is a normalization factor; $\xi = \xi_1 = 1 - \dfrac{t+s}{2}$ and $\zeta = 0$ in a weak magnetic field; and $\xi = \xi_2 = 1 - \dfrac{t-s}{2}$ and $\zeta = 1$ in a strong magnetic field.

Expression (6) presents a generalization of the conductivity in the presence of a magnetic field applied at an angle to the electric field. For $\chi = \pi/2$, this formula corresponds to the conductivity in the crossed fields, while for $\chi = 0$, the effect of the magnetic field vanishes for quite natural physical reasons.

Using expression (6), we calculated the differential conductivity by a scheme described in [1] and obtained the following result:

$$\frac{\sigma_d}{\sigma} = \frac{2\gamma - s - 1}{5 - 2\gamma - s}. \tag{8}$$

In a weak magnetic field, $2\gamma = t + 3$ and

$$\frac{\sigma_d}{\sigma} = \frac{2 + t - s}{2 - t - s}, \tag{8a}$$

while in a strong magnetic field, $2\gamma = 3 - t$ and

$$\frac{\sigma_d}{\sigma} = \frac{2 - (t+s)}{2 + t - s}. \tag{8b}$$

Summarizing the above results, we may conclude that in the cases of both weak and strong magnetic fields applied under the TR conditions ($t + s = 2$), σ_d changes sign and passes through infinity in the former case (8a) and through zero in the latter case (8b). Therefore, the current–voltage characteristic may acquire an S-like shape in a weak magnetic field and an N-like shape in a strong magnetic field. According to [6], for a combination of scattering mechanisms satisfying the condition $t + s = 2$, the transverse runaway takes place in any nonzero magnetic field. For this reason, the above results appear as quite reliable.

In conclusion, it is necessary to make the following remark. The simple formula (8) for σ_d/σ was obtained from a cumbersome expression by using a necessary condition for the appearance of TR ($\alpha \longrightarrow \infty$) and by canceling $\cos\chi \ne 0$. From this it follows that the expressions (8), (8a), and (8b) are valid only in sufficiently strong electric and magnetic fields oriented at an angle relative to each other.

Acknowledgments. This study was supported by the International Scientific-Technological Center, grant no. G-394.

REFERENCES

1. Z. S. Kachlishvili, N. K. Metreveli, and F. G. Chumburidze, Zh. Tekh. Fiz. **70** (5), 48 (2000) [Tech. Phys. **45**, 571 (2000)].
2. Z. S. Kachlishvili and F. G. Chumburidze, Zh. Éksp. Teor. Fiz. **87** (5), 1834 (1984) [Sov. Phys. JETP **60**, 1055 (1984)].
3. Z. S. Kachlishvili, N. M. Makharadze, and F. G. Chumburidze, Soobshch. Akad. Nauk Gruz. **134**, 69 (1989).
4. F. G. Bass, Zh. Éksp. Teor. Fiz. **48**, 275 (1965) [Sov. Phys. JETP **21**, 181 (1965)].
5. Z. S. Kachlishvili, Phys. Status Solidi A **33**, 15 (1976).
6. Z. S. Kachlishvili, Zh. Éksp. Teor. Fiz. **78** (5), 1955 (1980) [Sov. Phys. JETP **51**, 982 (1980)].

Translated by P. Pozdeev

Technical Physics Letters, Vol. 28, No. 9, 2002, pp. 784–786. Translated from Pis'ma v Zhurnal Tekhnicheskoĭ Fiziki, Vol. 28, No. 18, 2002, pp. 72–76.

The Equilibrium Shape of a Liquid Drop in Mutually Perpendicular Electrostatic and Hydrodynamic Fields

A. I. Grigor'ev

Yaroslavl State University, Yaroslavl, Russia

e-mail: grig@uniyar.ac.ru

Received May 13, 2002

Abstract—An analysis of the balance of pressures on the surface of a drop of an ideal incompressible liquid, exposed to a homogeneous electrostatic field and streamlined by a laminar flow of an ideal incompressible fluid perpendicular to the field, shows that, in the approximation linear with respect to the deformation amplitude, the equilibrium drop shape represents a triaxial ellipsoid. *© 2002 MAIK "Nauka/Interperiodica".*

The phenomenon of instability of the surface of a liquid drop is of considerable interest from the standpoint of numerous applications in geophysics and technical physics [1]. However, most investigations devoted to this problem were stimulated by the interest in elementary processes inside a storm cloud, related to the still incompletely clear physical mechanism of initiation of lightning discharge. Analysis of the drop stability with respect to constant and variable, intrinsic and polarization charges leads to unreasonably high values of the intrinsic charges and external electric fields for which a crown discharge can be initiated in the vicinity of such a drop and a lightning discharge can take place in the cloud [1–3].

Allowance for a laminar gas flow streamlining such a drop in the direction parallel to an external electrostatic field can only decrease the eccentricity of a spheroid representing the equilibrium shape of the drop in this field [4, 5]. Nor can the trend be altered by the presence of the intrinsic charge of the drop [6]. Nevertheless, there is a still unstudied possibility of reducing the critical conditions for realization of the drop instability, which is offered by a hydrodynamic deformation of the drop into a triaxial ellipsoid in the case when an external electrostatic field and the hydrodynamic flow streamlining the drop are noncollinear [7].

In this context, let us determine the equilibrium shape of a drop of an ideal incompressible liquid exposed to a homogeneous electrostatic field $\mathbf{E}_0$ and streamlined by a laminar flow of a gas with a density ρ moving at a velocity $\mathbf{U}$ perpendicular to the field direction ($\mathbf{U} \perp \mathbf{E}_0$). The analysis will be performed in a Cartesian coordinate system with the origin at the drop center, in which the field vector $\mathbf{E}_0$ is oriented along the unit vector $\mathbf{n}_z$ and the flow velocity $\mathbf{U}$, along the unit vector $\mathbf{n}_x$. We assume that the flow velocity U is much smaller than the sound velocity in the gas, so that the medium is modeled by the ideal incompressible fluid.

A drop of the ideal incompressible liquid for $E_0 = 0$ and $U = 0$ possesses a spherical shape, the radius of which is readily found from the balance of pressures at the liquid surface:

$$\frac{2\sigma}{R} = \Delta p,$$

where σ is the surface tension and Δp is the constant difference of pressures inside the drop and in the surrounding medium.

Now let us pass to the case when $E_0 \neq 0$ and $U \neq 0$. Then the equilibrium drop shape would differ from spherical. The new equilibrium shape is conveniently described in a spherical coordinate system with the origin at the drop center, the angle θ measured from the direction of $\mathbf{E}$, and the angle φ measured from the direction of $\mathbf{U}$:

$$r(\theta, \varphi) = R + h(\theta, \varphi) \equiv R + \sum_{n=0}^{\infty} \sum_{m=-n}^{m=n} A_n^m Y_n^m(\theta, \varphi). \quad (1)$$

In this expression, $Y_n^m(\theta, \varphi)$ are the nonnormalized spherical functions, A_n^m are the individual mode amplitudes, $\mu \equiv \cos(\theta)$, and $h(\theta, \varphi)$ is the deviation from the spherical surface. Let us find the perturbation $h(\theta)$ of the spherical surface (perturbed mode amplitudes A_n^m) from the balance of pressures at the equilibrium liquid surface:

$$p_\sigma = \Delta p + p_E + p_U. \quad (2)$$

For this purpose, the terms in the right-hand part of (2) will be determined for the initial spherical surface, while the Laplace pressure p_σ in the left-hand part, for

1063-7850/02/2809-0784$22.00 © 2002 MAIK "Nauka/Interperiodica"

a nearly perturbed spherical surface. Here p_E is the electrostatic field pressure produced by a polarization charge upon the spherical surface; p_U is the hydrodynamic pressure of the laminar fluid flow streamlining the spherical drop.

In order to determine the mode amplitudes A_n^m excited as a result of interaction of the free drop surface with the electric and hydrodynamic fields existing at the surface, let us write expressions for the pressures p_σ, p_E, and p_U at the nearly perturbed spherical surface in the form of expansions in spherical functions [5, 8, 9]:

$$p_\sigma = \frac{2\sigma}{R} - \frac{\sigma}{R^2}\sum_{n=0}^{\infty}\sum_{m=-n}^{m=n}[2-n(n+1)]A_n^m Y_n^m(\theta,\varphi); \quad (3)$$

$$p_E = \frac{3E_0^2}{8\pi}[Y_0^0(\theta,\varphi) + 2Y_2^0(\theta,\varphi)]; \quad (4)$$

$$p_U = \frac{9}{8}\rho U^2\left[\frac{2}{3}Y_0^0(\theta,\varphi) + \frac{1}{3}Y_2^0(\theta,\varphi) - \frac{1}{6}Y_2^{-2}(\theta,\varphi)\right]. \quad (5)$$

Substituting formulas (3)–(5) into Eq. (2) and equating the coefficients at the spherical functions of various orders, we obtain the amplitudes of excited modes. As can be readily seen from expressions (4) and (5), only three modes can be excited on the drop surface: $\sim Y_0^0(\theta, \varphi)$, $Y_2^0(\theta, \varphi)$, and $\sim Y_2^{-2}(\theta, \varphi)$. The amplitudes of the excited modes can be readily calculated, but the expression for the amplitude $\sim Y_0^0(\theta, \varphi)$ contains an unknown constant pressure difference δp. For this reason, it will be more convenient to calculate A_0^0 through A_2^0 and A_2^{-2} using the condition of constant volume of a drop of incompressible liquid. The resulting expressions for A_2^0 and A_2^{-2} are as follows:

$$\frac{A_2^0}{R} = \frac{3}{16\pi}\omega + \frac{3}{32}We; \quad \frac{A_2^{-2}}{R} = -\frac{3}{64}We; \quad (6)$$
$$w = E_0^2 R\sigma^{-1}; \quad We = \rho U^2 R\sigma^{-1}.$$

Here, w is a parameter characterizing stability of the drop with respect to the induced charge (the critical value of this parameter at which the drop becomes unstable is about 2.6 [10]); *We* is the Weber number for a sphere streamlined by the flow of a gas with the density ρ.

The expression for the amplitude A_0^0 calculated using the condition of constant volume of a drop of incompressible liquid is quadratic with respect to the A_2^0 and A_2^{-2} amplitudes. Thus, this term can be ignored in the approximation linear with respect to the deformation amplitude.

Consider a triaxial ellipsoid

$$\frac{x^2}{a^2} + \frac{y^2}{b^2} + \frac{z^2}{c^2} = 1$$

with eccentricities e and e_0 of the ellipses formed in the cross section of this triaxial ellipsoid by the planes $x = 0$ and $z = 0$ of the Cartesian coordinate system,

$$e^2 = 1 - \frac{b^2}{c^2}, \quad e_0^2 = 1 - \frac{b^2}{a^2}. \quad (7)$$

In the approximation linear with respect to the square eccentricities e and e_0, the equation of the above ellipsoid in the spherical coordinate system with the origin at the spheroidal drop center is as follows:

$$\frac{r(\theta)}{b} = \left\{1 + \left[\frac{1}{6}e^2 + \frac{1}{6}e_0^2\right]Y_0^0(\theta,\varphi) + \left[\frac{1}{3}e^2 - \frac{1}{6}e_0^2\right]Y_2^0(\theta,\varphi)\right. \quad (8)$$
$$\left. + \frac{1}{12}e_0^2 Y_2^{-2}(\theta,\varphi) + O(e^4, e_0^4)\right\}, \quad e^2 \ll 1, \quad e_0^2 \ll 1.$$

Comparing formulas (6) for the mode amplitudes A_2^0 and A_0^{-2} to the coefficients at $Y_2^0(\theta, \varphi)$ and $Y_2^{-2}(\theta, \varphi)$ in expression (8), one can readily see that the body into which the initial spherical drop is deformed represents a triaxial ellipsoid with

$$e^2 = \frac{9}{16\pi}\omega, \quad e_0^2 = -\frac{9}{16}We.$$

A triaxial ellipsoid with such eccentricities e and e_0 according to formulas (7) is elongated in the *OZ* axis and oblate in the *OX* direction. In the absence of a hydrodynamic flow, the drop would acquire a spheroidal shape with the eccentricity e.

Naturally, a question arises as to how the stability of a drop with respect to the external electrostatic field $\mathbf{E}_0$ is influenced by the appearance of a hydrodynamic flow deforming the spheroidal drop into the triaxial ellipsoid. Answering this question would require a special investigation, but it is known [7] that stability of a charged drop having the shape of a triaxial ellipsoid decreases as compared to that of an analogous spheroidal drop. Therefore, we may suggest that, in the case when an electrostatic pressure of the intrinsic charge acting upon the drop surface in addition to the external electrostatic and hydrodynamic fields, deformation of the drop shape toward a triaxial ellipsoid would also decrease the critical conditions for realization of the surface instability with respect to a superposition of the intrinsic and induced charges.

Conclusion. The equilibrium shape of a drop of an ideal incompressible liquid, exposed to a homogeneous electrostatic field and streamlined by a laminar hydrodynamic flow perpendicular to the field, represents a

triaxial ellipsoid elongated in the field direction and oblate in the flow direction.

REFERENCES

1. A. I. Grigor'ev and S. O. Shiryaeva, Izv. Akad. Nauk, Mekh. Zhidk. Gaza, No. 3, 3 (1994).
2. V. A. Dyachuk and V. M. Muchnik, Dokl. Akad. Nauk SSSR **248** (1), 60 (1979).
3. A. I. Grigor'ev and S. O. Shiryaeva, Phys. Scr. **54**, 660 (1996).
4. A. I. Grigor'ev, Pis'ma Zh. Tekh. Fiz. **28** (5), 12 (2002) [Tech. Phys. Lett. **28**, 176 (2002)].
5. A. I. Grigor'ev, Zh. Tekh. Fiz. **72** (7), 41 (2002) [Tech. Phys. **47**, 834 (2002)].
6. A. I. Grigor'ev, Pis'ma Zh. Tekh. Fiz. **28** (12), 91 (2002) [Tech. Phys. Lett. **28**, 530 (2002)].
7. A. I. Grigor'ev and S. I. Shchukin, Zh. Tekh. Fiz. **68** (11), 48 (1998) [Tech. Phys. **43**, 1314 (1998)].
8. A. I. Grigor'ev and S. O. Shiryaeva, Zh. Tekh. Fiz. **57** (9), 1863 (1987) [Sov. Phys. Tech. Phys. **32**, 1119 (1987)].
9. N. E. Kochin, I. A. Kibel', and N. V. Roze, *Theoretical Hydromechanics* (Fizmatgiz, Moscow, 1963), Part 1.
10. G. Taylor, Proc. R. Soc. London, Ser. A **280**, 383 (1964).

Translated by P. Pozdeev

Technical Physics Letters, Vol. 28, No. 9, 2002, pp. 787–789. Translated from Pis'ma v Zhurnal Tekhnicheskoĭ Fiziki, Vol. 28, No. 18, 2002, pp. 77–83.

Diamond Films: Initial CVD Growth Stage Using Nanodiamonds as Nucleation Centers

A. Ya. Vul'[a], V. G. Golubev[a], S. A. Grudinkin[a], A. Krüger[b], and H. Naramoto[c]

[a] *Ioffe Physicotechnical Institute, Russian Academy of Sciences, St. Petersburg, 194021 Russia*
e-mail: grudink@gvg.ioffe.rssi.ru
[b] *Toyohashi University of Technology, Toyohashi 441-8580, Japan*
[c] *Advanced Science Research Center, Japan Atomic Energy Research Institute, Takasaki 370-1292, Japan*

Received April 25, 2002

Abstract—Scanning electron microscopy is used to study features of a mechanism operating in the initial growth stages during the CVD of diamond films on nucleation centers representing predeposited nanodiamonds obtained by method of detonation synthesis. © *2002 MAIK "Nauka/Interperiodica".*

Introduction. Despite considerable progress achieved in the technology of growing diamond films from the gas phase employing various chemical vapor deposition (CVD) techniques [1], the mechanisms of nucleation and initial growth stages are still insufficiently clear for such films grown on the substrates possessing no chemical affinity to carbon. At the same time, it is well known that nucleation is a critical factor determining the film growth rate—a technological parameter of practical significance—which can vary within several orders of magnitude (10–10^3 nm/h) depending on the particular CVD variant employed. For example, the growth rate can reach 10 μm/h for a hot filament CVD and 1 μm/h for a microwave plasma technique [2].

A general technological approach to accelerating the nucleation process during the CVD of diamond films is to pass from heterogeneous to homogeneous growth, which is achieved by preliminarily depositing crystalline diamond precursors onto the substrate surface. From this standpoint, an advantageous technology should use diamond crystallites of minimum possible size in order to provide for the maximum concentration of nucleation centers on the substrate surface. To our knowledge, nanodiamonds obtained by detonation synthesis, possessing an average cluster size of 5 nm, were originally employed as the nucleation centers for the growth of diamond films by the plasma enhanced chemical vapor deposition (PECVD) technique in [3], which ensured a significant increase in the nucleation rate and, hence, in the growth rate of diamond films on silicon substrates.

Previously [4], we reported that the use of nanodiamonds obtained by detonation synthesis in combination with the thermal (hot filament) chemical vapor deposition (HFCVD) technique allowed us to grow diamond films on various substrates (sapphire, stainless steel, silicon, fused quartz) at a growth rate on the order of 1 μm/h. Below we present the experimental data obtained by scanning electron microscopy (SEM), suggest a mechanism, and propose a model describing features of the initial stages of a diamond film growth on nanodiamond nucleation centers.

Experimental results. The layers of nanodiamonds, separated from carbon detonation products by dissolving nondiamond particles in nitric acid [5], were deposited onto substrates from a suspension in isopropyl alcohol. The average size of diamond nanoclusters in the powder used to prepare the suspension was about 5 nm [6]. The diamond clusters are combined in aggregates. As can be seen from the SEM micrograph presented in Fig. 1, the minimum size of such aggregates is about 50 nm, which agrees well with the estimated average size of aggregates in a nanodiamond suspension

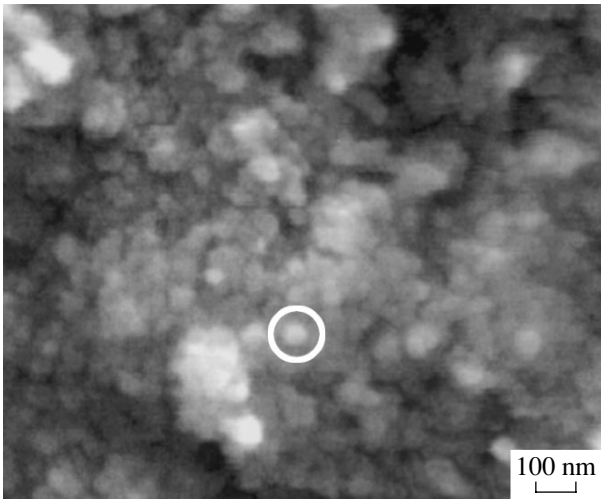

Fig. 1. High-resolution SEM micrograph of a nanodiamond powder. The circle indicates a well-resolved single aggregate composed of diamond nanoclusters.

1063-7850/02/2809-0787$22.00

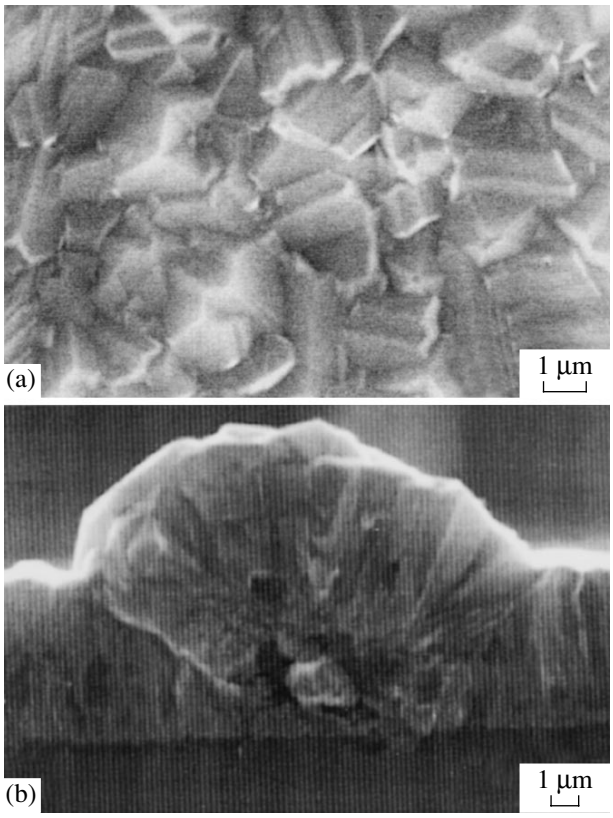

Fig. 2. SEM images of the (a) surface and (b) transverse cleavage of a diamond film grown on a silicon substrate completely covered with diamond precursors.

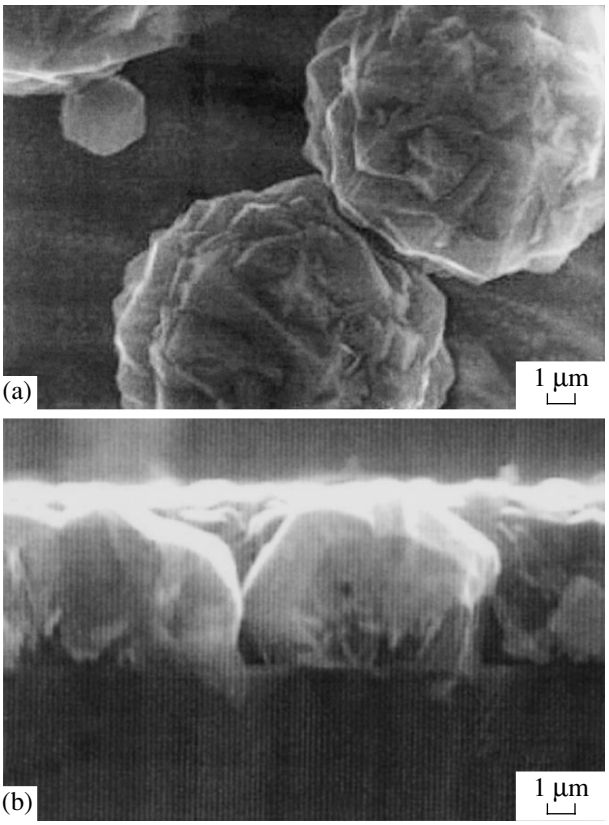

Fig. 3. SEM images of the (a) surface and (b) transverse cleavage of a diamond film grown on a silicon substrate incompletely covered with diamond precursors.

reported previously [5]. Each aggregate is formed from, on average, ten diamond nanoclusters.

The diamond films were grown by HFCVD from a hydrogen–methane mixture by a technology described in detail elsewhere [7]. It was established that effective growth of a diamond film is ensured by heating the substrate with a predeposited layer of nanodiamonds to 750–850°C in atomic hydrogen in the CVD chamber immediately before the growth process.

The Raman spectra of the as-grown diamond films exhibit a narrow (6 cm^{-1}) intense peak at 1332 cm^{-1}, which corresponds to a crystalline diamond phase [4]. A broad, weak signal at 1550 cm^{-1} showed evidence of the presence of a small amount of sp^2-hybridized carbon. The insignificant content of this carbon is confirmed by the fact that X-ray diffraction measurements did not reveal any crystalline sp^2-hybridized carbon phase.

As can be seen from the SEM images of the surface and transverse sections of samples, the diamond films possess a well-pronounced polycrystalline structure (Figs. 2 and 3). Well-distinguished crystallites with base dimensions on the micron scale represent the top parts of the diamond grains.

The SEM images of transverse cleavages show the presence of geometrically regular structures representing grains composed of crystallites with dimensions about one micron (Figs. 2b and 3b). In the case of complete coverage of a silicon substrate with nanodiamond precursors, crystallites (growing in the normal direction) have common side faces and form a continuous film. If the substrate is incompletely covered with nanodiamonds, the resulting film is not continuous and comprises well-distinguishable separate polycrystalline grains.

Nucleation and growth mechanism. Based on the SEM data, we can outline the following mechanism operative in the initial stages of growth of a diamond film from nanodiamond nucleation centers.

The growth of diamond crystallites begins on the surface of aggregates composed of several diamond nanoclusters. The direction of growth for these nanocrystallites is determined by the faces of diamond clusters forming the aggregates.

Etching of the surface of aggregates in atomic hydrogen atmosphere is necessary in order to increase the concentration of unsaturated sp^3 bonds on the surface of nanodiamond nuclei determining the initial growth rate of the diamond film. Before the etching, as

demonstrated in [8], only a small fraction (about 0.4%) of the total number of surface atoms occur in the state with unsaturated C–C bonds. In addition, the effect of nanodiamonds as the nucleation centers is controlled by the presence of sp^2 electron shells coating the diamond cluster [9]. Etching in the atomic hydrogen removes the shell, thus increasing the formation of a new diamond phase on the nucleation centers.

In the course of subsequent growth, crystallites growing on the adjacent aggregates begin to interact with each other. Each polycrystalline grain observed on the surface of a film represents such crystallites grown together.

The proposed mechanism stipulates a multilevel hierarchy of crystal dimensions in the film, including diamond nanoclusters, aggregates, nanocrystallites, and polycrystalline grains. In the case of separate aggregates scattered on a substrate surface (that is, in the absence of interaction between nanocrystallites growing from neighboring aggregates), the final shape of micron-sized polycrystalline grains must be close to spherical—and this is actually observed in experiment (Fig. 3a).

Acknowledgments. The authors are grateful to T. Ohnuki for studying the nanodiamond powder by high-resolution scanning electron microscopy.

The work of the authors from the Ioffe Physicotechnical Institute was supported by the Program "Directed Synthesis of Fullerenes and Other Atomic Clusters."

REFERENCES

1. J. C. Angus and C. C. Hayman, Science **241**, 913 (1988).
2. T. D. Moustakas, *Synthetic Diamond: Emerging CVD Science and Technology*, Ed. by K. E. Spear and J. P. Dismukes (Wiley, New York, 1994), p. 145.
3. T. Yara, H. Makita, A. Hatta, *et al.*, Jpn. J. Appl. Phys. **34**, 312 (1995).
4. S. A. Grudinkin, V. G. Golubev, and A. Ya. Vul', in *Proceedings of the International Conference "Trends in Nanotechnology (TNT 2001)," Segovia, Spain, 2001*, p. 225.
5. A. E. Aleksenskiĭ, V. Yu. Osipov, A. Ya. Vul', *et al.*, Fiz. Tverd. Tela (St. Petersburg) **43** (1), 140 (2001) [Phys. Solid State **43**, 145 (2001)].
6. A. E. Aleksenskiĭ, M. V. Baĭdakova, A. Ya. Vul', *et al.*, Fiz. Tverd. Tela (St. Petersburg) **39**, 1125 (1997) [Phys. Solid State **39**, 1007 (1997)].
7. M. V. Baĭdakova, A. Ya. Vul', V. G. Golubev, *et al.*, Fiz. Tekh. Poluprovodn. (St. Petersburg) **36** (6), 651 (2002) [Semiconductors **36**, 615 (2002)].
8. A. I. Shames, A. M. Panich, W. Kempinski, *et al.*, J. Phys. Chem. Solids (2002) (in press).
9. A. E. Aleksenskiĭ, M. V. Baĭdakova, A. Ya. Vul', and V. I. Siklitskiĭ, Fiz. Tverd. Tela (St. Petersburg) **41** (4), 740 (1999) [Phys. Solid State **41**, 668 (1999)].

Translated by P. Pozdeev

Technical Physics Letters, Vol. 28, No. 9, 2002, pp. 790–791. Translated from Pis'ma v Zhurnal Tekhnicheskoĭ Fiziki, Vol. 28, No. 18, 2002, pp. 84–88.

Photoinduced Recovery of Gamma-Irradiated Fluoride Glasses

P. B. Baskov, V. V. Sakharov, V. A. Stepanov, P. A. Stepanov, and P. V. Kurdyavko

All-Russia Research Institute of Chemical Technology, Russian Academy of Sciences, Moscow, Russia

Leipunskii Institute of Physics and Power Engineering, State Scientific Center of the Russian Federation, Obninsk, Russia

e-mail: stepanov@ippe.rssi.ru

Received April 16, 2002

Abstract—Radiation-induced changes in the optical properties of fluoride glasses (FGs) were studied on samples of zirconium fluoride and aluminum fluoride based compositions gamma-irradiated to a total dose of 1.2 MGy. Upon exposure, the fundamental absorption edge smears and shifts toward longer wavelengths. The FGs studied exhibit self-recovery of the optical properties, whereby the radiation-induced absorption decreases in the course of storage without action of any external factors. Photostimulated recovery of the optical properties of the gamma-irradiated FGs was studied in the range of light wavelengths from 400 to 1200 nm at a light intensity of 1–3 mW/cm^2. The maximum rate of recovery for both zirconium and aluminum fluoride based glasses was observed for the photoannealing at 600 nm. © *2002 MAIK "Nauka/Interperiodica".*

The use of various glasses in the optical systems of setups and devices operating under conditions of irradiation is subject to significant restrictions related, in particular, to a decrease in the spectral range of transparency as a result of radiation damage. For example, the transparency range of traditional quartz glasses in some cases narrows from 0.2–4.0 to 0.3–2 μm.

As is known, fluoride glasses (FGs) are transparent in a wider spectral range of 0.2–7.0 μm, which may decrease to 0.4–6.0 μm upon irradiation [1, 2]. A distinctive feature of FGs is the self-recovery of optical properties of the radiation-colored samples in the course of storage without action of any external factors. For example, a twofold clarification of the gamma-irradiated glasses based on zirconium fluoride is observed upon 24-h storage at room temperature. This property allows FGs to be used as a basis for the development of essentially new radiation-tolerant optical materials—glasses exhibiting self-recovery under conditions of irradiation. In this context, it is of interest to study the process of recovery of the optical transmission of irradiated FGs by exposure to a low-intensity light.

Hobson *et al.* [2] studied the photostimulated recovery of glasses based on zirconium and hafnium fluorides. The samples were gamma-irradiated to a total dose of 6 kGy. It was reported that a decrease in the light wavelength from 570 to 360 nm (whereby the light quantum energy approaches the bandgap width and the optical absorption increases) is accompanied by an increase in the rate of photostimulated recovery. In this context, we have studied the process of recovery of gamma-irradiated FGs illuminated with light in the visible and near infrared (NIR) range.

Samples of fluoride glasses were synthesized from corresponding high-purity metal fluorides with an impurity content not exceeding 10^{-3}–10^{-4} wt %. We studied the zirconium fluoride (ZBLAN) and aluminum fluoride (ABSCMYL) glasses of the following compositions (mol %):

ZBLAN: ZrF_4, 52.0; BaF_2, 20.0; LaF_3, 4.0; AlF_3, 4.0; NaF, 20.0;

ABSCMYL: AlF_3, 36.0; BaF_2, 12.3; SrF_2, 12.3; CaF_2, 12.3; MgF_2, 12.3; YF_3, 12.3; LaF_3, 2.5.

The FG samples were gamma-irradiated at room temperature using a Co^{60} source operating at a dose rate of 1 Gy/s. The ZBLAN and ABSCMYL samples were

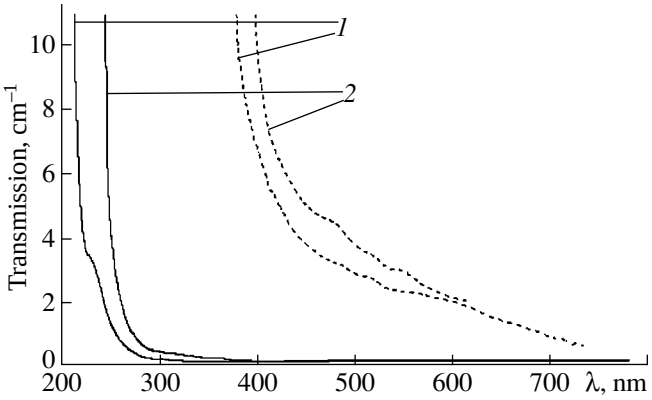

Fig. 1. Optical absorption spectra of fluoride glasses measured before (solid curves) and after (dashed curves) gamma-irradiation: (*1*) zirconium fluoride glass (ZBLAN) irradiated to a dose of 1.2×10^6 Gy; (*2*) aluminum fluoride glass (ABSCMYL) irradiated to a dose of 10^5 Gy.

1063-7850/02/2809-0790$22.00 © 2002 MAIK "Nauka/Interperiodica"

exposed to a total dose of 1.2×10^6 and 10^5 Gy, respectively. The optical absorption spectra of both glasses measured before and after gamma-irradiation are presented in Fig. 1. As can be seen, the spectra of irradiated samples display a shift by ~200 nm toward longer wavelengths and exhibit smearing of the fundamental absorption edge. The photostimulated annealing was produced by the light of a high-pressure mercury vapor lamp operating in a wavelength range from 400 to 1200 nm. The samples were illuminated using a light intensity of 1–3 mW/cm^2 within separated bands with a spectral width of 10–15 nm. The time of total recovery was determined by coincidence (to within 1%) of the absorption spectra of the initial glasses and those illuminated in the range from 400 to 700 nm.

Figure 2 shows a plot of the total recovery time t versus light wavelength λ for the aluminum fluoride-based (ABSCMYL) glass. The rate of recovery exhibits a significant growth when λ increases from 400 to 600 nm; the process sharply slows down in the NIR range. Recovery of the samples of a zirconium fluoride-based (ZBLAN) glass was also predominantly stimulated by the red light.

As is known [3], a decrease in the optical transmission of gamma-irradiated glasses in the spectral range below the fundamental absorption range is due to optical inhomogeneities arising in the material when the irradiation-induced carriers fill the shallow electron–hole traps and then migrate toward structural inhomogeneities. Our experimental results show evidence of a weak resonance absorption in the red spectral region, which is probably related to the transitions from shallow trap levels. The relaxation of traps leads to disappearance of the optical inhomogeneities.

The effect of accelerated recovery of the optical properties of fluoride glasses under the action of low-intensity light with a wavelength within the transparency range of these materials can be used for the development of radiation-resistant optical devices.

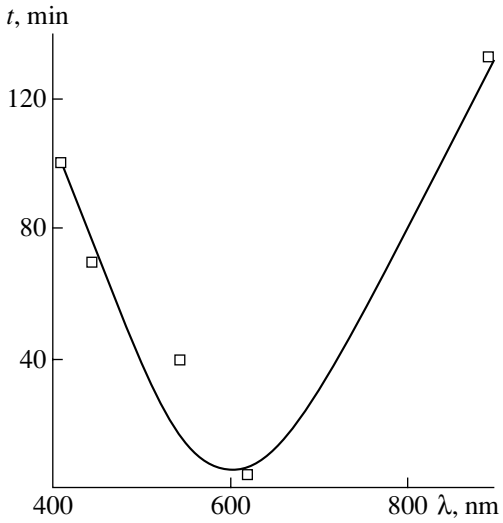

Fig. 2. A plot of the total recovery time t versus light wavelength λ in the 380–900 nm range for the aluminum fluoride based (ABSCMYL) glass (light intensity, 2 mW/cm^2).

REFERENCES

1. D. L. Griscom, J. Non-Cryst. Solids **113**, 146 (1989).
2. P. R. Hobson, D. C. Imre, *et al.*, in *Proceedings of the International Conference on Inorganic Scintillators and Their Application (SCINT 95), 1995.*
3. P. V. Demenkov, R. L. Ibragimov, O. A. Plaksin, *et al.*, Preprint FÉI-2764 (1999).

Translated by P. Pozdeev

Technical Physics Letters, Vol. 28, No. 9, 2002, pp. 792–794. Translated from Pis'ma v Zhurnal Tekhnicheskoĭ Fiziki, Vol. 28, No. 18, 2002, pp. 89–94.

Electrical Characteristics of (*p*)3C-SiC–(*n*)6H-SiC Heterojunctions

A. A. Lebedev, A. M. Strel'chuk, D. V. Davydov, N. S. Savkina, A. N. Kuznetsov, and L. M. Sorokin

Ioffe Physicotechnical Institute, Russian Academy of Sciences, St. Petersburg, 194021 Russia

Received April 22, 2002

Abstract—The electrical characteristics of (*p*)3C-SiC–(*n*)6H-SiC epitaxial heterostructures obtained by sublimation epitaxy in vacuum are studied. The band discontinuities are determined and the energy band diagram of the heterojunction is constructed. It is shown that the obtained heterostructure offers a promising material for high electron mobility transistors. © *2002 MAIK "Nauka/Interperiodica".*

Previously [1, 2], we demonstrated that high-quality epitaxial heterostructures of the (*p*)3C-SiC–(*n*)6H-SiC type can be obtained by sublimation epitaxy in vacuum. The data of structural analysis showed that growth of the *p*-type 3C-SiC layer took place immediately on the *n*-type 6H-SiC substrate. According to the results of EBIC measurements, the *pn* junction was sufficiently sharp and structurally perfect.

This study aimed at obtaining diode structures based on the aforementioned heteropolytype structures and at determining electrical characteristics of the samples.

The ohmic contacts on the *p*-type layer were prepared by magnetron sputter deposition of Al and Ti films, followed by annealing in vacuum at 1000°C. The ohmic contacts on the n^+-type substrate were prepared by magnetron sputter deposition of a Ni film, followed by annealing in vacuum at 900°C. Mesastructures with working-area dimensions of 3×10^{-3}, 1×10^{-4}, and 8×10^{-5} cm were obtained by ion plasma etching in SF_6 with an Al mask.

The concentrations of uncompensated donors (acceptors), determined from the slope of the capacitance–voltage (*C–U*) characteristics, was N_d–N_a = (1.7–2) × 10^{17} cm^{-3} for (*n*)6H-SiC layers and N_a–N_d ~ 3×10^{18} cm^{-3} for (*p*)3C-SiC layers. The *C–U* curves exhibited rectification in the C^{-2} versus *U* coordinates (Fig. 1), which was evidence of a sharp *pn* junction. The capacitance cutoff voltage (U_c^c) of the diodes studied, determined by extrapolating the C^{-2} versus *U* line to $C^{-2} \longrightarrow 0$ (*C* is the *pn* junction capacitance and *U* is the applied voltage), was 2.65 ± 0.05 V. In the region of small current densities, the current–voltage (*J–U*) characteristics obeyed the exponential law $J = J_0 \exp(qV/nkT)$ (Fig. 2) with an ideality factor of $q \sim 2.1$–2.4. Since most of the diodes studied exhibited similar *J–U* and *C–U* curves, it was concluded that the properties of epitaxial layers are sufficiently homogeneous over distances on the order of the diameter of the heterostructure.

The electroluminescence (EL) spectra of the diodes exhibited two emission bands with maxima at $h\nu_{max} \approx$ 2.9 and 2.3 eV, the intensities of which increased in proportion to the direct current (Fig. 3). The EL band at $h\nu_{max} \approx 2.9$ eV dominated; the intensity of the second band increased upon heating a sample. Taking into account the positions of the emission bands (with the values of $h\nu_{max} \approx 2.9$ and 2.3 eV being close to the bandgap widths of 6H-SiC and 3C-SiC, respectively), small halfwidths (in comparison to that of the so-called "defect" green EL line in 6H-SiC), and the characteristic behavior of the EL intensity with increasing current

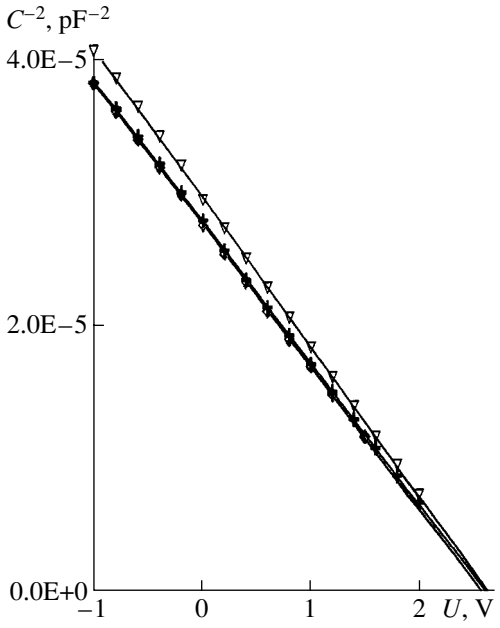

Fig. 1. Typical capacitance–voltage characteristics of the (*p*)3C-SiC–(*n*)6H-SiC heterojunctions studied.

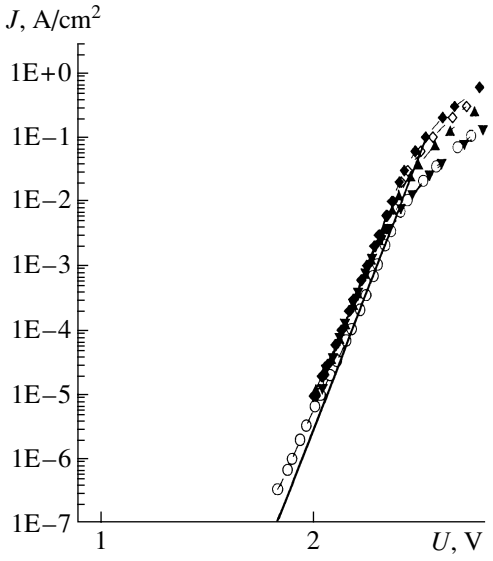

Fig. 2. Typical current–voltage characteristics of the (*p*)3C-SiC–(*n*)6H-SiC heterojunctions studied.

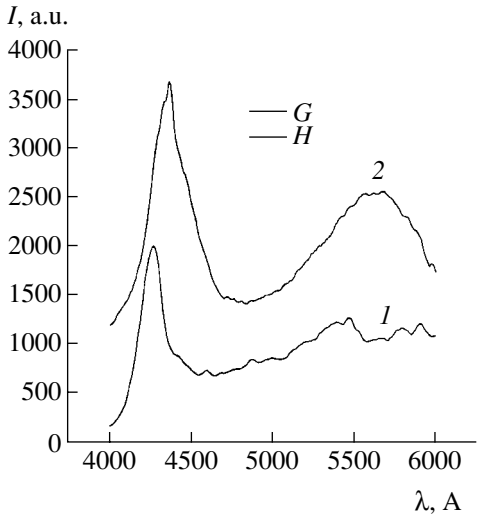

Fig. 3. Electroluminescence spectra of the (*p*)3C-SiC–(*n*)6H-SiC heterojunctions measured at a direct current of 70 mA and $T = 300$ (*1*) and 600 K (*2*) (for clarity, curve *2* is shifted upward by 1000 a.u.).

and temperature allow the observed emission bands to be attributed to the annihilation of free excitons in 6H-SiC and 3C-SiC [3, 4].

The energy differences between the conduction (ΔE_c) and valence (ΔE_v) band can be estimated using experimental values of the contact potential difference $U_d = U_c^c + 2kT/e$ (where k is the Boltzmann constant, T is the absolute temperature, and e is the electron charge) [5]. As is known [6],

$$\Delta E_c = U_d - E_{g_{3C}} + \mu_{3C} + \mu_{6H},$$

where E_g is the bandgap width of 3C-SiC; μ_{3C} and μ_{6H} are the differences between the Fermi energies and the nearest band bottom in *p*(3C)-SiC and (*n*)6H-SiC, respectively.

Assuming that the room-temperature Fermi level coincides with the levels of the main doping impurities ($\mu_{3C} \approx 0.2$ eV and $\mu_{6H} \approx 0.15$ eV), we obtain $\Delta E_c = 0.55 \pm 0.05$ eV and [6] $\Delta E_v = E_{g_{6H}} - E_{g_{3C}} - \Delta E_c = 0.05$ eV. Note that the ΔE_c estimate agrees well with the recent data on the electron affinities in 6H-SiC and 3C-SiC, $\chi_{6H} = 3.5$ eV and $\chi_{3C} = 4.0$ eV [7], from which we also obtain $\Delta E_c = \chi_{3C} - \chi_{6H} \sim 0.5$ eV.

Figure 4 shows the energy band diagram constructed for the (*p*)3C-SiC–(*n*)6H-SiC heterojunction using the ΔE_c and ΔE_v estimates obtained above. This pattern is close to the band diagram theoretically calculated for the same couple of semiconductors [8]. As can be seen from Fig. 4, a small value of ΔE_v does not prevent the injection of holes from (p^+)3C-SiC to (*n*)6H-SiC; at the same time, electrons can also be injected from wide-bandgap into narrow-bandgap material. Thus, the EL spectrum of the heterostructure studied may contain emission bands related to the recombination in both 6H-SiC and 3C-SiC, in agreement with the experimental spectrum.

The experimental data obtained in our study can be explained by the formation of a (*p*)3C-SiC–(*n*)6H-SiC heterojunction possessing high structural perfection. The estimated energy differences $\Delta E_c = 0.55$ eV and $\Delta E_v = 0.05$ eV agree well with theoretical calculations and experimental values of the electron affinity of 6H-SiC and 3C-SiC. The energy band diagram suggests a principal possibility of creating a field-effect transistor with a 2D-electron gas (high electron mobil-

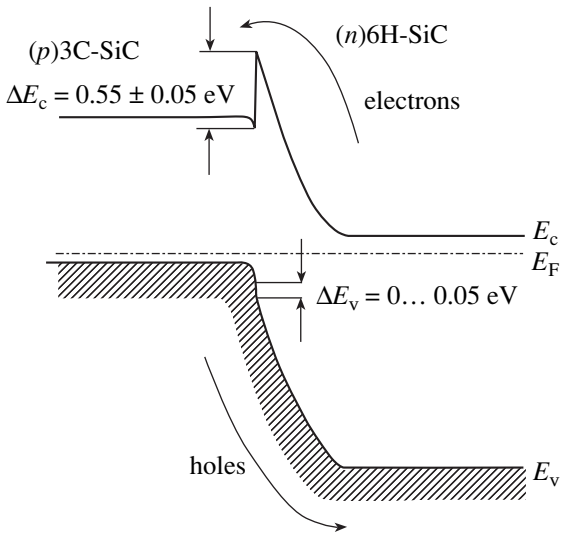

Fig. 4. Energy band diagram of the (*p*)3C-SiC–(*n*)6H-SiC heterojunction.

ity transistor) based on the (*p*)3C-SiC–(*n*)6H-SiC heterojunction obtained.

Acknowledgments. This study was supported by the Russian Foundation for Basic Research, project nos. 00-02-16688 and 01-02-17657.

REFERENCES

1. A. A. Lebedev, A. M. Strel'chuk, D. V. Davydov, *et al.*, Appl. Surf. Sci. **183**, 421 (2001).
2. A. A. Lebedev, G. N. Mosina, I. P. Nikitina, *et al.*, Pis'ma Zh. Tekh. Fiz. **27** (24), 57 (2001) [Tech. Phys. Lett. **27**, 1052 (2001)].
3. Yu. M. Altaĭskiĭ, S. F. Avramenko, O. A. Guseva, and V. S. Kiselev, Fiz. Tekh. Poluprovodn. (Leningrad) **21**, 2072 (1987) [Sov. Phys. Semicond. **21**, 1256 (1987)].
4. A. A. Lebedev, Fiz. Tekh. Poluprovodn. (St. Petersburg) **33**, 129 (1999) [Semiconductors **33**, 107 (1999)].
5. C. G. B. Garret and W. H. Brattain, Phys. Rev. B **19** (2), 376 (1970).
6. B. L. Sharma and R. K. Purohit, *Semiconductor Heterojunctions* (Pergamon, Oxford, 1974; Sov. Radio, Moscow, 1979).
7. M. J. Bozack, Phys. Status Solidi B **202**, 549 (1997).
8. F. Bechstedt, P. Kackell, A. Zywiets, *et al.*, Phys. Status Solidi B **202**, 35 (1997).

Translated by P. Pozdeev